

Computational Analysis of Multi-Phase Flow in Porous Media with Application to
Fuel Cells

by

Alireza Akhgar

B.Sc., Persian Gulf University, Iran, 2008

M.Sc., Shahid Bahonar University, Iran, 2011

A Dissertation Submitted in Partial Fulfillment of the
Requirements for the Degree of

DOCTOR OF PHILOSOPHY

in the Department of Mechanical Engineering

© Graduate Advisor, 2016
University of Victoria

All rights reserved. This dissertation may not be reproduced in whole or in part, by
photocopying or other means, without the permission of the author.

Computational Analysis of Multi-Phase Flow in Porous Media with Application to
Fuel Cells

by

Alireza Akhgar

B.Sc., Persian Gulf University, Iran, 2008

M.Sc., Shahid Bahonar University, Iran, 2011

Supervisory Committee

Dr. Ned Djilali, Supervisor
(Department of Mechanical Engineering, University of Victoria)

Dr. Henning Struchtrup, Departmental Member
(Department of Mechanical Engineering, University of Victoria)

Dr. Yonas Dibike, Outside Member
(Water and Climate Impacts Research Centre, University of Victoria)

Supervisory Committee

Dr. Ned Djilali, Supervisor

(Department of Mechanical Engineering, University of Victoria)

Dr. Henning Struchtrup, Departmental Member

(Department of Mechanical Engineering, University of Victoria)

Dr. Yonas Dibike, Outside Member

(Water and Climate Impacts Research Centre, University of Victoria)

ABSTRACT

Understanding how the water produced in an operating polymer electrolyte membrane fuel cell (PEMFC) is transported in cathode catalyst layer (CCL) is crucial to improving performance and efficiency. In this thesis, a multiple-relaxation-time (MRT) lattice Boltzmann method (LBM) is employed to simulate the high density ratio, multiphase water transport in the CCL. The three-dimensional structure of the catalyst layer is reconstructed based on experimental data acquired with a dual beam scanning electron microscope/focused ion beam system and a stochastic method using lower order statistical functions (e.g. porosity and two point correlation functions). Simulations of the water transport dynamics are performed to examine the effect of a range of physical parameters: wettability, viscosity ratio, pressure gradient, and surface tension. The water penetration patterns in the catalyst layers reveal a complex fingering process and transition of the water transport pattern from a capillary fingering regime to a stable displacement regime is observed when the wettability potential of the catalyst layer changes.

The second part of the analysis focuses on quantifying the impact of liquid water distribution and accumulation in the catalyst layer on effective transport properties by coupling two numerical methods: the two-phase LBM is used to determine equilibrium liquid water distribution, and then a finite volume-based pore-scale model (FV-PSM)

is used to compute transport of reactant and charged species in the CL accounting for the impact of liquid water saturation .The simulated results elucidate and quantify the significant impact of liquid water on the effective oxygen and water vapor diffusivity, and thermal conductivity in CLs.

Contents

Supervisory Committee	ii
Abstract	iii
Table of Contents	v
List of Figures	viii
Nomenclature	xiii
Acknowledgements	xvii
Dedication	xviii
1 Introduction	1
1.1 Background and Motivation	1
1.2 Fuel Cell Performance and Water Generation Reaction	3
1.3 Thesis Organization	6
2 Literature Review	7
2.1 Performance and Degradation in Fuel cells: CL Morphology and Water Effects	7
2.2 Catalyst Layer Microstructure Characterization and Reconstruction .	8
2.3 Experimental Observation of Liquid Water Dynamics in Fuel Cells . .	10
2.4 Theoretical Methods for Two Phase Flow in Porous Media	11
2.5 Multi-Phase Lattice Boltzmann Method	13
2.6 Impact of Liquid Water on Transport Properties	17

3	Reconstruction of the Physical CL Model	21
3.1	FIB/SEM Reconstructed CL	21
3.1.1	CL Preparation and Image Acquisition	21
3.1.2	Image Processing	21
3.1.3	3D Reconstruction and Pore-Size Distribution	23
3.2	Stochastically Reconstructed CL	26
4	Methodology	30
4.1	Boltzmann Equation	30
4.2	Lattice Boltzmann Equation	32
4.3	Boundary Conditions	34
4.3.1	Periodic Boundary Condition	34
4.3.2	Bounce-Back Boundary Condition	35
4.4	MRT-LBM	36
4.5	FVM-PSM	38
5	Evaluation, Analysis, and Comparisons	41
5.1	Validation of Numerical Code	41
5.1.1	Permeability of a Packed Bed	41
5.1.2	Laplace Law	44
5.1.3	Wettability Potential of Solid Surfaces	45
5.1.4	Capillary Pumping in a Nano-Channel	46
5.2	Water Transport in a Reconstructed Catalyst Layer	48
5.2.1	Effect of Surface Tension	65
5.3	Capillary Pressure in a Reconstructed Catalyst Layer	71
5.4	Impact of Liquid Water on Transport Parameters in Catalyst Layers .	74
5.4.1	Effect of Different Contact Angles	76
5.4.2	Effect of Different Pressure Gradients	78
6	Conclusions and Future Work	84
6.1	Conclusions	84
6.2	Future Work	86
A	Additional Information	87
A.1	Impact of Liquid Water on Transport Parameters in hydrophilic Catalyst Layers	87

A.2 Relation Between Units in the Framework of LBM and Physical Units	88
Bibliography	90

List of Figures

Figure 1.1	SEM image of a PEM fuel-cell catalyst layer (ESTP Laboratory, University of Victoria, unpublished).	3
Figure 1.2	Schematic of a PEM fuel cell unit	5
Figure 1.3	Schematic of a half-cell unit (Cathode electrode)	5
Figure 3.1	Schematic of a CL microstructure based on the agglomeration model	23
Figure 3.2	Schematic of the experimental imaging set up on Dual Beam FIB-SEM. The SEM image was taken with the electron beam inclined at 52° degrees to the ion beam	24
Figure 3.3	Image-processing procedure explained using a single slice at various processing stages: (a) original 8-bit gray-scale image, (b) stretched in the y-direction, (c) aligned, (d) area of interest cropped, (e) normalization applied, and (f) thresholded.	24
Figure 3.4	3-D view of the reconstructed domain with domain Size: 1400nm × 1814nm × 1500nm (Red area=pore; Blue area=solid)	25
Figure 3.5	Pore-size distribution in CL, based on experimental FIB /SEM data	25
Figure 3.6	Flow chart outlining the methodology used in the present study	26
Figure 3.7	Steps to reconstruct the CL and to obtain the initial phase of liquid water distribution: a) cropped area of interest from FIB/SEM showing solid phase (light gray) and open pores (dark gray); b) binary image obtained after image processing and thresholding with solid phase (black) and pores (white); c) reconstructed with carbon particles (green), ionomer (yellow) and pores (blue); and d) computed liquid water distribution (red) in the CL.	29

Figure 4.1	3D network of LBM	33
Figure 4.2	Schematic of periodic boundary condition	35
Figure 4.3	Schematic of bounce-back boundary condition	36
Figure 5.1	Comparison of simulation results for dimensionless permeability obtained by LBM with the analytical solution and the KC relation for a packed-sphere porous medium.	43
Figure 5.2	Absolute permeability versus fluid viscosity based on MRT-LBM and SRT-LBM.	44
Figure 5.3	Comparison of simulation results for the pressure jump across the interface with the analytical solution based on the Laplace law.	45
Figure 5.4	Simulation of equilibrium contact angle of a hemispherical liquid droplet on a surface: a) $\theta = 60^\circ$ b) $\theta = 90^\circ$ c) $\theta = 120^\circ$. . .	46
Figure 5.5	Comparison of simulation results for the measured contact angles with theoretical values.	46
Figure 5.6	a) Schematic of initial distribution of different fluids in a nano-channel assuming different contact angles b) capillary effect in a nano-channel.	47
Figure 5.7	Schematic of reconstructed catalyst layers.	49
Figure 5.8	Visualization of water transport after $2.3 \mu s$ in reconstructed catalyst layers with $\delta p = .0017$ ($=113.3$ KPa), $M=54$, and different contact angles: a) $\theta = 105^\circ$ b) $\theta = 110^\circ$ c) $\theta = 115^\circ$ d) $\theta = 120^\circ$ e) $\theta = 130^\circ$ f) $\theta = 140^\circ$. Left column (red: water, green: air, blue: solid structure); right column is the isosurface of water.	52
Figure 5.9	Visualization of water distribution after $2.3 \mu s$ in reconstructed catalyst layers with $\delta p = .0017$, $M=54$, and different contact angles: $\theta = 105^\circ$ b) $\theta = 110^\circ$ c) $\theta = 115^\circ$ d) $\theta = 120^\circ$ e) $\theta = 130^\circ$ f) $\theta = 140^\circ$. Red: water, green: air, blue: solid structure.	55

Figure 5.10 Visualization of water transport after $2.37 \mu s$ in reconstructed catalyst layers with $\delta p=.0017$, $M=18$, and assuming different contact angles: a) $\theta = 105^\circ$ b) $\theta = 110^\circ$ c) $\theta = 115^\circ$ d) $\theta = 120^\circ$ e) $\theta = 130^\circ$ f) $\theta = 140^\circ$. Left column (red: water, green: air, blue: solid structure); right column shows the isosurface of water at equilibrium status. 58

Figure 5.11 Visualization of water distribution after $2.37 \mu s$ in reconstructed catalyst layers with $\delta p=.0017$, $M=18$, and assuming different contact angles: a) $\theta = 105^\circ$ b) $\theta = 110^\circ$ c) $\theta = 115^\circ$ d) $\theta = 120^\circ$ e) $\theta = 130^\circ$ f) $\theta = 140^\circ$. Red: water, green: air, blue: solid structure. 61

Figure 5.12 Visualization of water transport after $2.37 \mu s$ in reconstructed catalyst layers with $\delta p=0.0034$ ($=226.6$ KPa), $M=18$, and assuming different contact angles: a) $\theta = 105^\circ$ b) $\theta = 110^\circ$ c) $\theta = 115^\circ$ d) $\theta = 120^\circ$ e) $\theta = 130^\circ$ f) $\theta = 140^\circ$. Left column (red: water, green: air, blue: solid structure); right column shows the isosurface of water at equilibrium status. 64

Figure 5.13 Simulated water saturation versus contact angle considering the effects of different pressure gradients and viscosity ratios. . . . 65

Figure 5.14 Visualization of water transport after $2.3 \mu s$ in reconstructed catalyst layers with $\delta p=.0017$, $M=54$, $\sigma=.0625$, considering different contact angles: a) $\theta = 110^\circ$ b) $\theta = 130^\circ$. Left column (red: water, green: air, blue: solid structure); right column shows the isosurface of water at equilibrium status. 67

Figure 5.15 Simulated water saturation versus contact angle considering the effect of different surface tension values. 68

Figure 5.16 Visualization of water transport after $2.37 \mu s$ in reconstructed catalyst layers with $\delta p=.0017$, $M=18$, $\sigma=.0625$, and considering different contact angles: a) $\theta = 110^\circ$ b) $\theta = 130^\circ$. Left column (red: water, green: air, blue: solid structure); right column shows the isosurface of water at equilibrium status. . . 69

Figure 5.17 Simulated water saturation versus contact angle considering the effect of different surface tension values. 70

Figure 5.18 Variation of water saturation with contact angle considering the effects of different pressure gradients and viscosity ratios. . 71

Figure 5.19	Capillary pressure in the reconstructed catalyst layer	73
Figure 5.20	Effect of different contact angles on capillary pressure	73
Figure 5.21	3D model of the reconstructed CL including ionomer, carbon spheres, water, and pores (ionomer: yellow, carbon: green, water: red, and pores: blue).	74
Figure 5.22	Impact of different liquid water saturations on effective oxygen and water-vapour diffusivities and on proton, electron, and thermal conductivities.	76
Figure 5.23	Impact of different ionomer contact angles on effective oxygen diffusivity.	77
Figure 5.24	Impact of different ionomer contact angles on effective water-vapour diffusivity.	78
Figure 5.25	Impact of different ionomer contact angles on effective thermal conductivity.	78
Figure 5.26	Impact of different pressure gradients on effective oxygen diffusivity with hydrophobic ionomer surface.	79
Figure 5.27	The impact of different pressure gradients on the effective oxygen diffusivity with hydrophilic ionomer surface.	79
Figure 5.28	Impact of different pressure gradients on effective water-vapour diffusivity with hydrophobic ionomer surface.	80
Figure 5.29	Impact of different pressure gradients on effective thermal conductivity with hydrophobic ionomer surface.	80
Figure 5.30	Impact of different pressure gradients on effective oxygen diffusivity with hydrophobic ionomer surface.	81
Figure 5.31	Impact of different pressure gradients on effective water-vapour diffusivity with hydrophobic ionomer surface.	81
Figure 5.32	Impact of different pressure gradients on effective thermal conductivity with hydrophobic ionomer surface.	81
Figure 5.33	Impact of different pressure gradients on water distribution with $S=40$ and hydrophobic ionomer surface shown in three slices through the CL structure: a) $\delta p=3.2e-5$ ($=5.4$ KPa) b) $\delta p=4.8e-5$ ($=8.1$ KPa)	82

Figure 5.34	Impact of different pressure gradients on water distribution with $S=70$ and hydrophobic ionomer surface shown in three slices through the CL structure: a) $\delta p=3.2e-5$ ($=5.4$ KPa) b) $\delta p=4.8e-5$ ($=8.1$ KPa). (Green represents carbon, yellow is ionomer, blue is gas filled pores, and red water filled pores) . . .	83
Figure A.1	Impact of different pressure gradients on effective water-vapour diffusivity with hydrophilic ionomer surface.	87
Figure A.2	Impact of different pressure gradients on effective thermal conductivity with hydrophilic ionomer surface.	87
Figure A.3	Impact of different pressure gradients on effective oxygen diffusivity with hydrophilic ionomer surface.	88
Figure A.4	Impact of different pressure gradients on effective oxygen diffusivity with hydrophilic ionomer surface.	88
Figure A.5	Impact of different pressure gradients on effective thermal conductivity with hydrophilic ionomer surface.	88

Nomenclature

Acronyms

<i>BGK</i>	Bhatnagar Gross Krook
<i>CCL</i>	Cathode Catalyst Layer
<i>CLs</i>	Catalyst Layers
<i>ECSA</i>	Electrochemical Surface Area
<i>FIB</i>	Focused Ion Beam
<i>FV – PSM</i>	Finite Volume - Pore Scale Model
<i>GDL</i>	Gas Diffusion Layer
<i>LBM</i>	Lattice Boltzmann Method
<i>LGCA</i>	Lattice Gas Cellular Automata
<i>MPL</i>	Micro Porous Layer
<i>MRT</i>	Multiple-Relaxation-Time
<i>NMRI</i>	Nuclear Magnetic Resonance Imaging
<i>PEMFCs</i>	Proton Exchange Membrane Fuel Cells
<i>PNM</i>	Pore Network Model
<i>PSM</i>	Pore Scale Model
<i>REV</i>	Representative Elementary Volume
<i>SEM</i>	Scanning Electron Microscope

TEM Transmission electron microscope

VOF Volume of Fluid

Symbols

α Charge Transfer Coefficient

δp Pressure Differences across Computational Domain[Pa]

δt_{LB} Lattice Time Step

Δt_p Physical Time Step[s]

δx_{LB} Lattice Length Scale

Δx_p Physical Length Scale[m]

η Overpotential[V]

γ Wetting Potential

Λ_i Diagonal Relaxation Matrices

μ Dynamic Viscosity[$N.s/m^2$]

μ_c Chemical Potential[J/mol]

ν_{LB} Lattice Kinematic Viscosity

ν_p Physical Kinematic Viscosity[m^2/s]

ϕ Order Parameter

ϕ Porosity

ϕ_s Solid Phase Order Parameter

Π Peltier Coefficient

ψ_s Surface Energy Density

ψ Free Energy Density

ρ Density[kg/m^3]

σ_m	Ionic Conductivity[S/m]
σ_s	Electronic Conductivity[S/m]
σ	Surface Tension[N/m]
σ_{LB}	Lattice Surface Tension
σ_p	Physical Surface Tension[N/m]
τ_ν	Relaxation Time
θ	Contact Angle
φ_m	Electronic Potential[V]
φ_s	Ionic Potential[V]
ξ	Interface Width[nm]
a_i	Local Acceleration Component[m/s ²]
$D_{i,m}$	Diffusivity of Species in Membrane
e^-	Electron
e_i	Velocity of Each Density Distribution Function
F	Body Force[N]
f	Density Distribution Function
f^{eq}	Equilibrium Distribution Function
f^{neq}	Non-Equilibrium Distribution Function
F_{ext}	External Body Force[N]
F_f	Faraday Constant[C/mol]
H^+	Proton
H_2	Hydrogen
i_0	Exchange Current Density[A/m ²]

$J_{H_2O}^d$	Water-Vapour Diffusive Flux[$mol.m^2/s$]
$J_{O_2}^d$	Oxygen Diffusive Flux[$mol.m^2/s$]
L_{LB}	Lattice Length
L_p	Physical Length[m]
m_f	Velocity Distribution Function in Moment Space
m_g	Order Parameter Distribution Function in Moment Space
n	Vector Normal to Surface
O_2	Oxygen
P_c	Capillary Pressure[Pa]
P_g	Gas Pressure[Pa]
P_{LB}	Lattice Pressure
P_l	Liquid Pressure[Pa]
P_p	Physical Pressure[Pa]
Q	Transformation Matrix
$Q_f(f)$	Collision Operator
R	Gas Constant[J/(mol.K)]
r_{ORR}	Electrochemical Reaction Rate
T	Temperature[K]
v_i	Local Velocity Component[m/s]

ACKNOWLEDGEMENTS

I would like to express my sincere and deep appreciation to my supervisor Prof. Ned Djilali for all his advice, support, suggestions, insightful comments, and spectacular vision throughout my PhD studies. I will always be deeply thankful to him for his mentorship. I am grateful to my dissertation committee member, Prof. Henning Struchtrup . Without his invaluable comments, this thesis could not have been more accurate and more clearly expressed. I would like to specially thank Dr. Jay Sui, Dr. Belaid Moa, Dr. Andreas Putz, and Dr. Randhir Singh for their guidance and collaboration during my research at University of Victoria. I would like to deeply thank my teacher and friend at Shahid Bahonar University of Kerman, Prof. Mohammad Rahnama, for his endless support and encouragement.

I would like to thank all amazing staff at the Institute for Integrated Energy Systems of the University of Victoria (IESVic), Sue Walton and Pauline Shepherd. I deeply acknowledge the support from my friends and colleagues Mostafa Rahimpour, Dr. Behnam Rahimi, Amin Cheraghi, Dr. Afshin Joshesh, Dr. Hamed Akbari, Majid Soleimani, Ahmad Lashgar, Amin Ebrahimi, Razzi Movassaghi, Krishna Ravi, and Valerie Losier.

My deepest gratitude goes to my parents and my two lovely sisters, for being an unending source of encouragement and inspiration throughout my academic adventures. Without their encouragement, understanding and loving, this research would never have been finished.

Also, I would like to thank Automotive Partnership Canada (APC), Ballard Power Systems, Automotive Fuel Cell Cooperation (AFCC Corp.), the CaRPE-FC Network, and the Natural Sciences and Engineering Research Council of Canada (NSERC) for their financial support and Compute Canada for the computational resources throughout this research.

DEDICATION

To my lovely mother and father, Sodabeh and Ali.

To my lovely sisters, Maryam and Mahsa.

Chapter 1

Introduction

1.1 Background and Motivation

Due to their high energy efficiency (generally between 40-60%, or up to 85% efficient in cogeneration systems), low emissions, and low noise, proton exchange membrane fuel cells (PEMFCs) have attracted more and more attention over the last decade as a candidate alternative power source in the automotive industry and in other portable power devices [1]. Although acceptable performance levels have been achieved, high cost and durability concerns are preventing full-scale commercialization of the technology [2]. These challenges are to a large extent associated with the catalyst layers (shown in Fig. 1.1), which play an important role in PEM fuel cells. They provide electrochemical sites using Pt elements, conduct ions through ionomers, transfer electrons using carbon spheres, and carry water generated from an electrochemical reaction through the pore structures. The transport of product water has a significant influence on PEMFC performance [3-5]. To maintain high proton conductivity in PEM fuel cells, the membrane must be kept well hydrated, but too much water in the cathode catalyst layers can cause flooding of the catalyst layers (CLs), the gas diffusion layer (GDL), the micro-porous layer (MPL), or the gas flow channel, thus inhibiting gaseous reactant transport to the reaction sites [6, 7]. Water management is therefore a critical issue in PEMFC performance, especially for the cathode catalyst layer. Recent research has shown that lifetime performance losses in PEMFCs are dominated by CL degradation [8]. A significant performance loss was reported after 1000 start/stop cycles due to reduced CL porosity and the concomitant loss in transport properties. Accordingly, a detailed understanding of CL microstructure

is of paramount importance in our efforts to understand PEMFC performance and degradation issues. One way to understand more fully and to quantify CL degradation mechanisms is to characterize fully the morphology and effective properties before and after degradation. The overall strategy to achieve this at the Energy Systems and Transport Phenomena Laboratory at the University of Victoria is to: i) characterize the structure of sample CLs using advanced electron microscopy (FIB-SEM); ii) perform physically representative numerical reconstructions of CL samples; iii) perform pore-scale simulations of salient transport phenomena; and iv) derive the effective transport parameters as a function of CL and liquid water morphology. The array of transport phenomena taking place in the CL includes transfer of mass, momentum, heat, and charged species in conjunction with reaction kinetics. The main focus of this thesis is on one of the most challenging processes occurring in PEMFCs: the dynamic transport of liquid water in the CL. The objectives are to quantify the characteristics of water transport in PEMFC catalyst layers and to gain insights into its impact on performance and durability. A multi-phase multiple-relaxation-time (MRT) lattice Boltzmann method (LBM) is used to simulate water transport in the reconstructed catalyst layer. The choice of MRT-LBM is based on its suitability for modelling and simulating multi-phase flow phenomena with high density and viscosity ratios (e.g., air and liquid water) in complex geometries such as the porous structures of PEM fuel-cell components.

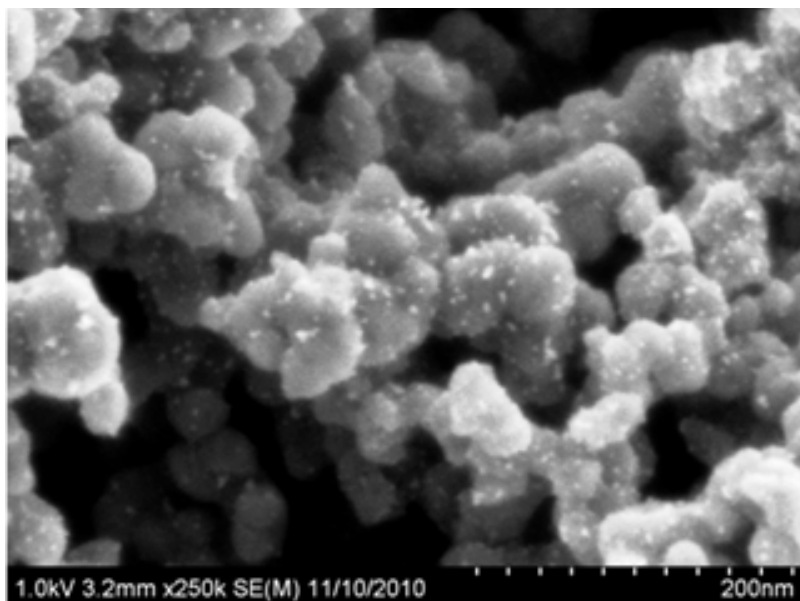


Figure 1.1: SEM image of a PEM fuel-cell catalyst layer (ESTP Laboratory, University of Victoria, unpublished).

1.2 Fuel Cell Performance and Water Generation Reaction

A fuel cell is an electrochemical device that changes the released energy of a reactant into electricity. Polymer electrolyte membrane fuel cells (PEMFCs) have been the technology of choice in the automotive industry because they offer zero tailpipe emission, highly efficient performance, and adaptability to low-temperature operating conditions. A schematic of a PEMFC is shown in Fig. 1.2. A PEMFC unit consists of three main components: a membrane, two electrodes (anode and cathode), and bipolar plates. At the anode electrode, hydrogen is supplied to the fuel cell unit and is converted to electrons and protons by the electrochemical reaction expressed by Eq. (1.1) [3]. The membrane layer, which conducts protons produced at the anode electrode, is the heart of a PEMFC. The most commonly used type of membranes have a conventional polymer structure with a high band gap making them electrical insulators. Electrons are therefore transferred from the anode electrode to the cathode through an external circuit via the conductive bipolar plates. At the cathode electrode, the protons and electrons that have migrated through the membrane and the external circuit, respectively, as well as the oxygen fed to the cathode electrode come

together and react according to Eq. (1.2) [3]. The schematic of this process is illustrated in Fig. 1.3. Water is the only byproduct of this reaction which is ejected from the fuel cell system through the exhaust tail pipe of cars (zero tail-pipe emission). Figure 1.3 shows the three main components of a cathode electrode. A half-unit cell comprises a GDL, an MPL, and a CL. The GDL and MPL are mainly made of carbon fibres and carbon spheres, respectively, which conduct electrons. The CL is composed of four main elements: i) carbon spheres, which transfer electrons; ii) an ionomer, which conducts protons; iii) platinum (Pt), where the electrochemical reactions occur; and iv) pores, which facilitate the transport of reactants and products (e.g., oxygen, water vapour, and liquid water) arising from the anodic and cathodic reactions:



Water generated based on this electrochemical reaction (Eq. 1.2) must be removed from the fuel-cell system to avoid blocking oxygen pathways and maintain performance. Understanding the dynamics of liquid water can result in improved performance and help quantify some of the degradation mechanisms occurring in PEMFCs.

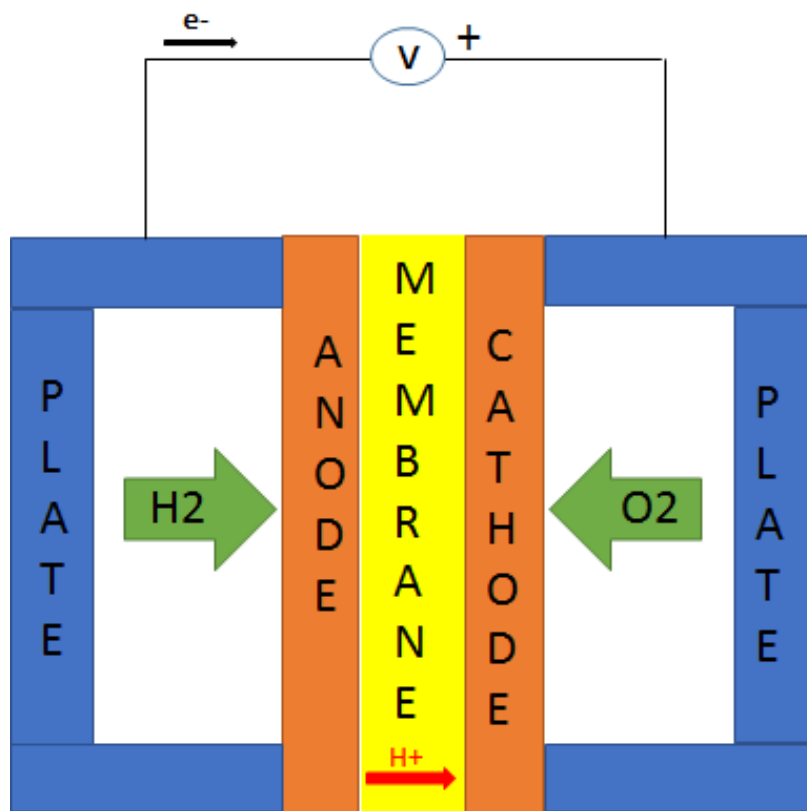


Figure 1.2: Schematic of a PEM fuel cell unit

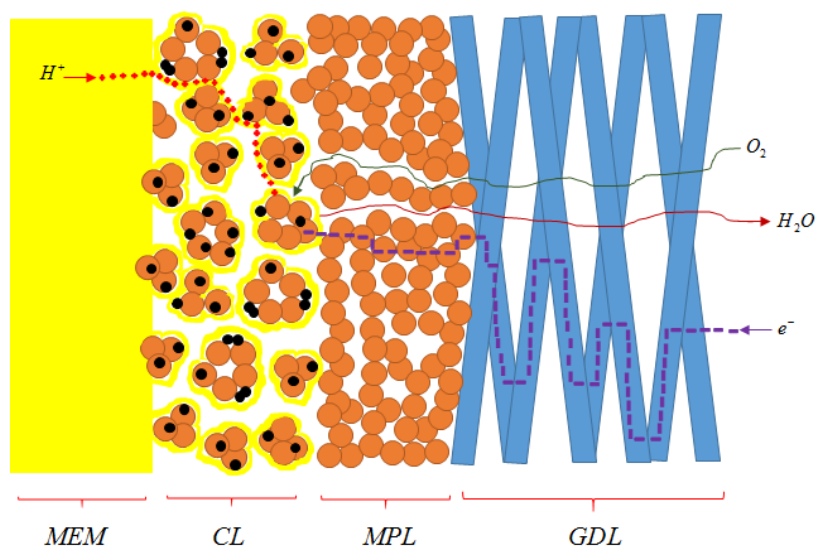


Figure 1.3: Schematic of a half-cell unit (Cathode electrode)

1.3 Thesis Organization

The main focus of the research described in the present thesis is to characterize the dynamic transport of liquid water and its impact on the effective transport properties in the catalyst layer of PEMFCs. The thesis is organized in six chapters. The background and motivation are presented in Chapter 1, along with an overview of fuel cell operation and performance, and of the role of the water generation by the electrochemical reaction. Chapter 2 provides a literature review of CL characteristics relevant to fuel cell performance, degradation and durability, nano-structural characterization of the CL, experimental visualization techniques to observe liquid water in an operating PEMFC, and relevant aspects of more general multi-phase flow simulations in porous media. In Chapter 3, the physically based numerical reconstruction of CL samples to generate the computational domains used for the simulations is discussed. The methodology used to investigate liquid water transport dynamics and its impact on the transport properties is presented in Chapter 4. Chapter 5 provides the evaluation, analysis, and comparisons of simulated results including validation of the developed and deployed numerical methodologies. Finally, conclusions and future work are outlined in Chapter 6.

Chapter 2

Literature Review

The following sections provide a literature review of CL characteristics relevant to fuel cell degradation and durability, nano-structural characterization of the CL, and relevant aspects of more general multi-phase flow simulations in porous media.

2.1 Performance and Degradation in Fuel cells: CL Morphology and Water Effects

One of the major thrusts in current fuel-cell research is understanding degradation mechanisms and improving durability and performance, which are inherently influenced by the materials used in the system [1, 2, 5, 8–11]. Degradation in PEMFC systems is primarily dominated by degradation of the membrane and catalyst layer, although degradation mechanisms typically involve cross-component links and depend strongly on operating conditions. A recent study reported, for instance, a significant performance loss after 1000 start/stop cycles due to reduced CL porosity [8]. The membrane in this study was virtually unaffected; Pt coarsening was similar to a case where the PEMFC was subjected to 24,000 voltage cycles without any substantial performance degradation. Hence, the performance loss was attributed to porosity loss with concomitant loss in CL transport properties. The particular degradation mechanisms that led to porosity loss are not entirely clear, but were attributed in part to collapse of the pore structure due to carbon corrosion. Carbon corrosion in the CL has been reported to occur mainly due to local fuel starvation and to start-up/shutdown processes [9]. Local fuel starvation results from reducing gas diffusivity in GDL due to the flooding of this porous layer. In the case of start-up/shutdown processes, following

hydrogen purging, some portion of anode channel can fill with air which results in current reversal and triggering carbon corrosion. This degradation mechanism gives rise to loss of carbon support as well as of Pt particle connectivity resulting in a loss of active area of the porous CL available for reaction and consequently a drastic decrease in performance [9]. In addition, membrane degradation corresponding to re-deposition of Pt under specific operating conditions is intimately linked to CL stability, and Pt precipitates in the membrane have been identified as a potential cause of increased membrane/cell ohmic resistance in an aged vehicle PEMFC [2, 8, 9]. Furthermore, the origin of many of the radicals that attack the ionomer phase in the CL and at the CL-membrane interface can be traced to the CL [12]. The most important factor affecting PEMFC degradation and performance is linked to the presence of liquid water generated by the electrochemical reaction in the CCL [1, 2, 5, 10]. Liquid water has a noteworthy impact on performance due to its impact on reactant transport and is one of the root causes of accelerated carbon corrosion and Pt dissolution in CCLs due to hindering of reactants pathways and consequently the local fuel starvation. Under fuel-cell operating conditions, especially at higher current densities, whenever the rate of liquid water generation is higher than the rate of water removal from the system, the fuel cell is referred to as flooded [10]. In this situation, accumulated liquid water blocks reactant pathways to reaction sites (Pt locations) and reduces active reaction area (ECSA). In summary, flooding reduces fuel-cell performance and reliability, and can induce degradation under unchanged operating conditions. Besides being at the crossroad of degradation pathways in the membrane, the CL (mainly on the cathode side) is the principal source of fuel-cell efficiency losses. Hence, a detailed understanding of CL microstructure is of paramount importance to understand and eventually to mitigate PEMFC performance and degradation issues.

2.2 Catalyst Layer Microstructure Characterization and Reconstruction

Proper characterization of the nano-structure of PEM catalyst layers is a prerequisite to full understanding of transport phenomena. Experimental characterization of CL nano-scale structure is challenging because the distribution of the various phases (carbon, ionomer, Pt, and void) is difficult to resolve even with new advanced microscopic techniques. A clear distinction between carbon and ionomer has not yet been made

due to the limitations of advanced microscopic facilities [13,14]. Hence, some authors have reconstructed CL structures to explore transport properties through CLs using either an idealized CL structured approach [15] or a random approach [13, 14, 16]. The latter approach has mostly been developed based on experimental data obtained from advanced microscopic facilities in conjunction with stochastic techniques.

Lange et al. [14], for instance, used a stand-alone focused ion beam (FIB) and a stand-alone scanning electron microscope (SEM) to cut and sequentially image slices of the interior structure of the CL. Using the stack of carefully post-processed images, a computational reconstruction of the catalyst layers was performed using a simulated annealing method. Mukherjee et al. [16] used TEM experimental images to derive two-point correlation functions to reconstruct a CL structure based on a coarse-mesh stochastic reconstruction. Kim and Pitsch [17] reconstructed CL geometry by matching the experimental pore-size distribution obtained by mercury intrusion porosimetry and the pore-size distribution used in computational CL reconstruction using simulated annealing optimization. Siddique et al. [18] proposed a reconstruction algorithm that attempted to mimic the experimental procedure of CL fabrication. Singh et al. [13] computationally reconstructed a CL based on data obtained from a dual-beam FIB/SEM. The CL structure was optimized using a simulated annealing technique reinforced by two different cost functions: the first based on the two-point correlation function derived from FIB/SEM experimental data, and the second associated with the difference in the number of pore pixels between the experimental data and the corresponding reconstructed image. Their study showed that the two-point correlation function corresponded to a statistically better representation of the CL structure, with higher fidelity [13]. Furthermore, they pointed out that the two-point correlation function offered higher computational efficiency than its counterpart.

Each of these techniques has its pros and cons. Methods based on purely stochastic reconstruction are computationally efficient, but do not necessarily represent real CL morphology. Reconstructing 3D CL nanostructure based on experimental data using advanced microscopy facilities such as FIB/SEM can provide more accurate details on CL structure, but is expensive.

Determining effective transport properties, e.g., oxygen and water-vapour diffusivities, throughout the CL depends not only on CL morphology, but also on CL liquid water distribution. Hence, the dynamics of liquid water in the porous structure of cathode CLs needs to be investigated further both experimentally and numeri-

cally [1, 2, 5, 19–22].

2.3 Experimental Observation of Liquid Water Dynamics in Fuel Cells

Liquid water dynamics and transport have a significant impact on the performance and durability of PEMFC components, especially the cathode catalyst layer (CCL). It is therefore crucial to understand the physics of liquid water transport through these fuel-cell components. To visualize the salient features of liquid water dynamics, four main visualization techniques have been used: direct visualization, nuclear magnetic resonance imaging (NMRI), beam interrogation, and fluorescence microscopy [7, 23].

Although these imaging techniques can all be applied to PEMFCs, each of them has its own advantages and disadvantages. The main barrier to observing liquid water with these imaging techniques is their limited spatial and temporal resolution [7, 23]. Furthermore, traditional GDL and bipolar plates in PEMFCs are made of opaque materials [7, 23]. As a result, in-situ visualization of liquid water distribution and dynamics is challenging.

Among the visualization techniques mentioned above, direct visualization, e.g., using infrared cameras, digital camcorders, and CCD cameras, has been frequently used to look into the emergence, growth, and transport in channel flow of liquid water using a transparent cell [7, 23, 24]. However, use of this technique is limited by the lack of depth perception in available cameras and the highly reflective nature of GDL materials [7, 23]. Fluorescence microscopy [25, 26] is the second technique used to explore liquid water dynamics, mostly on the surface of GDLs. As stated in [23, 27], this method is limited to a depth of a few fibres into the GDL due to its opaque material.

High-resolution beam interrogation and NMRI devices have been recently adapted and developed to enable characterization of the liquid water distribution through the various PEMFC components [7, 23]. Unlike their counterpart techniques, these techniques can capture the dynamics of liquid water even through opaque materials. In spite of these improvements, the NMRI technique is mostly used to visualize liquid water in membrane, land, and flow channels due to the sensitivity and incompatibility of magnetic signals with carbon materials [7, 23, 28].

Beam interrogation techniques, e.g., neutron imaging, X-ray techniques, and elec-

tron microscopy, are widely used to investigate liquid water distributions in the through-plane and in-plane directions of PEMFC porous structures. Among the beam interrogation techniques, X-ray radiography [29–37] has been recently used and demonstrated to be able to visualize liquid water dynamics in a cathode catalyst layer in an operating fuel cell with spatial and temporal resolutions of 0.5 μm and 2 sec/frame respectively [32].

Understanding and observing liquid water in porous catalyst media is a challenge even with new advanced microscopic facilities due to the need for a high-resolution microscope that can resolve liquid water transport in the nano-pores of porous media. Deevanhxay et.al [32] resolved for the first time the presence and accumulation of liquid water inside a cathode catalyst layer. They conducted an experiment that used soft X-ray radiography in conjunction with electrochemical impedance spectroscopy to demonstrate the variability of liquid-water accumulation in the CCL. They elucidated the presence of higher liquid-water saturation on the CL/GDL side than on the CL/MEM side. They also pointed out that with increasing current density and over time, more liquid water was resolved in the cathode CL, especially under the rib portions.

In spite of recent progress in observing liquid water in CCLs, much more effort is necessary to understand the dynamics of liquid water numerically using two-phase flow models because imaging techniques with their limited resolutions still cannot capture and resolve water transport through CCL nano-structures.

2.4 Theoretical Methods for Two Phase Flow in Porous Media

A wide variety of practical applications involve multi-phase flow transport, heat transfer, and multi-component mass transfer in porous media. These include thermally enhanced oil recovery, capillary-assisted thermal technology, and water intrusion through packed beds, as well as transport in PEM fuel-cell electrodes. A combination of viscous, thermal, and interfacial forces governs the transport and distribution of water in PEM porous electrodes. Understanding and modelling of water movement and distribution and the conditions that lead to specific regimes can inform improved design for fuel-cell performance. Various models have been developed and proposed to analyze two-phase flow in porous media.

One of the first methods proposed to investigate two-phase flow in PEM fuel cells was based on the unsaturated flow theory (UFT) [21]. In this method, a constant pressure of the gas phase is assumed, and consequently the pressure gradient of the liquid phase is equal to the negative of the capillary pressure. An expression of Darcys law for liquid phase flux was obtained and combined with the liquid continuity equation to yield the velocity and saturation of liquid water.

The multi-phase mixture model is another method developed to model two-phase flow, which unlike the UFT method, does not need to assume constant gas pressure. This method is based on a reformulation of the classical two-phase model equations into a single equation. The interfacial tension effect and wettability potential are fully accounted for in this method [38,39]. Assuming a mixture velocity and density for the gas and liquid phases, the liquid saturation was obtained according to a non-linear first-order equation. Using the liquid saturation, the individual velocities and densities of the gas and liquid phases and their corresponding pressures were computed. This model is suitable for modelling two-phase flows in cases of high capillary numbers and when gas pressure is the dominant force on the liquid [40]. Another method that has been used to simulate two-phase flow in PEM fuel-cell porous electrodes is the multi-fluid model [41]. In this method, unlike the mixture model and UFT, two separate sets of equations were used to capture the hydrodynamic behaviour of liquid and gas fluids, and their field equations were linked using the relative permeabilities of the fluids. One of the advantages of this method compared to the mixture model is that it can be used to simulate high-saturation cases [40].

All these models are macroscopic models and solve two-phase flow using a representative elementary volume (REV) characterized by effective properties but without resolution of the pore structure. The determination of the effective properties for REV modelling becomes challenging when the porous media have a complex three-dimensional heterogeneous and disordered geometry and when the scales approach the molecular mean free path. Numerically tracking phase interfaces and calculating surface tension forces become computationally expensive, and theoretical inconsistencies may exist in some studies [42]. Therefore, it is desirable to develop a pore-scale model to study two-phase flows that can resolve fundamental pore-level phenomena.

Among pore-scale models for fuel-cell porous structures, the volume of fluid (VOF) model, the pore network model (PNM), and the lattice Boltzmann method (LBM) are widely used. The PNM uses an idealized and simplified porous structure containing a network of interconnected spherical pores and throats [6,43–46]. In this idealized pore-

scale model, simplified hydrodynamics equations are solved to simulate two-phase flow. Therefore, pore network simulations mostly rely on a simplified morphology and topology of a heterogeneous porous medium. As a result, the idealized PNM usually cannot accurately represent an actual and realistic porous geometry and account for two-phase transport through porous structures. The VOF model is another two-phase model that is extensively applied to the gas channel to predict water transport in PEMFCs [47,48]. In this method, the Navier-Stokes equations and a volume fraction function are solved to determine the dynamics of each phase and of the interface. The interface is reconstructed in each time step based on the volume fraction in such a way that a time-consuming computational re-initialization algorithm is a prerequisite for this method. Due to this drawback, this method is less widely used in 3D simulations of heterogeneous porous geometries [49–51]. The LBM is another two-phase method that is a sophisticated and robust tool for simulating multi-phase flow in porous media. This method can provide more realistic and efficient pore-scale dynamic simulations of water transport in porous geometries, as will be discussed in more detail in the following sections.

2.5 Multi-Phase Lattice Boltzmann Method

The LBM originated from lattice gas cellular automata (LGCA) [52]. In LGCA, the fluid is modelled by discrete particles moving on predefined trajectories at constant velocities. Particles collide in accordance with predefined collision rules and trajectories. Due to the discrete nature of the colliding particles, this method is prone to substantial local fluctuations. This drawback of LGCA models has been resolved by LBM, which involve a density distribution function instead of single particles at each lattice site [53]. Due to its kinetic origin, the LBM provides some distinctive features, including ease of programming, an intrinsic parallelism algorithm, and manipulation of complex boundaries and multi-phase multi-component flows. These characteristics make LBM very effective in dealing with complex boundary conditions [54] and multi-phase, multi-component problems [54–60].

Four main LBM models have been proposed to investigate multi-phase flow through porous media: the colour-fluid model developed by Gunstensen et al. [55], the interparticle-potential model proposed by Shan and Chen [56], the free-energy model developed by Swift et al. [57], and the mean-field theory model provided by He et al. [58].

The colour-fluid model (blue and red colours) is based on the two-phase immiscible

lattice-gas model proposed by Rothman and Keller [59], which has been modified by Grunau et al. [60] to account for density and viscosity variations. This model is based on red and blue particle distribution functions representing two different fluids. To model surface tension, a perturbation step is added to the original collision operator. To simulate a sharp interface and implement phase separation, a segregation operator is added to enforce movement of fluid particles to their own colour region [61]. To perform the segregation step, the particles must be redistributed by means of a very inefficient algorithm that causes anisotropic surface tension and non-physical vortices near the interface [62, 63]. Several studies have been carried out to address and resolve these drawbacks. Recently, Reis and Philips [61] modified the original colour-fluid model by introducing a two-phase flow operator to recover the single-phase NS equations and proposed a surface tension term. Lishchuk et al. [62] used a new continuum surface force to model surface tension directly at the interface. They noted a significant decrease in spurious velocities at the interface, leading to improved isotropy at the interface. Latva Kokko and Rothman [63] proposed a new segregation model called a diffusion scheme that overcomes the lattice pinning problem that occurs with the original proposed colour fluid model and creates a symmetric particle distribution around the interface.

The interparticle-potential model proposed by Shan and Chen [56] is based on the concept of nearest-neighbor interactions which consider the microscopic interaction forces between particles. To model interaction between the fluids, a collision operator considering interactive forces between particles was added to original collision operator to take into account surface-tension forces and account for phase separation. The original Shan and Chen model compared to color fluid model is capable of handling multiphase flow with isotropic surface tension. But it should be noted that the collision operator in the Shan and Chan model does not satisfy local momentum conservation compared to the color-fluid model which conserves momentum locally. However, the momentum is globally conserved when boundary effects are excluded [64, 65]. Separation scheme in this model is automatic which makes a positive contribution to this model, but leads to generate a thicker interface compared to that one captured by the color fluid model which make it difficult to distinguish exact location of interface by this model [64, 65].

The free-energy model proposed by Swift et al. [57] introduced a free-energy function to consider interface and surface tension effects in a thermodynamically consistent manner. Unlike the two previous models, this model considered the total density and

the density difference of the fluids as simulation parameters instead of the density of each phase. The total density parameter recovers the velocity field, and the density difference parameter tracks the interfaces between the phases. The lack of Galilean invariance in this model was resolved in work described in [66,67]. This approach is best suited to generating a consistent model of the equilibrium distribution based on thermodynamic concepts [67–69]. Consequently, conservation of total energy, including surface energy, kinetic energy, and internal energy, is precisely satisfied [68]. This model is well adapted to model multi-phase flow with high density ratios and different viscosity ratios. Recently, Niu et al. [66], Zheng et al. [69], and Inamuro et al. [67] proposed two new free-energy models that could simulate multi-phase flows with high density ratios (up to 1000). Niu et al. [66] and Zheng et al. [69] used two sets of distribution functions to recover the Navier-Stokes equation and the Cahn-Hilliard equation, which tracks the evolution of the interface. Inamuro et al. [67] introduced two new sets of distribution functions to recover these equations and included a pressure correction to enforce continuity in each iteration. Several deficiencies of free-energy models [67] have been reported [66,69]. The pressure projection method used by Inamuro et al. [67] increases computing cost significantly, and this method may also produce non-physical results in some test cases [69].

One other multi-phase LB method worth noting is the mean-field theory model proposed by He et al. [58], which gives acceptable results in the nearly incompressible limit for non-ideal gases. In this model, two sets of distribution functions are used, one to simulate the pressure, and a second index function that tracks the interface between the two fluids. However, this model cannot completely recover the Cahn-Hilliard equation, which tracks the evolution of the interface [58].

Each of these models has been used to simulate two-phase flow problems in different geometries, especially in complex geometries such as porous media. For instance, Pan et al. [65] simulated two-phase flow in a reconstructed packed-sphere bed using an LBM approach. Good agreement was achieved between the measured capillary pressure-saturation relation and the LBM simulations. In addition, some studies using LBM to study PEM-FC transport phenomena in the GDL have also been carried out. Hao and Cheng [70] investigated the effects of different wettability potentials of the fibre structure of a reconstructed 3D carbon-paper GDL on relative permeability. In their research, good agreement between LBM results and the power-law correlation between relative permeability and saturation was achieved. Sinha et al. [43] simulated liquid water drainage and water distribution in a reconstructed non-woven GDL mi-

crostructure using a two-phase LBM model. Hao and Cheng [71] looked at the effect of wettability on water transport in the GDL by simulating water invasion into a fully saturated GDL using the multi-phase free-energy lattice Boltzmann method. Their results showed that wettability plays a significant role in water saturation distribution. With the same capillary numbers, they investigated two datasets in a porous medium with highly hydrophobic and neutral porous media. They pointed out that for hydrophobic surfaces in porous media, water transport behaves like a capillary fingering regime. They also stressed that for neutral-wettability solid-structured samples, water transport moves as a stable displacement. Hao and Cheng [72] compared the capillary pressure results in a carbon-paper gas diffusion layer having hydrophilic and hydrophobic pores by both LBM and experimental measurement. Their results expressed that pore-scale simulated drainage and capillary imbibition pressures were in good agreement with obtained experimental data. Gao et al. [73] stated that as the pressure gradient imposed on water invading a reconstructed GDL increases, the water distribution in the hydrophobic GDL shows a channeled pattern, but in the case of a hydrophilic GDL, a piston-flow pattern was obtained.

None of the above studies have considered water transport in the GDL for high density and viscosity ratios. Niu et al. [66] are amongst the few who have tackled this problem and investigated water transport through a reconstructed GDL using a high-density-ratio, multi-phase, multi-relaxation-time free-energy lattice Boltzmann method. They examined the effects of various parameters, including pressure gradient, wettability, and viscosity ratio, on the relative permeabilities of water and air in a reconstructed GDL. Moriyama and Inamuro [74] studied the effect of different GDL wettabilities in conjunction with gas channel flow on water distribution using a high-density-ratio, free-energy LBM method. They concluded that for a hydrophilic structure, water penetrates through small pores, whereas for a hydrophobic one, water moves through bigger pores. Some studies have also investigated experimentally the issue of water transport through a GDL. Lister et al. [26] used fluorescence microscopy to observe water transport through a GDL. They found water transport in the GDL structure was mostly dominated by the capillary fingering pattern rather than the converging capillary-tree water-transport mechanism proposed by Nam and Kaviani [75]. Although many efforts have been made to elucidate water transport and its consequences in PEM fuel-cell components, water transport through the catalyst layers has been less thoroughly studied. Only a few studies have been done on this issue, and none of them has considered high density and viscosity ratios. Mukher-

jee et al. [76] studied the effect of different capillary forces on water patterns in a reconstructed catalyst layer using a lattice Boltzmann method. A capillary fingering pattern was observed in the catalyst layer under the normal operating conditions of a PEM fuel cell. Furthermore, they stated that when capillary pressure was increased in the catalyst layer, the water pattern transitioned from capillary fingering to a stable displacement pattern. Like other researchers on the GDL, they did not consider the effect of high density ratio. Moreover, they did not report the impact of different viscosity ratios, surface tension, or CL material contact angles on water transport. Meanwhile, an optimized value for the contact angle of the catalyst layers under different operating conditions remains to be determined. To the best of the authors' knowledge, no study has reported an optimized wettability value of catalyst layer materials. High-density-ratio MRT-LBM has not yet been used to investigate water transport and patterns in a reconstructed catalyst layer.

In this thesis, MRT-LBM is used based on the method developed by Niu et al. [66]. The basic principle of this method [77] is the mean-field diffusive interface theory, which has been shown capable of simulating multi-phase flows with high density and viscosity ratios. The present MRT-LBM provides viscosity-independent permeability predictions, which is a very important physical consistency attribute in simulating multi-phase flows. Niu et al. [66] stated that in their model, the surface tension and the wetting boundary conditions do not need to be obtained implicitly, but can be computed explicitly and compared to the model proposed in [78], which requires an implicit treatment of interface tension. Details of the method are provided in Chapter 4.

2.6 Impact of Liquid Water on Transport Properties

Due to the nano-scale nature of the cathode CL pore structures as well as the complex reactive processes involved in the cathode electrode, direct experimental observation of the underlying phenomena and capture of transport dynamics are not possible even with new advanced microscopic facilities. It is therefore desirable to develop a numerical method that can investigate transport phenomena in the nano-porous structure of cathode CLs.

In this study, a coupling of two numerical methods, namely a two-phase lattice

Boltzmann method (LBM) and a finite volume-based pore-scale model (FV-PSM), is used to elucidate the dynamics of liquid water and its impact on the transport of reactant species in a three-dimensional numerically reconstructed CL.

Determining changes in effective transport parameters after long hours of operation is still not well understood. Numerous mathematical models have been used to explore transport properties through CLs. Some of these studies have considered the CL as a macro-homogeneous medium and investigated its transport parameters. The thin-film, discrete-volume, and agglomerate models have been widely used to describe transport properties through CLs. Among these methods, the agglomerate model has been shown to be the most accurate [79]. However, this method cannot rigorously represent effective transport values in the porous CL because it uses empirical relationships linking bulk properties to the effective properties of the porous CL [80]. A more rigorous solution with higher fidelity in determining the transport properties from the CL nano-structure requires resolving the microscale transport by solving the appropriate governing transport equations over the 3D nano-pore structure of a reconstructed CL, and thereafter computing effective transport properties by averaging over the representative elementary volume (REV).

Due to the complexity of the cathode CL nano-porous structure, a sophisticated pore-scale model (PSM) in conjunction with a robust reconstructed CL consolidated with experimental data obtained by FIB/SEM can be effective in resolving CL micro-structures and elucidating transport parameters.

Lange et al. [81, 82] used an FV-PSM to discretize and solve diffusive transport and reaction kinetic fluxes of different species and charges over a 3D reconstructed CL. The effective oxygen and water-vapour diffusivities and the proton and electron conductivities were computed and showed that Knudsen diffusion plays an important role in limiting oxygen transport through CLs, as the pores in CLs have dimensions in the range of 10-100 nanometers and the corresponding Knudsen number is of order unity. They noted that proper estimation of Knudsen diffusion in arbitrarily shaped pores is critical and emphasized that using the Derjaguin correction yields computational results that are much closer to experimental data. Mukherjee et al. [16] used direct numerical simulation (DNS) to solve for transport properties considering the effect of Knudsen diffusion. They emphasized that a stochastic reconstruction method based on TEM images along with the DNS model could be an effective way to explore transport properties in the cathode CL. Kim and Pitch [16] used a higher-order lattice Boltzmann method to evaluate the effective diffusivity of a

reconstructed CL. Their results highlighted the strong effects of Knudsen diffusion on reactant gas transport, especially at near-atmospheric pressures [17]. Randhir et al. [13] used an FV-PSM to determine the effective transport values of oxygen and water-vapour diffusivities, proton and electron conductivities, and thermal conductivity. The obtained effective properties were shown to agree reasonably well with measured experimental data reported in the literature.

None of the studies described above has taken into account the effect of liquid water on effective transport properties. Water management is a critical issue in terms of PEM fuel-cell performance and durability, especially for the cathode CL. Several pore-scale and meso-scale approaches have been used to model two-phase flow through the 3D micro-structure of PEM fuel-cell components. The lattice Boltzmann method (LBM), the pore network model, and the volume of fluid (VOF) model are three methods that are extensively used to investigate water transport through PEM fuel-cell porous structures, especially in the gas diffusion layers. Among these methods, the LBM has been shown to be a novel, reliable, and robust approach to model multi-component, multi-phase flows through porous media. This method has been applied to several complex problems to address the dynamics of liquid water [53, 54, 66, 71, 73, 76, 83]. This method has been used mostly to simulate water transport through the gas diffusion layer of PEM fuel cells [54, 66, 71, 73, 83], but fewer studies have looked at the influence of liquid water in the cathode CL [76]. Among LBM multi-phase models, the free-energy model is the most widely used to explore water transport through PEM fuel-cell porous structures. This model is well known to be capable of accounting for the thermodynamics of a multi-phase system [57, 64, 66, 67, 69, 84, 85]. Furthermore, the free-energy model is also well adapted to model multi-phase flow problems with high density ratios and various viscosity ratios. Niu et. al. [66], Zheng et al. [69], and Inamuro et al. [67] introduced a free-energy model to study multi-phase flow problems with high density ratios (up to 1000). The work of Niu et. al. [66], which was applied to a reconstructed GDL, is taken into consideration in this study.

One of the key objectives of this thesis is to account for the impact of liquid water on the effective transport properties of the CL. A decrease in the diffusion of reactants to the reaction sites in the cathode CL is widely associated with blockage of air pathways with water. A model is therefore needed that can simultaneously capture water transport dynamics and simulate the underlying phenomena, such as bulk and Knudsen diffusivities, in the 3D CL nano-structure. Hutzenlaub et al. [86] studied the impact of liquid water on effective oxygen diffusivity through a 3D reconstructed

cathode CL obtained using a FIB/SEM. They used a method based on a 3D pore-size distribution to fill pores with water from smaller to bigger pores and vice versa, accounting for both hydrophilic and hydrophobic CL scenarios. They also compared the effective oxygen diffusivity considering the Knudsen effect through the cathode CL for both cases. However, in their study, they did not take into account water transport dynamics and the impact of capillary pressure in different pores. Furthermore, their reconstructed CL geometry did not include the different cathode CL phases, including carbon, ionomer, and pore phases. Hence, their study did not address the effects of the different hydrophobicities of each phase.

This work addresses the issue of liquid water impact on transport properties considering the dynamics of liquid water as well as the actual CL morphology, including carbon, ionomer, water, and pore phases. To the best of the authors knowledge, a similar study has not yet been performed. A coupled FV-PSM and a two-phase free-energy LBM were used to investigate the role of liquid water in determining the transport parameters. Details of the coupling method are provided in Chapter 4.

Chapter 3

Reconstruction of the Physical CL Model

3.1 FIB/SEM Reconstructed CL

3.1.1 CL Preparation and Image Acquisition

A schematic of a CL microstructure based on the agglomerate model is shown in Fig. 3.1. The CL was ink-printed on a standard aluminum stub for the SEM. A small edge portion of the CL, to be milled using a focused ion beam (FIB), was removed using a sharp knife. An area of interest away from the edge of the specimen was cut and imaged at 52° to the surface normal using a field-emission SEM and FIB. A schematic of the experimental imaging set-up is shown in Fig. 3.2. A contiguous series of 75 slices, 20 nm apart were sliced and imaged at 50,000X magnification, generating a final 3D domain of size $1814.75 \times 1398.25 \times 1500 \text{ nm}^3$ shown in Fig. 3.4. The experimental reconstructed sample had a per-pixel resolution of 5.95 nm in the x-y plane (i.e., the SEM-imaging plane) and 20 nm in the z-direction (z is the thickness direction at each milling stage).

3.1.2 Image Processing

The SEM images were processed in FIJI (<http://fiji.sc/>), an open source image processing software. The steps involved in image processing leading to the generation of a binary (solid-void) 3D model are depicted in Fig. 3.4. Various image-processing filters such as median and intensity normalization were used, as illustrated in Fig.

3.3. The local pore-size distribution for the experimental data based on FIB and SEM data was calculated by fitting a sphere of maximum diameter to each void voxel that did not intersect the solid region. This was achieved using a local thickness filter in the FIJI software. Reconstruction of the physical CL model (Fig. 3.3) shows the main sequence of operations to generate the thresholded images. The following procedures were carried out to find the porosity and pore-size distribution that characterized the catalyst layer sample [87]:

1. Removing Vertical Stripes due to Beam Effects

- Because the sample was exposed to the beam without depositing a protective layer, some of the images exhibited a vertical strip. The bandpass filtering function of ImageJ was used to remove the strips, following which the images were registered.

2. Registration

- The alignment of successive images is called registration. The registration problem for the present dataset consists of two parts. The systematic displacement is due to the geometric configuration of the sample, in which the SEM images were taken at an angle of 52° to the FIB milling direction. The images were stretched by a factor of 1.27 corresponding to the acquisition angle of 52° . Moreover, in the acquisition process there is a random shift between successive images due to small variations in the operating conditions such as fluctuations in the FIB-SEM electron optics. The second part of the registration was implemented with an ImageJ plug-in called StackReg. In this module, registration was performed using the Translation option. The next step was selecting the region of interest; for this purpose, the largest contiguous area of interest that percolated through all slices was cropped.

3. Segmentation

- In this step, the cropped images were divided into porous and solid components. First, image intensities were normalized to correct for intensity variations in some parts of the images due to edge effects, acquisition angle, and sub-surface effects. Intensity variation was handled by two plug-in modules in ImageJ. First, a local normalization plug-in was used

to reduce the effect of non-uniform illumination in each image. Next, the stack normalize plug-in was implemented to tune brightness and contrast in all images in the stack. After normalizing the images, the images were segmented using the ImageJ software.

3.1.3 3D Reconstruction and Pore-Size Distribution

As explained in the preceding sub-section, a PEMFC catalyst layer sample was characterized using advanced microscopic facilities (dual-beam at Simon Fraser University). The acquired data were analyzed using the ImageJ/Fiji open-source software environment in addition to MATLAB functionalities. Afterwards, a three-dimensional sample of a cathode catalyst layer, as shown in Fig. 3.4 was reconstructed based on experimental data in which the solid and pore structures of the cathode were resolved. Finally, the porosity and pore-size distribution of the structure were calculated to implement numerical simulations, especially for calculation of Knudsen diffusion and investigation of effective transport properties. The computed porosity was 34% for the reconstructed geometry. The pore-size distribution shown in Fig. 3.5, calculated from the experimental FIB/SEM data, showed a peak at about 50 nm. The local thickness function in the Fiji open-source software was used to extract the pore-size distribution.

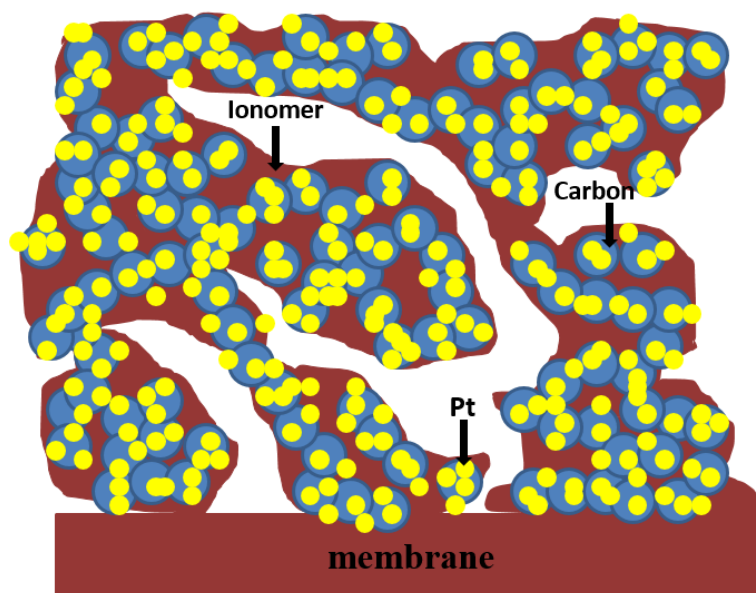


Figure 3.1: Schematic of a CL microstructure based on the agglomeration model

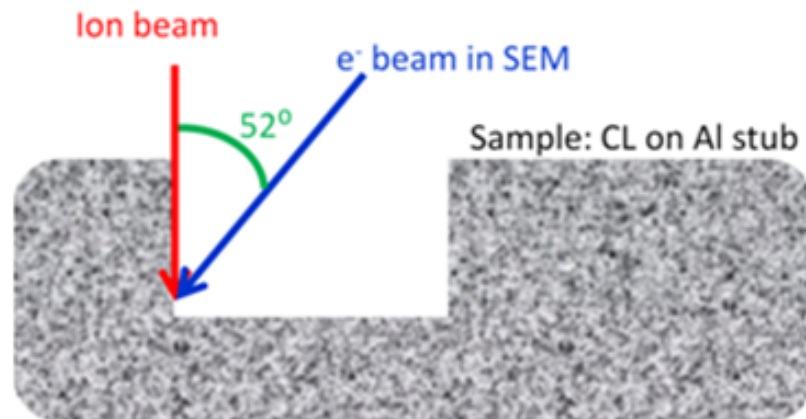


Figure 3.2: Schematic of the experimental imaging set up on Dual Beam FIB-SEM. The SEM image was taken with the electron beam inclined at 52° degrees to the ion beam

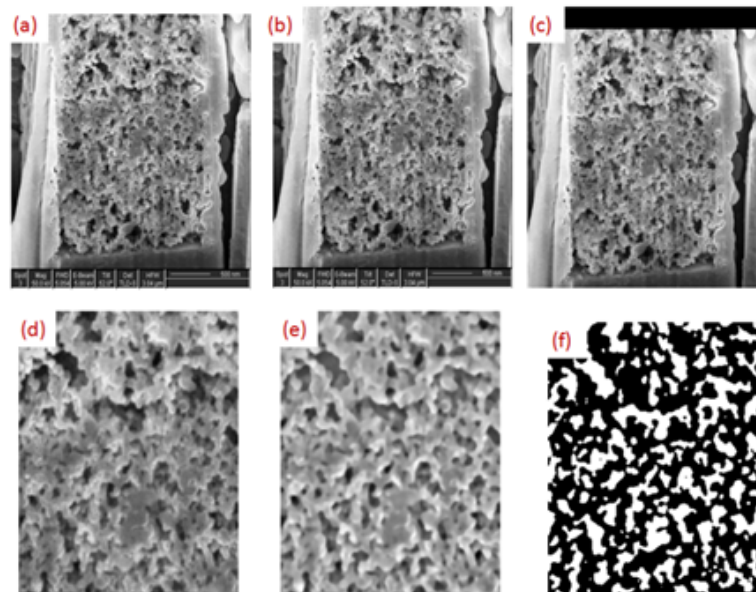


Figure 3.3: Image-processing procedure explained using a single slice at various processing stages: (a) original 8-bit gray-scale image, (b) stretched in the y-direction, (c) aligned, (d) area of interest cropped, (e) normalization applied, and (f) thresholded.

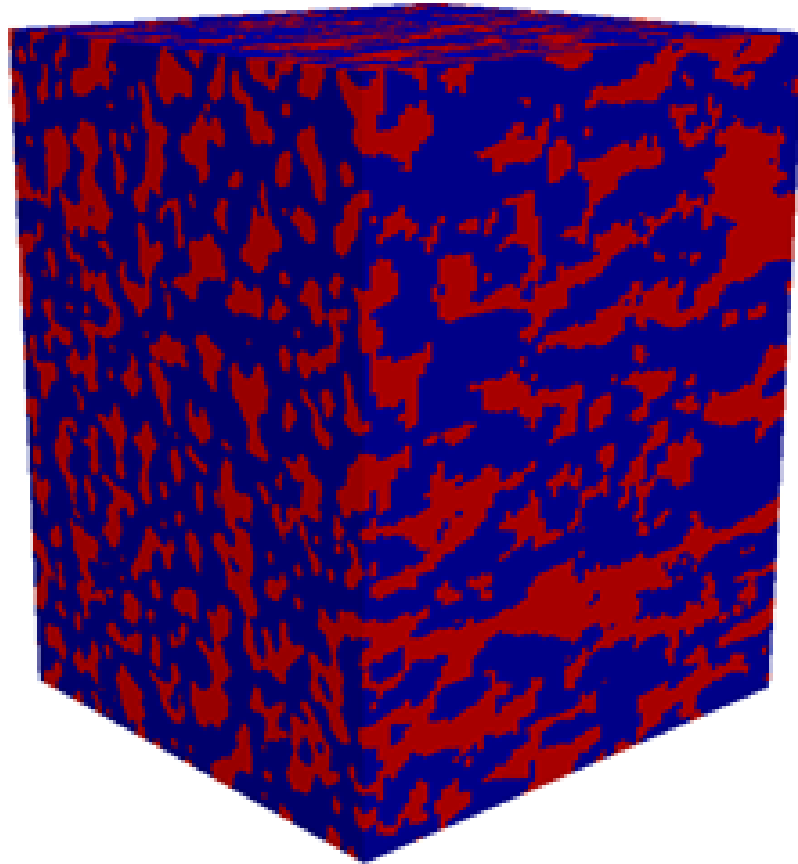


Figure 3.4: 3-D view of the reconstructed domain with domain Size: $1400nm \times 1814nm \times 1500nm$ (Red area=pore; Blue area=solid)

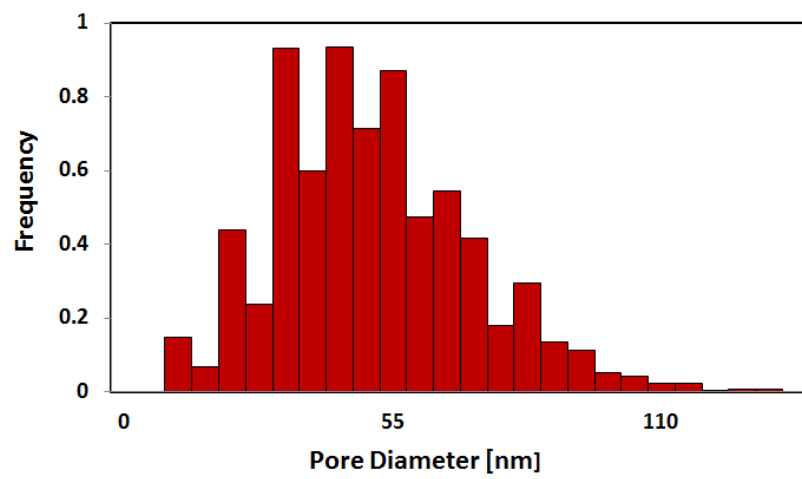


Figure 3.5: Pore-size distribution in CL, based on experimental FIB /SEM data

3.2 Stochastically Reconstructed CL

Figure 3.6 presents a flowchart of the hybrid methodology developed to reconstruct catalyst layer samples with a pores scale resolution, and the strategy used to investigate the effect of liquid water on the CL effective transport parameters. A 3D stack of images of a CL structure was acquired from a dual-beam FIB/SEM. The CL preparation and data acquisition procedures were discussed in the preceding section. The image processing procedure was incorporated using the FIJI open-source image-processing software environment. Several built-in filters were applied to the images to obtain thresholded images representing solid and porous structures. Details of the image-processing procedure can be found in the preceding section.

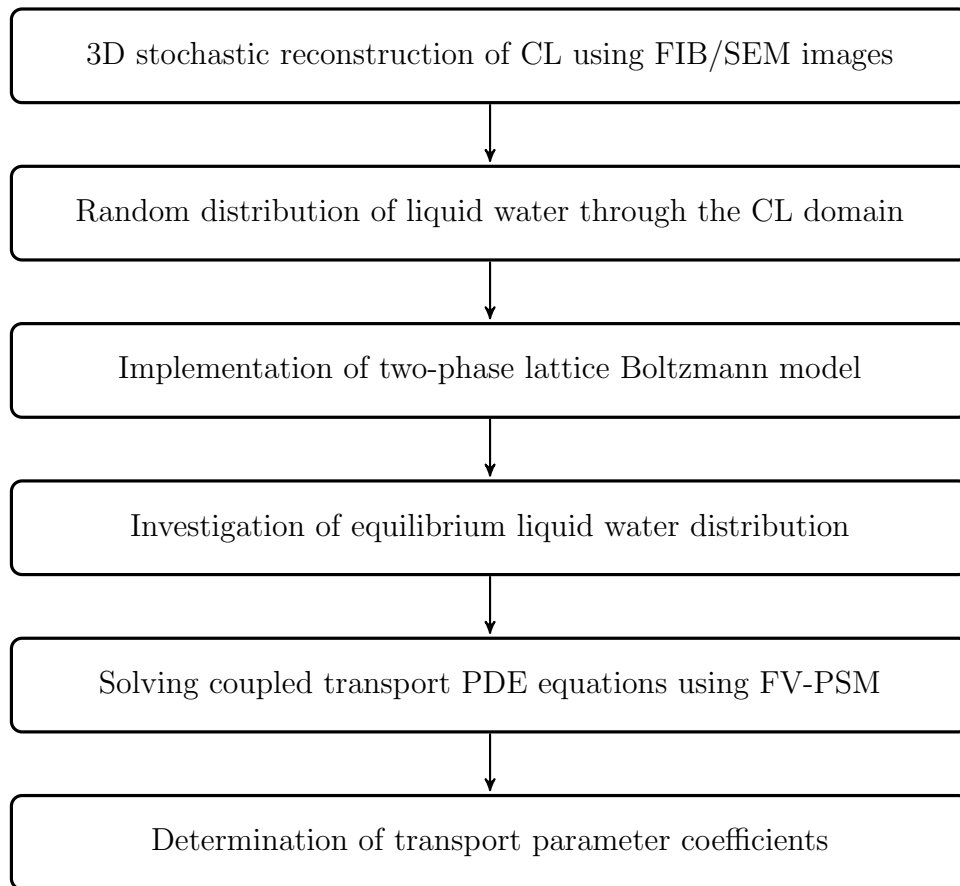


Figure 3.6: Flow chart outlining the methodology used in the present study

The resolved thresholded images are used to stochastically reconstruct a CL that consists of four phases: ionomer, carbon-black spheres, pores, and Pt particles. In

the reconstruction procedure, the Pt particles were assumed to be a non-volumetric phase located at the carbon-ionomer interfaces. To reconstruct the 3D nano-structure of the CL sample, we follow the simulated annealing technique described in Singh et al. [13] and in which two different cost functions were used. A cost function is a quantitative measure of the difference between the initial and target structures. One such frequently used cost function is the two-point-correlation function; lower-order statistical correlation functions indicate a mismatch between the targeted structure and the initial CL structure. The two cost functions used in [13] were: (1) the difference in pore pixels between the FIB/SEM experimental image and the corresponding numerically reconstructed image, and (2) the sum of squares of the differences in the two-point correlation function.

It has been shown that the latter cost function results in a statistically better, higher-fidelity representation of the CL [13]. Furthermore, the cost function according to the two-point correlation function has been demonstrated to be computationally more efficient than its counterpart. Hence, in this study, the two-point-correlation function, which is the more rigorous cost function, was used to generate the 3D CL nano-structure. The CL structure was optimized in each computational time step using simulated annealing.

The 3D numerically reconstructed CL included a $305 \times 235 \times 252$ grid with an isotropic resolution of 5.95 nm. Singh et al. [13] carried out several parametric studies using a FV-PSM to determine transport parameter coefficients through the reconstructed CL, but they ignored the impact of liquid water on these coefficients. In the present study, to investigate the impact of liquid water on transport properties, a coupling method consisting of a finite-volume pore-scale model (FV-PSM) and a two-phase free-energy LBM was used. The dynamics of liquid water through the reconstructed CL were solved for using a robust two-phase lattice Boltzmann technique.

The nano-structure of the reconstructed CL was made up of different materials with different degrees of hydrophobicity and hydrophilicity. Therefore, it is desirable to develop a method that can capture water dynamics, water preferential sites, and percolation pathways. The sophisticated mesoscopic LBM evolves the distribution of different fluid phases from an initial distribution towards an equilibrium distribution. The equilibrium distribution can ultimately be assumed to represent the preferred locations that water tends to occupy in the CL nano-structure. In this work, to obtain preferential water sites, the simulations were initiated by randomly distributing liquid

water through the 3D nano-structure of the reconstructed CL using a MATLAB random number generator. The two-phase LBM was then used to rearrange the water distribution towards the equilibrium state. In the next stage, the liquid water equilibrium was taken into account as a stationary heat-conducting, non-electric and non-proton conductive phase in conjunction with the other solid and gas phases of the CL. Finally, pore-scale simulations using a finite-volume method (FVM) were conducted to predict mass, charge, and heat transport through the CL, accounting for the presence of liquid water.

Figure 3.7 (a, b, and c) illustrate the numerical steps in acquiring a reconstructed CL for a single slide of an obtained experimental FIB/SEM image. The initial distribution of liquid water throughout the slide image is shown in Figure 3.7d.

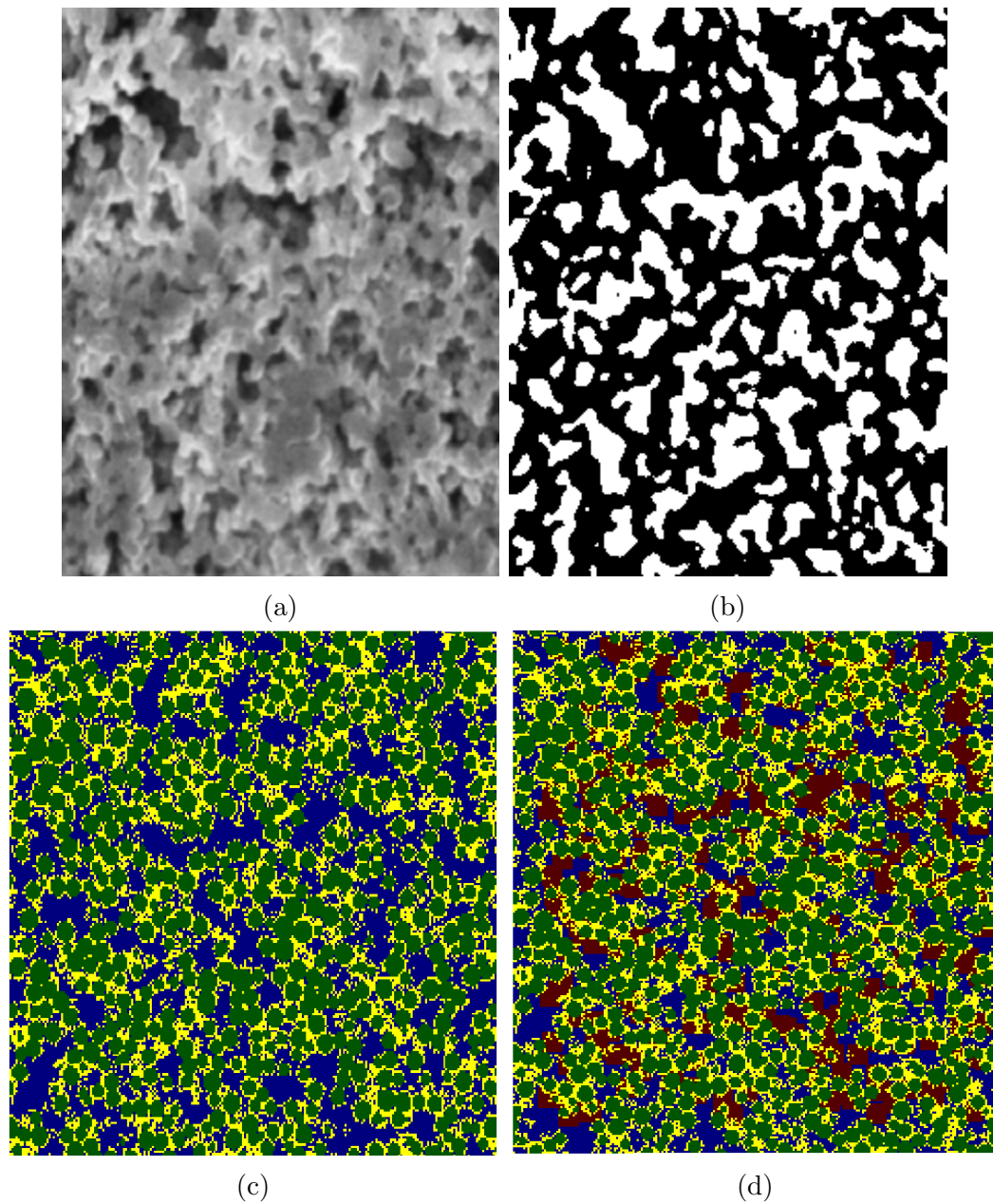


Figure 3.7: Steps to reconstruct the CL and to obtain the initial phase of liquid water distribution: a) cropped area of interest from FIB/SEM showing solid phase (light gray) and open pores (dark gray); b) binary image obtained after image processing and thresholding with solid phase (black) and pores (white); c) reconstructed with carbon particles (green), ionomer (yellow) and pores (blue); and d) computed liquid water distribution (red) in the CL.

Chapter 4

Methodology

4.1 Boltzmann Equation

The lattice Boltzmann method (LBM) is a discretized form of the Boltzmann equation expressed in Eq. (4.1), which is based on the kinetic theory of gases [88–91]:

$$\frac{Df(r, v, t)}{Dt} = Q_f(f) \quad (4.1)$$

where $Q_f(f)$ and f are the collision operator and the density distribution function respectively. The density distribution function f is a function of seven parameters (three spatial parameters x , y , and z ; three velocity components corresponding to each of the spatial directions v_x , v_y , and v_z ; and time t). Therefore, the material derivative of the density distribution can be described as:

$$\frac{Df}{Dt} = \frac{\partial f}{\partial t} + \frac{\partial f}{\partial x} \frac{dx}{dt} + \frac{\partial f}{\partial y} \frac{dy}{dt} + \frac{\partial f}{\partial z} \frac{dz}{dt} + \frac{\partial f}{\partial v_x} \frac{dv_x}{dt} + \frac{\partial f}{\partial v_y} \frac{dv_y}{dt} + \frac{\partial f}{\partial v_z} \frac{dv_z}{dt} \quad (4.2)$$

Or

$$\frac{Df}{Dt} = \frac{\partial f}{\partial t} + v_x \frac{\partial f}{\partial x} + v_y \frac{\partial f}{\partial y} + v_z \frac{\partial f}{\partial z} + a_x \frac{\partial f}{\partial v_x} + a_y \frac{\partial f}{\partial v_y} + a_z \frac{\partial f}{\partial v_z} \quad (4.3)$$

where v_x , v_y , and v_z are local velocity components and a_x , a_y , and a_z are local acceleration components. Substitution Eq. (4.3) into Eq. (4.1) gives rise to the following partial differential form of the Boltzmann equation [88–91]:

$$\frac{\partial f}{\partial t} + (v \cdot \nabla) f = Q_f(f) + F_{ext} \quad (4.4)$$

$$F_{ext} = -\frac{F}{m} \cdot \nabla_v f \quad (4.5)$$

where F is body force. The density distribution function f in the above mentioned equations is a combination of equilibrium and non-equilibrium density distribution functions and can be written as [88–91]:

$$f = f^{eq} + f^{neq} \quad (4.6)$$

where f^{eq} and f^{neq} are equilibrium and non-equilibrium distribution functions. The non-equilibrium part of distribution function f^{neq} can be described as small perturbation from equilibrium state. The non-equilibrium distribution function is approximated by the first level of Chapman Enskog expansion of the distribution function. The equilibrium distribution function f^{eq} is defined based on the Maxwell-Boltzmann equation described in Eq. (4.7). The function depends on the macroscopic properties of the fluid flow such as density, velocity, and temperature [88–91].

$$f^{eq} = \frac{\rho}{(2\pi RT)^{\frac{D}{2}}} e^{[-\frac{(v-V)(v-V)}{2RT}]} \quad (4.7)$$

where ρ , T , and R are density, temperature, and gas constant. In the above equation, D is equal to 3 which corresponds to the degrees of freedom in a monoatomic gas. According to the conservation of mass and momentum, the density and momentum are collision invariant. In the BGK formulation a simple collision operator models the collision as a relaxation of the density distribution function toward the Maxwellian equilibrium distribution function. Therefore, the equilibrium density distribution function should have mass and momentum related moments in common with the density distribution function as [88–91]:

$$\rho = \int f(r, v, t) dv = \int f^{eq}(r, v, t) dv \quad (4.8)$$

$$\rho V = \int f(r, v, t) v dv = \int f^{eq}(r, v, t) v dv \quad (4.9)$$

The collision term in Eq. (4.4) can be described using the BGK approximation [88–91]:

$$Q_f(f) = -\frac{f - f^{eq}}{\tau_\nu} \quad (4.10)$$

where τ_ν is the relaxation time of the density distribution function towards the equilibrium density distribution function. From Eq. 4.6 with the assumption of $\text{Kn} \ll 1$, one can rewrite this equation to clarify the role of non-equilibrium distribution function as:

$$Q_f(f) = -\frac{f^{neq}}{\tau_\nu} \quad (4.11)$$

Substitution of Eq. (4.10) into Eq. (4.4) gives:

$$\frac{\partial f}{\partial t} + (v \cdot \nabla) f = -\frac{f - f^{eq}}{\tau_\nu} + F_{ext} \quad (4.12)$$

Eq. (4.12) is the BGK kinetic model. This equation relates the microscopic properties of a fluid flow system to its macroscopic properties. From Eq. (4.12), the conservation laws (mass, momentum, and energy) can be recovered [88–91].

4.2 Lattice Boltzmann Equation

The discretization of the Boltzmann equation Eq. (4.12) gives rise to the single-phase lattice Boltzmann equation expressed in Eq. (4.13) [88–91]:

$$f_i(r + e_i \delta t, t + \delta t) = f_i(r, t) + Q_f(f) \quad i = 0, 1, 2, \dots, m \quad (4.13)$$

where m determines the standard number of system directions in the framework of LBM ($m=8$ for 2D and $m=18$ for 3D) and e_i is the velocity of each density distribution in each direction. It should be noted that although the Boltzmann equation (Eq. (4.1)) describes interactions in gas flows, the general form of the Boltzmann Eq. (4.14) multi-body collision operators making it applicable to dense fluids by using, e.g., the multiple-relaxation scheme describe later. Substituting the BGK collision term into the above equation results in the standard form of the LBM equation [88–91]:

$$f_i(r + e_i \delta t, t + \delta t) = f_i(r, t) - \frac{f_i(r, t) - f_i^{eq}(r, t)}{\tau_\nu} + F \quad (4.14)$$

The macroscopic properties can be obtained according to the following relations [88–91]:

$$\rho = \sum_i f_i \quad (4.15)$$

$$\rho u = \sum_i f_i e_i \quad (4.16)$$

A 3D network of LBM (D3Q9) is shown in 4.1.

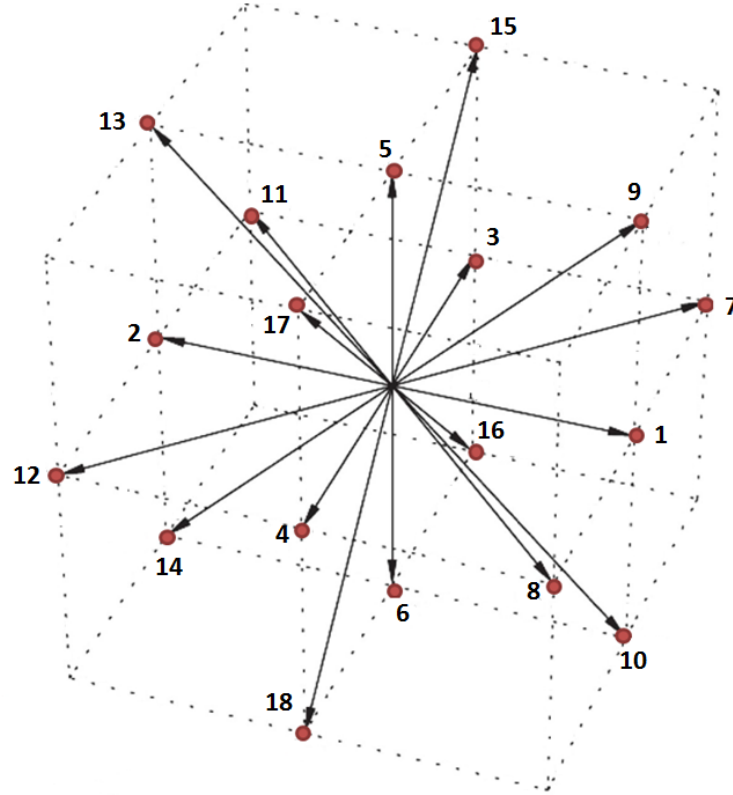


Figure 4.1: 3D network of LBM

The Taylor series expansion of Eq. (4.7) results in the equilibrium density distribution in the framework of LBM defined by Eq. (4.14) [88–91]:

$$\begin{aligned}
 f_i^{eq} &= \frac{4}{9}\rho\left[1 - \frac{3}{2}\frac{u^2}{c^2}\right] & i = 0 \\
 f_i^{eq} &= \frac{1}{9}\left[1 + 3\frac{e_i \cdot u}{c^2} + \frac{9}{2}\frac{(e_i \cdot u)^2}{c^4} - \frac{3}{2}\frac{u^2}{c^2}\right] & i = 1, 3, 5, 7 \\
 f_i^{eq} &= \frac{1}{36}\left[1 + 3\frac{e_i \cdot u}{c^2} + \frac{9}{2}\frac{(e_i \cdot u)^2}{c^4} - \frac{3}{2}\frac{u^2}{c^2}\right] & i = 2, 4, 6, 8
 \end{aligned} \quad (4.17)$$

where c is the velocity of lattice space which is equal to unity for a unity lattice space

and a unity time space. The lattice Boltzmann method consists of two main parts: collision and streaming. The two terms on the right-hand side of Eq. (4.14) represent the process that simulates the collision of particles in the system. The term on the left-hand side of Eq. (4.14) corresponds to the streaming process that captures the propagation of particles to their neighbourhood after colliding.

4.3 Boundary Conditions

For fluid flow problems, Eq. (4.14) should be solved in addition to the appropriate boundary conditions specific to the problem. Two of the best-known and most frequently used boundary conditions in LBM simulations are bounce-back and periodic boundary conditions.

4.3.1 Periodic Boundary Condition

The periodic boundary condition is the simplest form of boundary condition in computational fluid dynamics. In the lattice Boltzmann method, this boundary condition can be implemented using density distribution functions rather than macroscopic properties such as velocity and pressure. The concept of periodic boundary condition in the LBM is that distribution functions that enter/leave by one boundary leave/enter from the opposite boundary in the same direction. A schematic of this periodic boundary condition is shown in Fig. 4.2.

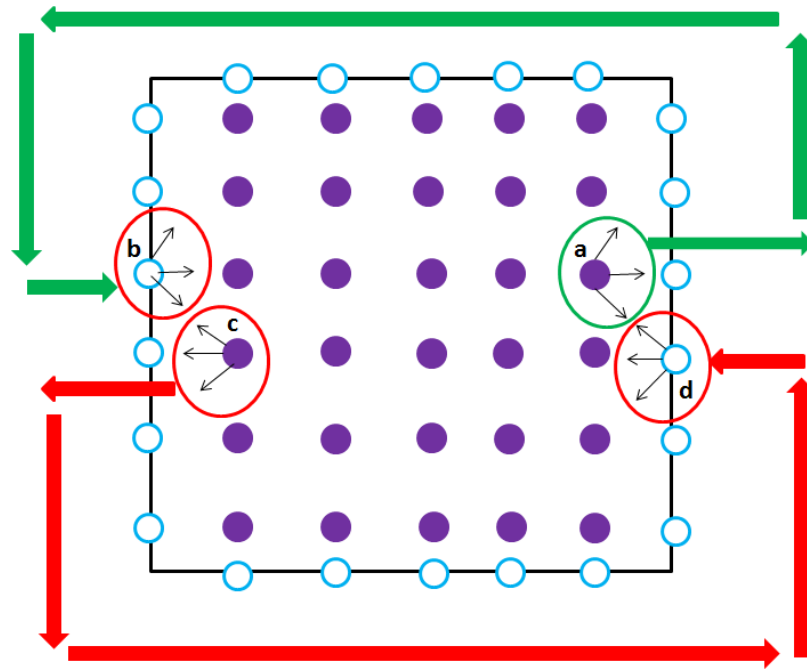


Figure 4.2: Schematic of periodic boundary condition

4.3.2 Bounce-Back Boundary Condition

The bounce-back boundary condition in the LBM is a descriptor of no-slip boundary conditions in computational fluid dynamics. This boundary condition enforces zero fluid velocity at solid walls and applies to continuum flow ($Kn \ll 1$) conditions. In the LBM framework, the interaction between the fluid and solid phases is dealt with using the bounce-back boundary condition. In the bounce-back technique shown in Fig. 4.3, distribution functions that are travelling from fluid nodes toward the wall or from solid nodes, after hitting the wall, are reflected back 180 degrees towards fluid nodes.

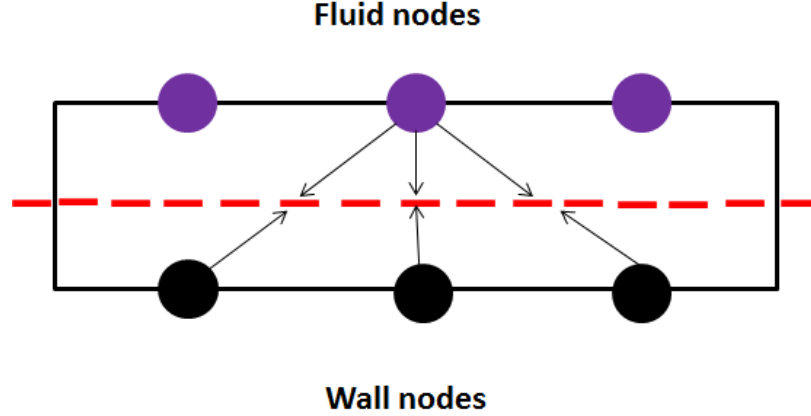


Figure 4.3: Schematic of bounce-back boundary condition

4.4 MRT-LBM

In this section, the methodology of two-phase free-energy LB is presented. To capture the total energy of a three-phase system including two fluids (gas and water) and a solid phase, a free-energy functional which provides the principal information about the thermodynamic properties of the three-phase system is used [66]:

$$F = \int dV \left(\psi + \frac{\kappa}{2} |\Delta \phi|^2 \right) + \int dS \psi_s \quad (4.18)$$

The first term in the first integral on the right-hand side of Eq. (4.18) describes the standard Ginzburg-Landau expression defined in Eq. (4.19), and the second term reflects intermolecular interactions, which can be assumed to be repulsive forces at the interface of two fluids [66]. The total surface energy density between fluid and solid phases is taken into account by the term in the second integral given in Eq. (4.20) [92, 93]:

$$\psi = A(\phi^2 - 1)^2 \quad (4.19)$$

$$\psi_s = -\gamma \phi_s \quad (4.20)$$

where the order parameter ϕ is a variable that distinguishes the two fluid phases in terms of the density difference and is calculated based on Eq. (4.28). The double-well free energy-density shown in Eq. (4.19) has two equilibrium minimum order

parameters $\phi = \pm 1$ which correspond to high- and low-density fields in the bulk of the two fluids. Parameters k and A used in Eqs. (4.18) and (4.19) can explicitly be determined from the surface tension and interface width respectively as [66]:

$$\sigma = 4 \frac{\sqrt{2kA}}{3} \quad (4.21)$$

$$\xi = \sqrt{\frac{2k}{A}} \quad (4.22)$$

In Eq. (4.20), γ is a parameter controlling the wetting potential, which can be derived according to the wetting property of a solid surfaces characterized by a static contact angle, shown in Eq. (4.23) [66] .

$$\gamma = 2 \text{sign}\left(\frac{\pi}{2} - \theta\right) \sqrt{\cos \frac{\beta}{3} (1 - \cos \frac{\beta}{3})} \sqrt{2Ak} \quad (4.23)$$

where θ is static contact angle and $\beta = \arccos(\sin^2 \theta)$. Having obtained the wetting potential, the following boundary condition can be implemented on solid surfaces [66]:

$$\left(\frac{\partial \phi}{\partial n}\right)_s = n \cdot \Delta \phi = -\frac{\gamma}{k} \quad (4.24)$$

where n is a vector normal to solid surfaces. To simulate the dynamics of two-phase flow in the framework of a multi-relaxation-time lattice Boltzmann (MRT-LBM) method, two sets of density distribution functions are used to describe the macroscopic properties of each species and to distinguish the location of each phase and track the evolution of their interface [66, 78]:

$$f(r + e_i \delta t, t + \delta t) = f(r, t) - Q^{-1} \Lambda_f (m_f(r, t) - m_f^{eq}(r, t)) + \delta t \left(I - \frac{1}{2} Q^{-1} \Lambda_f Q\right) G(r, t) \quad (4.25)$$

$$g(r + e_i \delta t, t + \delta t) = g(r, t) - Q^{-1} \Lambda_g (m_g(r, t) - m_g^{eq}(r, t)) \quad (4.26)$$

where f and g are density and order parameter distribution functions respectively, Λ_f and Λ_g describe diagonal relaxation matrices of each distribution function as given in [66], and Q represents a transformation matrix that linearly converts the distribution functions f and g into the moment spaces (m_f and m_g) [66]. The m_f and m_g are moment vectors of velocity and order parameter distribution functions respectively.

In this model, the local density ρ , the order parameter ϕ and the momentum j are respectively calculated using [66]:

$$\rho = \sum_i f_i \quad (4.27)$$

$$\phi = \sum_i g_i \quad (4.28)$$

$$j = \rho u = \sum_i f_i e_i + \frac{\delta}{2} G \quad (4.29)$$

In Eqs. 4.25 and 4.29 G takes into account the effect of the body forces given by [66]:

$$G_i = w_i \frac{(e_i - u)}{c_s^2} \cdot (F_b + \mu_c \nabla \phi) \quad (4.30)$$

4.5 FVM-PSM

The first phase of the present work is focused on simulating the liquid water transport dynamics using the two-phase LBM described in the previous section. Once that is accomplished, the impact of liquid water on the effective transport properties needs to be determined. This is accomplished by coupling the LBM to a pore-scale model (PSM) that solves the coupled governing equations for the electron and proton conductivities and for species and energy conservation. The PSM uses a finite-volume method is used to discretize the governing equations. The method was developed at the ESTP laboratory by Lange et al [94, 95] and is extended in this work to include the additional liquid phase. The governing equations consist of diffusive and reactive transport terms, which can be expressed for O_2 , H_2O , electron, proton and energy respectively via [13]:

$$\nabla \cdot (J_{O_2}^d - r_{ORR}/(4F_f)) = 0 \quad (4.31)$$

$$\nabla \cdot (J_{H_2O}^d - r_{ORR}/(2F_f) - n_d \sigma_m \nabla \phi_m / F_f) = 0 \quad (4.32)$$

$$\nabla \cdot (\sigma_s \nabla \phi_s - r_{ORR}) = 0 \quad (4.33)$$

$$\nabla \cdot (\sigma_m \nabla \phi_m - r_{ORR}) = 0 \quad (4.34)$$

$$\nabla \cdot (-k_i \nabla T) = S_{irr} + S_{rev} \quad (4.35)$$

where $J_{O_2}^d, J_{H_2O}^d$ are respectively the diffusive fluxes for O_2 and H_2O in the gas phase that are solved in the pores using the Maxwell-Stefan equation, which accounts for the bulk and Knudsen diffusions. To compute Knudsen diffusion, which depends upon the pore diameter, the Derjaguin correction for the Knudsen diffusion is used.

The local pore diameter in each pore cell is determined from the average of 13 scalar lengths of a pore cubic pocket (along x , y , and z (3); two diagonal directions in each of the x - y , x - z , and y - z planes (6); and four of the diagonal directions obtained by the set of lines $|x| = |y| = |z|$ in 3D space (4)) [13].

In the Eqs. (4.31) to (4.35), the r_{ORR} parameter represents the electrochemical reaction rate (Cm^{-2}) governed by the Tafel equation at the carbon-ionomer interface consisting of Pt particles (non-volumetric phase) and defined in Eq. (4.36) [13]. Liquid water in CLs is generated in the high current densities which correspond to the high overpotential operation. Under high overpotential conditions, the Butler Volmer equation can simplify to the Tafel equation.

$$r_{ORR} = -1_{Pt} [i_0 \exp(-\frac{\alpha F_f}{RT} \eta)], \quad (4.36)$$

where, 1_{Pt} equals 1 at the Pt-containing C-ionomer interface; i_0 , α , F_f and η are the exchange current density, charge transfer coefficient, Faraday constant and overpotential, respectively. The overpotential is linked to the ionic potential, φ_m , and the electronic potential, φ_s , as $\eta = \varphi_s - \varphi_m$. The expression of the exchange current density can be found in [18]. In Eq. (4.35), the irreversible losses caused by ohmic losses, S_{irr} , and the reversible losses associated with the electrochemical reaction, S_{rev} , are defined as [13]:

$$S_{irr} = \sigma_s (\nabla \varphi_s)^2 + \sigma_m (\nabla \varphi_m)^2 \quad (4.37)$$

$$S_{rev} = (\eta + \Pi) \nabla \cdot r_{ORR}, \quad (4.38)$$

where, σ_s, σ_m, k_i and Π are the electronic conductivity, ionic conductivity, thermal conductivity and the Peltier coefficient, respectively [13]. In the Eq. (4.32), n_d is the electro-osmotic drag coefficient of water and is set to 1.

The diffusion of O_2 and H_2O species through the ionomer phase is taken into

account as the Fickian diffusion in a dilute solution, whereas no diffusion through carbon is assumed [13]:

$$J_{O_2}^d = -D_{O_2,m} \nabla c_{O_2} \quad (4.39)$$

$$J_{H_2O}^d = -D_{H_2O,m} \nabla c_{H_2O}, \quad (4.40)$$

where $D_{i,m}$ is the expression for the diffusivity of species, oxygen, and water vapour through the membrane [13].

To solve the coupled transport equations, the Dirichlet boundary conditions are considered for the x, y and z directions one at a time, whereas the rest of the directions in each case were set to be periodic. The values for the boundary conditions were taken from [13], details of this method can be found in Djilali and co-workers [13, 14, 81, 82].

Chapter 5

Evaluation, Analysis, and Comparisons

In this section, the parameters are specified in LBM units. The relation between the parameters in LBM units and physical parameters used in the simulations is documented in Appendix A.

5.1 Validation of Numerical Code

A computer code developed by Toyota *R&D* lab [66] and incorporating the multiple relaxation time LBM described in the preceding Chapter was modified and used for this work. Prior to using the method to investigate flow in the CL, this Section presents validation results for 4 simpler problems focusing on underlying physics related to the CL and for which experimental data is available.

5.1.1 Permeability of a Packed Bed

To validate the numerical method, a series of benchmark test cases were used. The first case involved a packed-bed porous medium consisting of a cubic array of spheres. The non-dimensional absolute permeability was compared based on an analytical solution proposed by Zick and Homsey [96], the semi-empirical Kozney-Carman (KC) equation, and the LBM method. The absolute permeability k for a single incompressible fluid in a laminar regime can be expressed based on Darcys law:

$$u = -\frac{k}{\mu} \nabla p \quad (5.1)$$

where u is the superficial velocity of a fluid in the domain defined as the flow rate divided by the cross sectional area of the porous medium, ∇p is the pressure gradient across the porous medium, and μ is the dynamic viscosity of the fluid. The absolute permeability of a porous domain is a function of the porous structure of the material only, not of the fluid. In this regard, the absolute permeability k can also be described in terms of the porosity ϕ based on the semi-empirical Kozney-Carman (KC) relation:

$$k = C \frac{\phi^3}{(1 - \phi)^2} \quad (5.2)$$

where the Kozney-Carman constant C is a function of the sphere diameter, i.e. $C = \frac{d^2}{180}$. As illustrated in Fig. 5.1, the LBM results are in a good agreement with the analytical solution over the entire range of properties, whereas the KC results become, as expected, less accurate at high porosity because they were determined based on experiments for packed low-porosity sphere beds.

The absolute permeability depends only on the porous medium structure, not on the fluid. A comparison of the absolute permeability predicted by MRT-LBM and SRT-LBM for different values of kinematic viscosity is shown in Fig.5.2. The absolute permeability remains constant for MRT-LBM, whereas it varies quasi-linearly for SRT-LBM. This unphysical behaviour is a well-documented issue with the BGK-LBM model, making this formulation problematic for multi-phase flow systems having different viscosities. This deficiency by the SRT-LBM model can be resolved by using a MRT-LBM approach. The MRT-LBM separates the relaxation times for different kinetic modes, and consequently the collision operator can be constructed to be essentially viscosity independent.

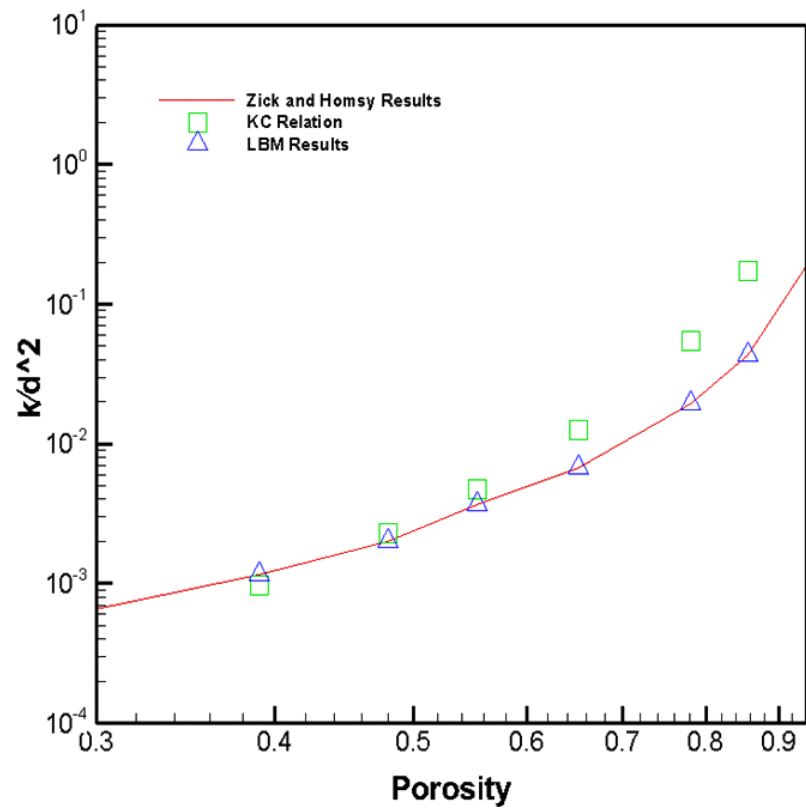


Figure 5.1: Comparison of simulation results for dimensionless permeability obtained by LBM with the analytical solution and the KC relation for a packed-sphere porous medium.

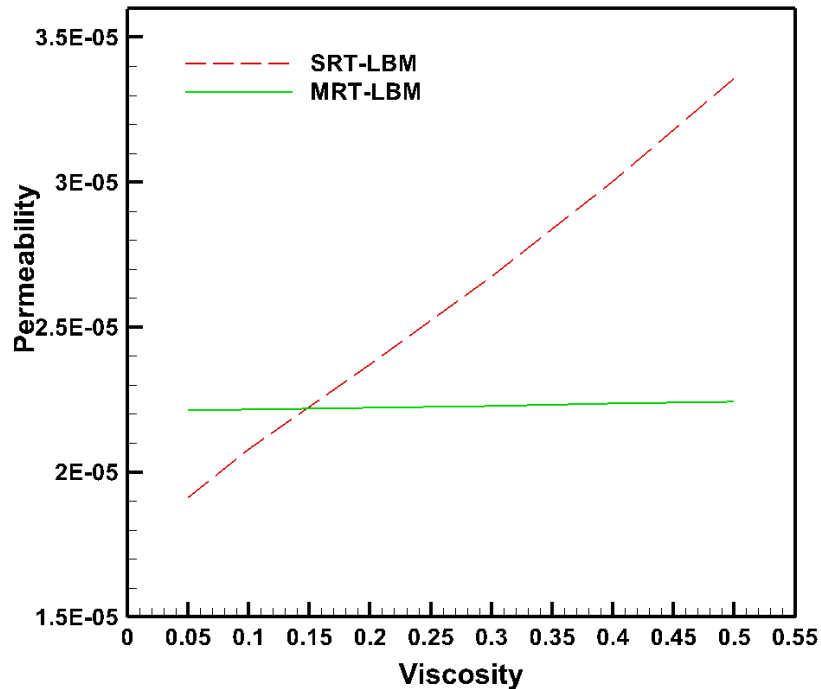


Figure 5.2: Absolute permeability versus fluid viscosity based on MRT-LBM and SRT-LBM.

5.1.2 Laplace Law

To verify the physical representation of surface tension, the predicted pressure difference across the interface of a static bubble was examined as the next test case. Initially, a spherical water droplet surrounded by air was located at the centre of a cubic domain. A periodic boundary condition was used at all boundaries. The density ratio of the two fluids was selected as 1000. Based on the Laplace law for a spherical stationary droplet, the pressure difference across the interface is:

$$\Delta p = \frac{\sigma}{R} \quad (5.3)$$

where Δp is the pressure jump across the interface and R is the radius of the droplet. The pressure at each fluid medium is calculated as an average value when the system reaches equilibrium. Figure 5.3 illustrates the good agreement obtained between numerical and analytical results.

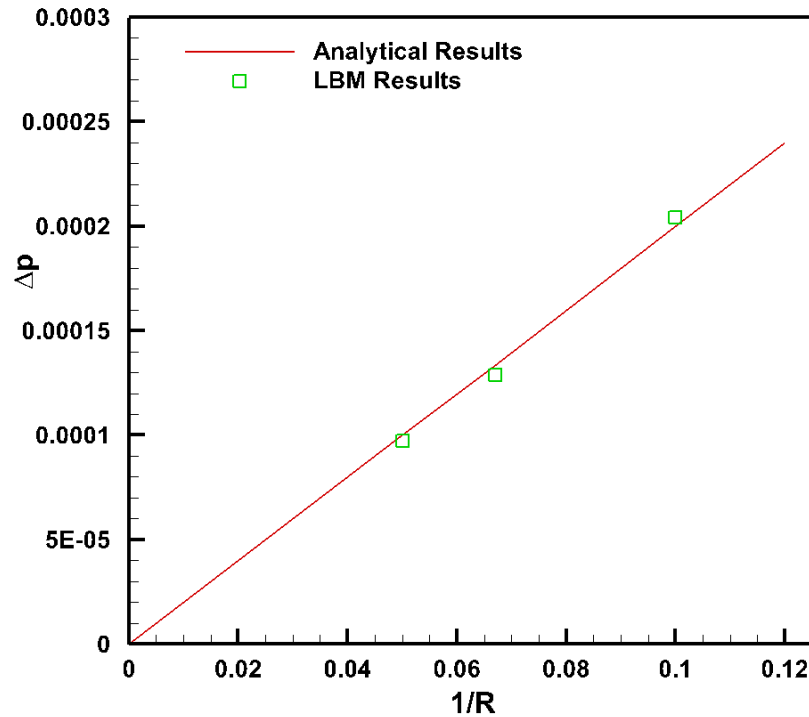


Figure 5.3: Comparison of simulation results for the pressure jump across the interface with the analytical solution based on the Laplace law.

5.1.3 Wettability Potential of Solid Surfaces

The third test case examines whether a hemispherical water droplet goes to its correct equilibrium state. A droplet of radius $R=10$ is located on a surface with varying wettability potential, as indicated in Fig. 5.4. The wettability of solid surfaces in the 3 cases illustrated in Fig. 5.4 is calculated based on Eq. 4.23 with the corresponding contact angles. The obtained surface wettability corresponding to each case is applied to surface wetting boundary condition through Eq. 4.24. The computational domain consists of a $51 \times 51 \times 51$ cubic lattice. The bounce-back boundary condition is used for the upper and lower walls, and a periodic boundary condition is used for the other pair-wise directions. Increasing the wettability potential of the solid surface from hydrophilic to hydrophobic causes water to be repelled from the solid surface, as qualitatively illustrated in Figs. 5.4 and 5.5. These figures show a comparison of the measured contact angles with theoretical values for different solid-surface wettability potentials. The capability of the method to capture multi-phase flows with different wettability potentials is a particularly important feature for application to fuel-cell catalyst layers.

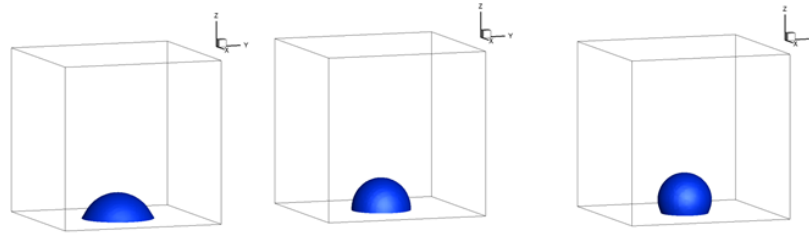


Figure 5.4: Simulation of equilibrium contact angle of a hemispherical liquid droplet on a surface: a) $\theta = 60^\circ$ b) $\theta = 90^\circ$ c) $\theta = 120^\circ$.

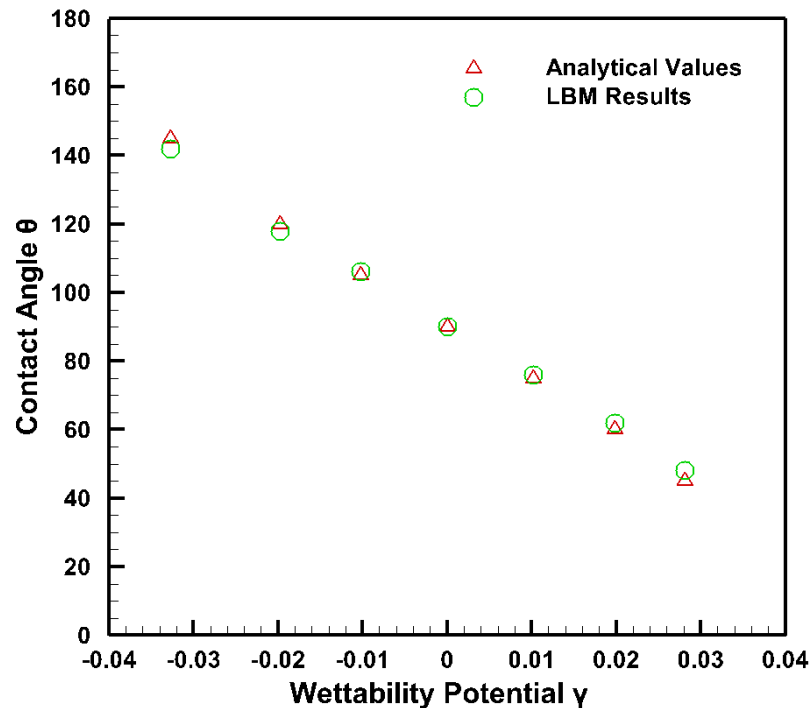


Figure 5.5: Comparison of simulation results for the measured contact angles with theoretical values.

5.1.4 Capillary Pumping in a Nano-Channel

As the characteristic size of a channel or pore becomes smaller, the surface area-to-volume ratio increases, and surface tension and contact angle play an increasingly important role. To simulate the effect of different contact angles on water transport, a water slug in a square-section nano-channel otherwise filled with air was considered. The left half of the channel had a hydrophobic surface and the other half a hydrophilic surface, as shown schematically in Fig.5.6a. According to the Young-Laplace equation, the capillary pressure between non-wetting and wetting fluids is:

$$P_c = P_l - P_g = -\frac{2\sigma\cos(\theta)}{r} \quad (5.4)$$

where P_l and P_g are the liquid and gas average pressures respectively, σ is the surface tension and r the hydraulic radius of the channel. In the hydrophilic portion, the liquid water wets the surface, and the interface is concave with a negative capillary pressure, and conversely in the hydrophobic region, the interface is convex, and the capillary pressure is positive. The pressure difference between the two interfaces induces capillary pumping, as illustrated in Fig. 5.6. As the left interface transitions from the hydrophobic to the hydrophilic region, its curvature adjusts. The capillary pressures eventually become equal, and the motion of the slug stops. The mechanism illustrated here can play an important role in water transport through catalyst-layer pores with inhomogeneous surface wetting.

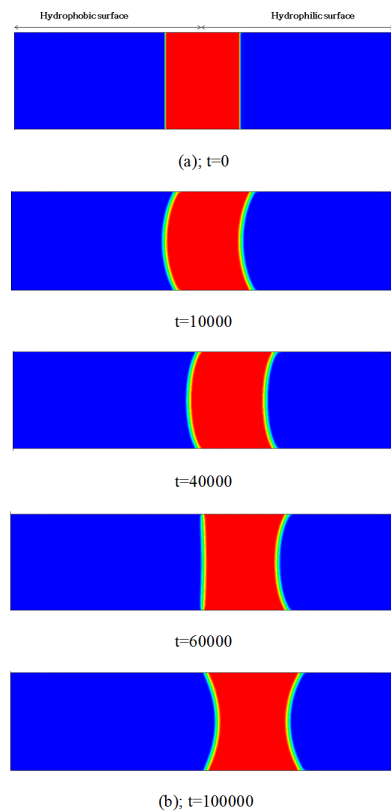


Figure 5.6: a) Schematic of initial distribution of different fluids in a nano-channel assuming different contact angles b) capillary effect in a nano-channel.

5.2 Water Transport in a Reconstructed Catalyst Layer

We consider two-phase transport in the FIB/SEM reconstructed $1815 \times 1400 \times 1500 \text{ nm}^3$ catalyst-layer sample discussed in Section 3.1.3. The reconstruction was based on experimental data acquired using a FIB/SEM image stack, as described in [13,14]. Because current microscopic methods cannot discriminate between ionomer and carbon phases, these are combined in a single solid phase for the current simulations. This does not affect water transport as long as the wettability potential is correctly represented. Due to high computing costs, the computational domain was restricted to a subset of the reconstructed physical domain, with a size of $50 \times 50 \times 100$ LB units with a resolution of 15 nm per LB unit, as shown in Fig. 5.7. The resolution of 15 nm per LB unit is obtained based on the conversion of FIB/SEM physical unit into the corresponding computational domain in the framework of LBM. To simulate water intrusion into the CL, a water reservoir 10 LB thick was placed next to the domain inlet. The CL domain was initially fully saturated with air. A pressure gradient was imposed to drive water into the domain. The water-transport process was tracked until it reached an equilibrium state after 100,000 time steps. The equilibrium state is defined as the state when no changes can be observed in the saturation of penetrated liquid water into the domain and the system reaches a steady state condition. Simulations and analysis of the dynamic water patterns were conducted for a range of contact angles. In the following simulations, the values of the selected parameters are $\rho_l=1000 \text{ kg/m}^3$, $\rho_g=1.14 \text{ kg/m}^3$, $\sigma=.0786 \text{ N/m}$, $\zeta=67 \text{ nm}$. The non-dimensionalization of the variables and parameters used in the simulations is documented in the Nomenclature and Appendix. Periodic boundary conditions as well as the order parameter were taken into account for all sides of the velocity field, except for inlet and outlet order parameter boundary conditions on one side, where the inlet order parameter was chosen to be unity and the outlet one to be a zero gradient.

In addition to the effect of contact angle, the effects of varying pressure gradient, surface tension, and viscosity ratio on water-transport patterns and water saturation in the catalyst layer were also investigated. For the first case examined, the pressure difference across the domain and the dynamic viscosity ratio were set to $\delta p=0.0017$ ($\equiv 113.3 \text{ KPa}$), $M=\frac{\mu_{nw}}{\mu_w}=54$ respectively; this viscosity ratio corresponds to STP conditions [97]. It should be noted that both compressibility and rarefaction effects are neglected for the gas phase, because the flow velocities are small and the shear

stresses associated with the gas flow are much smaller than those for the liquid phase. The equilibrium water distributions are illustrated in Fig. 5.8 for various surface wetting conditions. The left-hand side depicts all three phases (water, air, and solid) and the right-hand side the corresponding water iso-surfaces. The contact angle and wettability potential have a strong impact on water-transport patterns, which evolve from stable displacement at $\theta = 105^\circ$, to pure capillary fingering at $\theta = 140^\circ$, with a transition to mixed patterns for intermediate contact angle $> \theta = 110^\circ$. Decreasing the wettability potential and contact angle below the transition value $\theta = 110^\circ$ results in higher saturation levels and translates in increased flooding risk in an operating fuel cell. Increasing the wettability potential of the solid phase significantly reduces water transport in the domain. Figure 5.8 also shows that maximum intrusion occurs in conjunction with two large pores located on the left side of the domain, whereas smaller pores with smaller menisci promote water transport through enhanced capillary diffusion. This is consistent with experimental observations of water transport in hydrophobic gas diffusion layers [26] and in conjunction with small cracks on CL and MPL that play a significant role in transferring water towards the GDL [30, 31, 34]. In the capillary fingering regime, the injected fluid preferentially percolates through the pores with the smallest capillary resistance (i.e., larger radius in a hydrophobic medium).

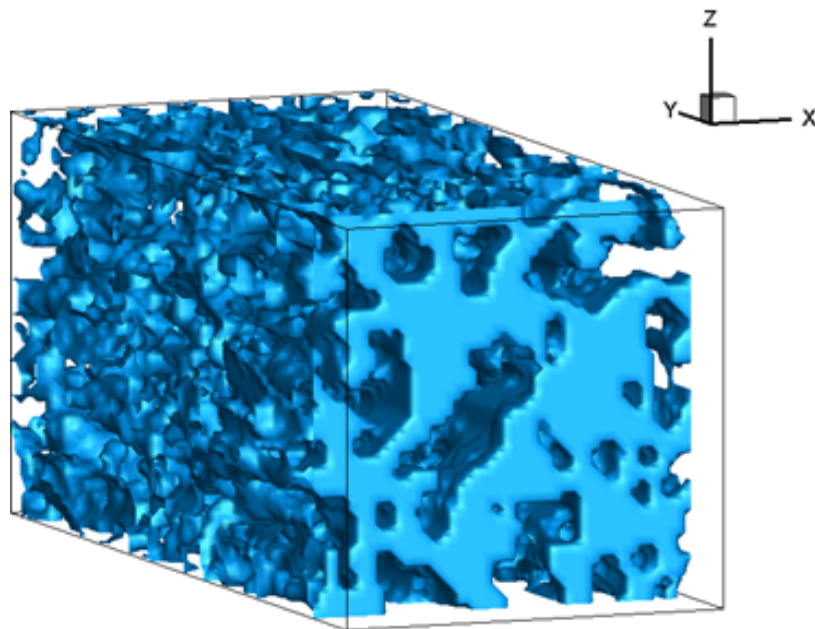
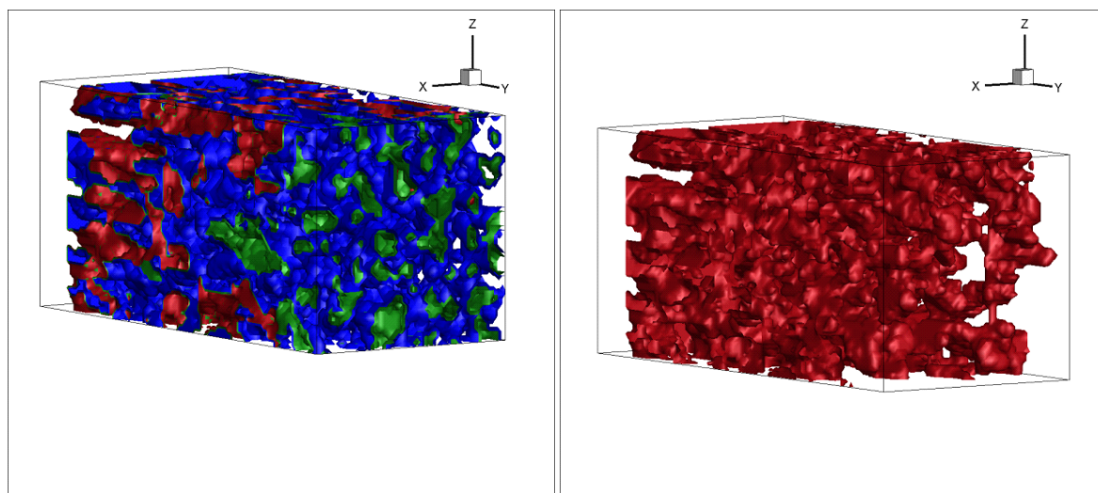
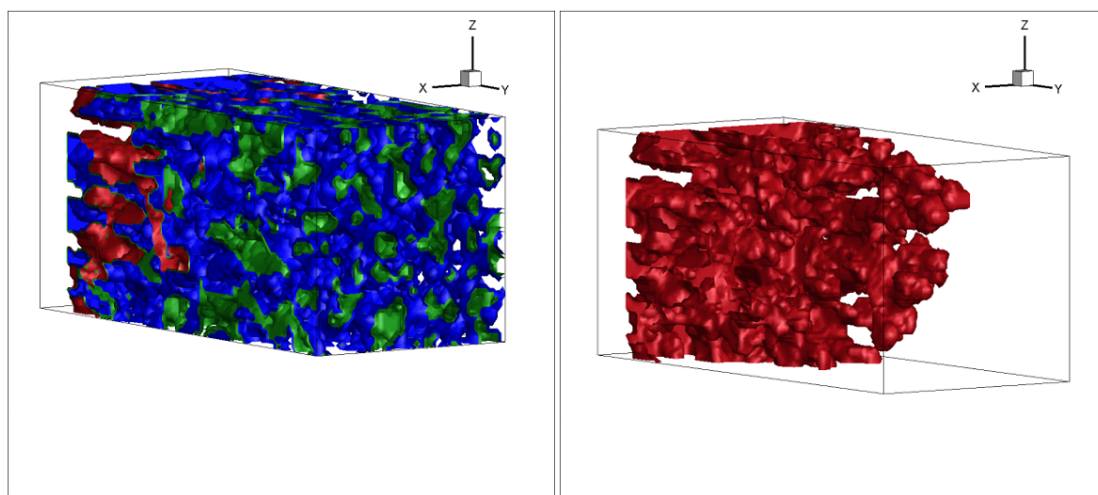


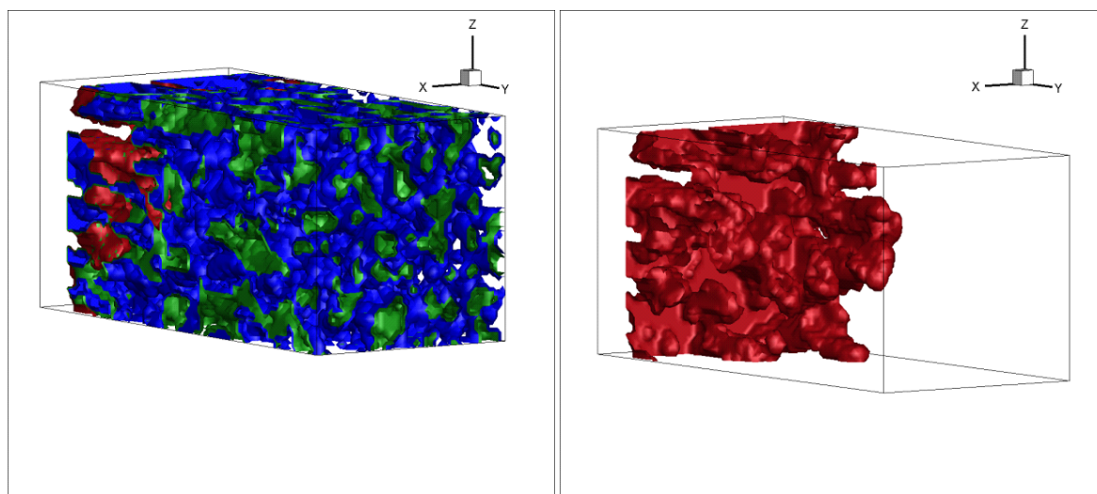
Figure 5.7: Schematic of reconstructed catalyst layers.



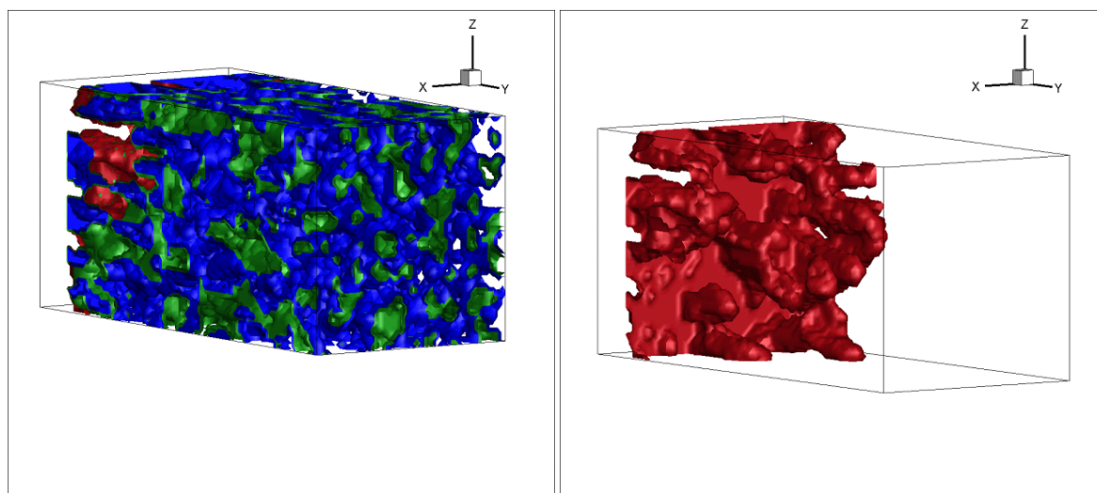
(a)



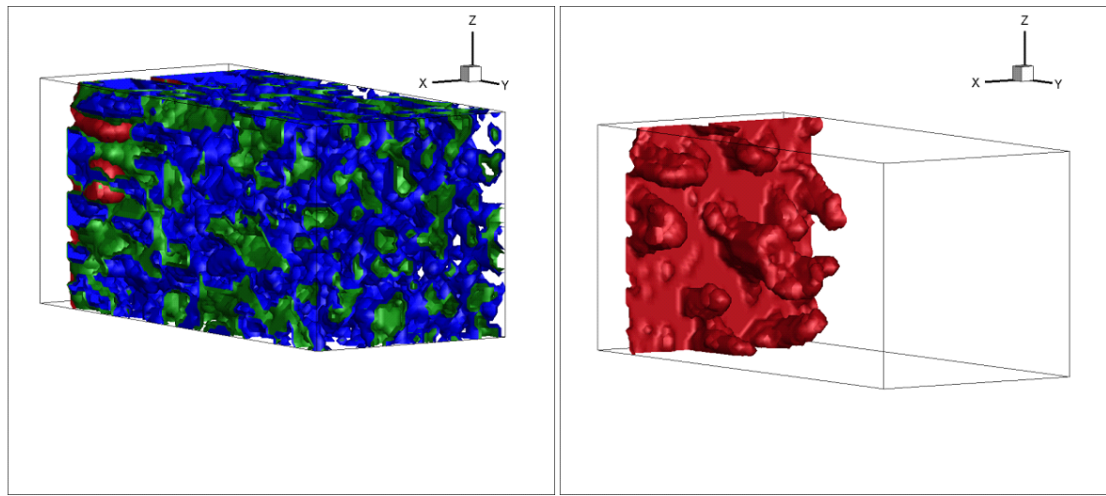
(b)



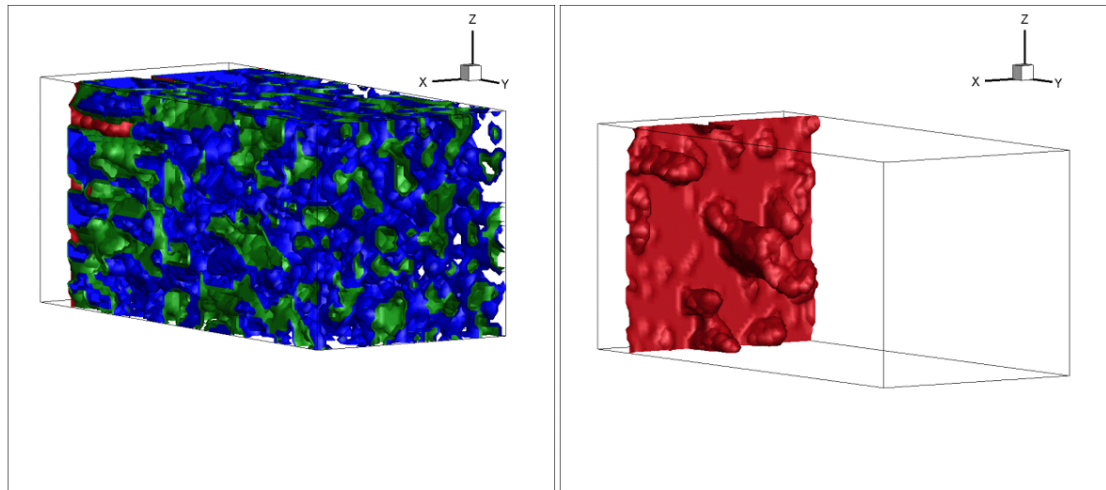
©



(d)



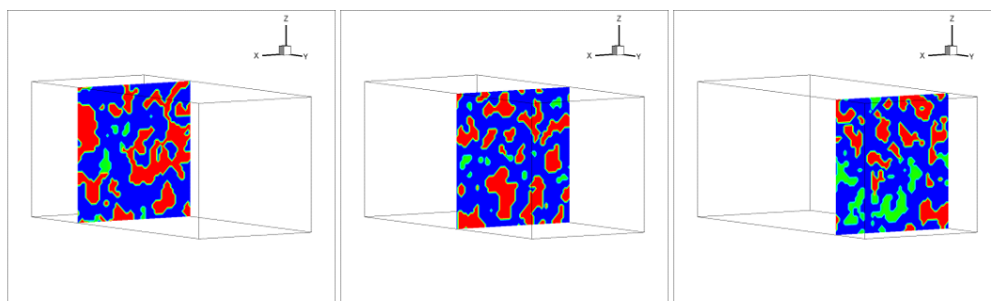
(e)



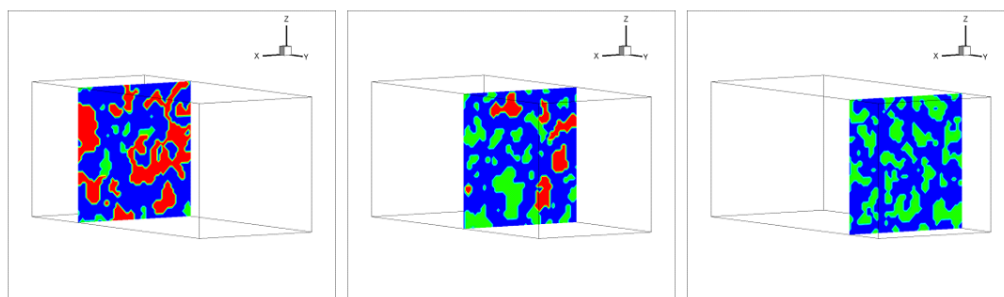
(f)

Figure 5.8: Visualization of water transport after $2.3 \mu\text{s}$ in reconstructed catalyst layers with $\delta p = 0.0017$ ($=113.3 \text{ KPa}$), $M=54$, and different contact angles: a) $\theta = 105^\circ$ b) $\theta = 110^\circ$ c) $\theta = 115^\circ$ d) $\theta = 120^\circ$ e) $\theta = 130^\circ$ f) $\theta = 140^\circ$. Left column (red: water, green: air, blue: solid structure); right column is the isosurface of water.

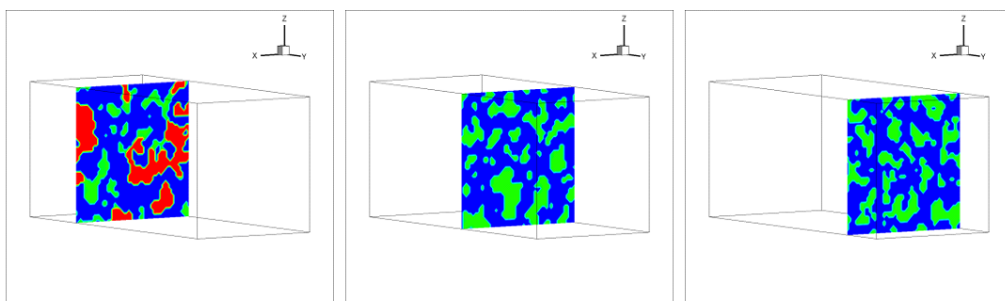
To analyze the simulations further, three planes through the domain are shown in Fig. 5.9 at arbitrary time steps that best illustrate the physical process. The decreasing water saturation with hydrophobicity and the preferential occupation of larger pores are clearly illustrated.



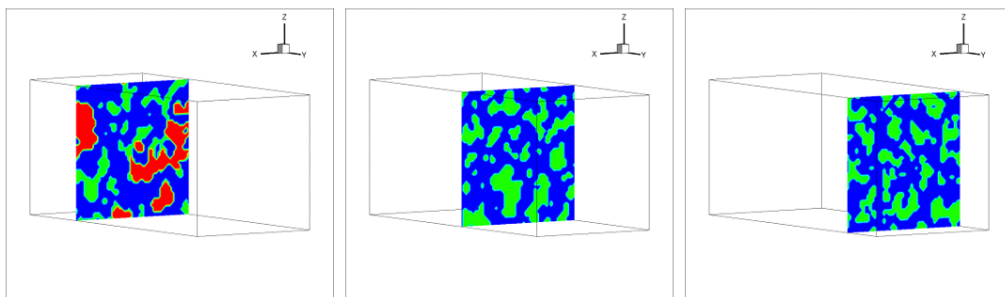
(a)



(b)



(c)



(d)

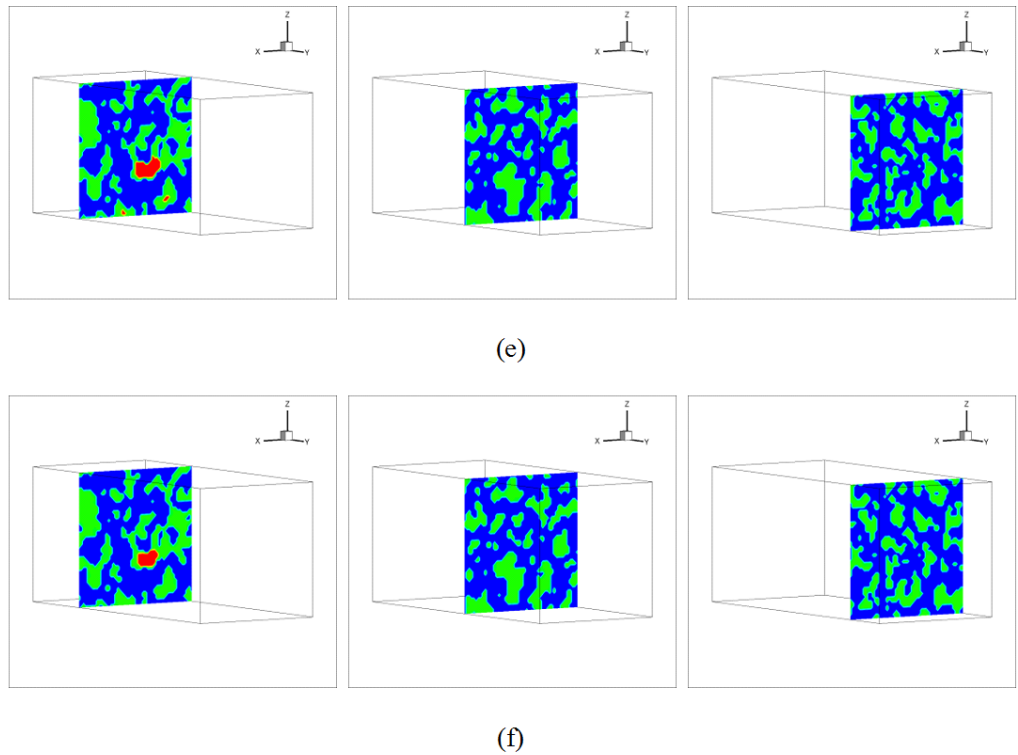
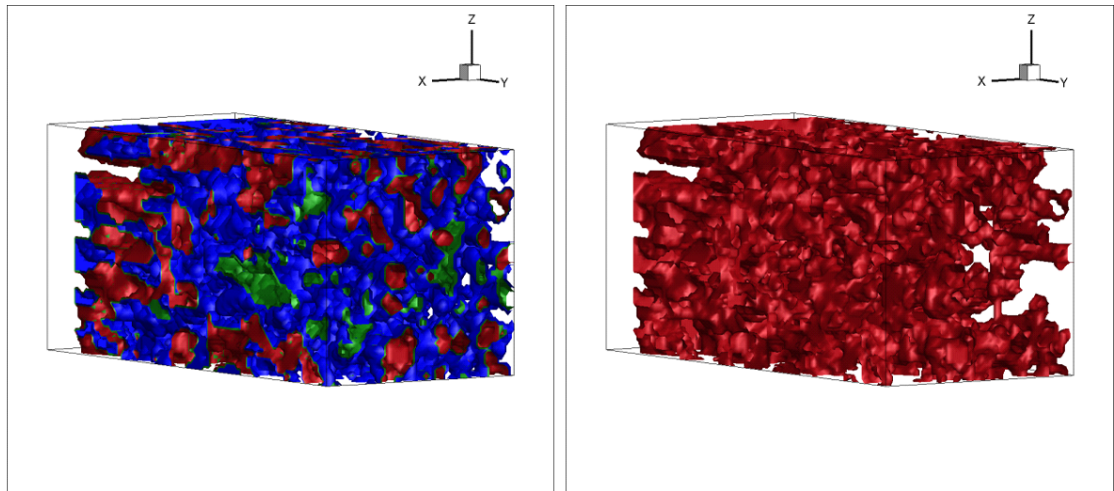


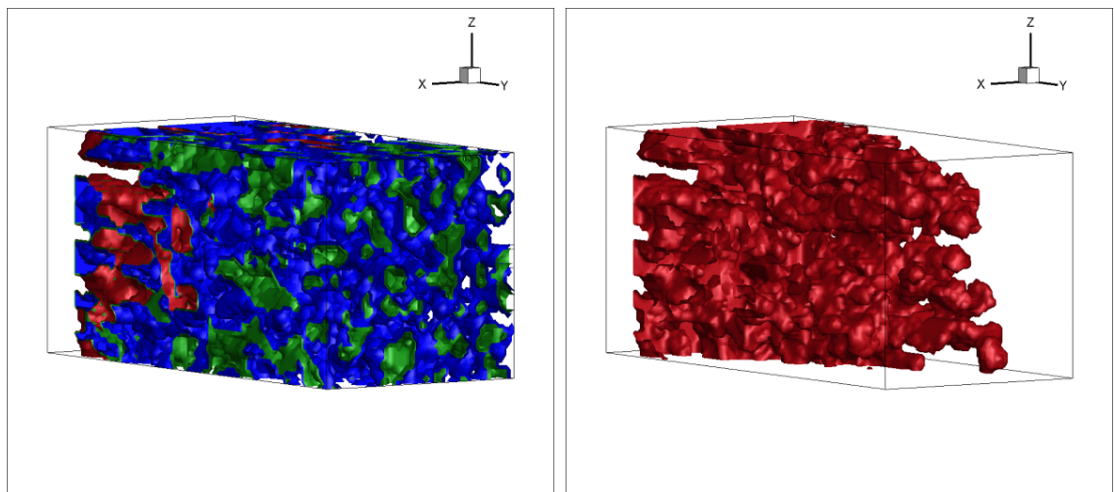
Figure 5.9: Visualization of water distribution after $2.3 \mu\text{s}$ in reconstructed catalyst layers with $\delta p = .0017$, $M = 54$, and different contact angles: a) $\theta = 105^\circ$ b) $\theta = 110^\circ$ c) $\theta = 115^\circ$ d) $\theta = 120^\circ$ e) $\theta = 130^\circ$ f) $\theta = 140^\circ$. Red: water, green: air, blue: solid structure.

Since viscosity changes with operating temperature, the effect of the viscosity ratio on water transport is considered in Fig. 5.10. A dynamic viscosity ratio (M) of 18 corresponds to fuel-cell operation at 80 Celsius degree [34]. Comparing Fig. 5.10 with Fig. 5.8 for the same pressure gradient, there is no substantial change in water-transport patterns with viscosity ratio, but water saturation does increase with viscosity ratio. Water also wets more area for the whole range of contact angles in Fig. 5.11 than in Fig. 5.9. Therefore, temperature changes, which in a fuel cell are most pronounced during start-up, lead to viscosity changes that are expected to give rise to accelerated water transport in fuel cells even for higher super-hydrophobic contact angles. This phenomenon can be attributed to the lubricating effect, which means that transfer of non-wetting fluid is affected by transferring momentum between wetting and non-wetting fluids in pores [13,23]. Detailed on screen computer visualization (not shown here) indicates as noted earlier, that water in a hydrophobic medium tends to move to bigger pores, and, conversely, air tends to move to smaller pores. Coupling between

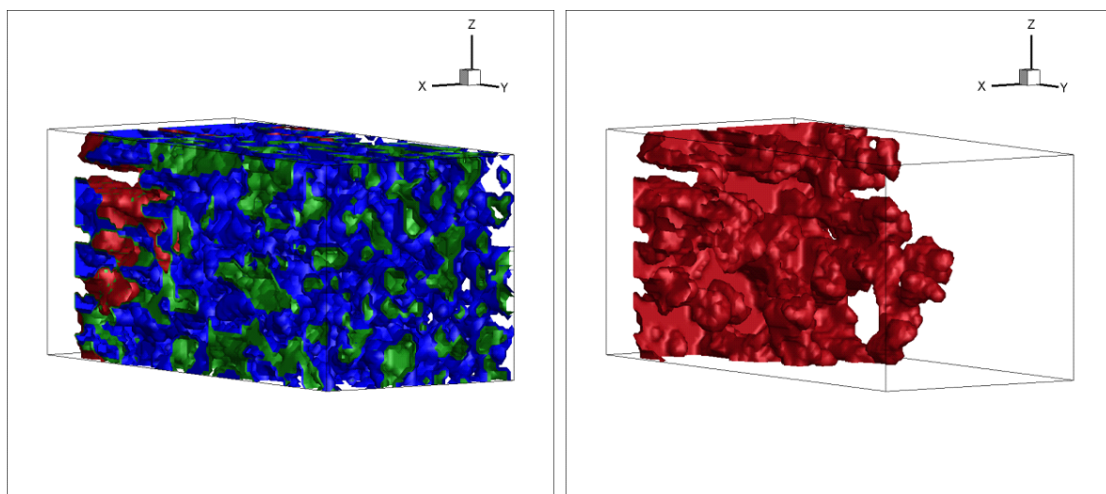
the viscosities of wetting and non-wetting fluids enhances water transport (faster or higher saturation when the viscosity ratio decreases). This may partially explain experimental observations of increasing water saturation in PEM fuel-cell electrodes after start-up [30,31]. Other factors may involve thermocapillary transport.



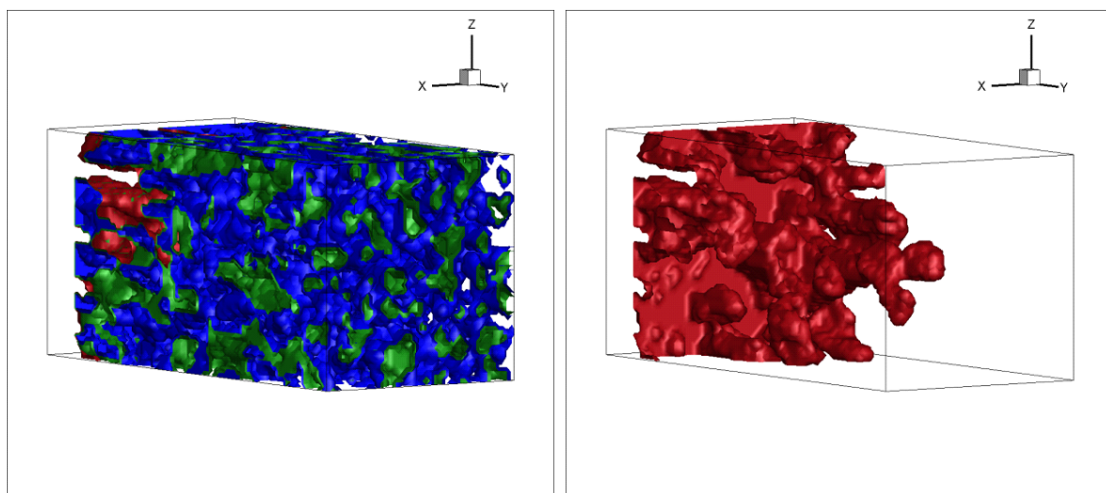
(a)



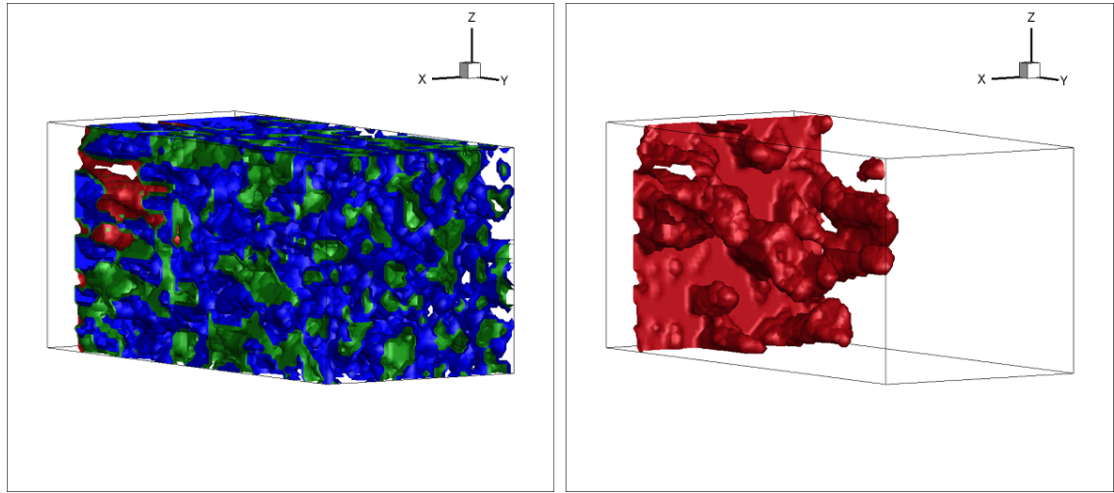
(b)



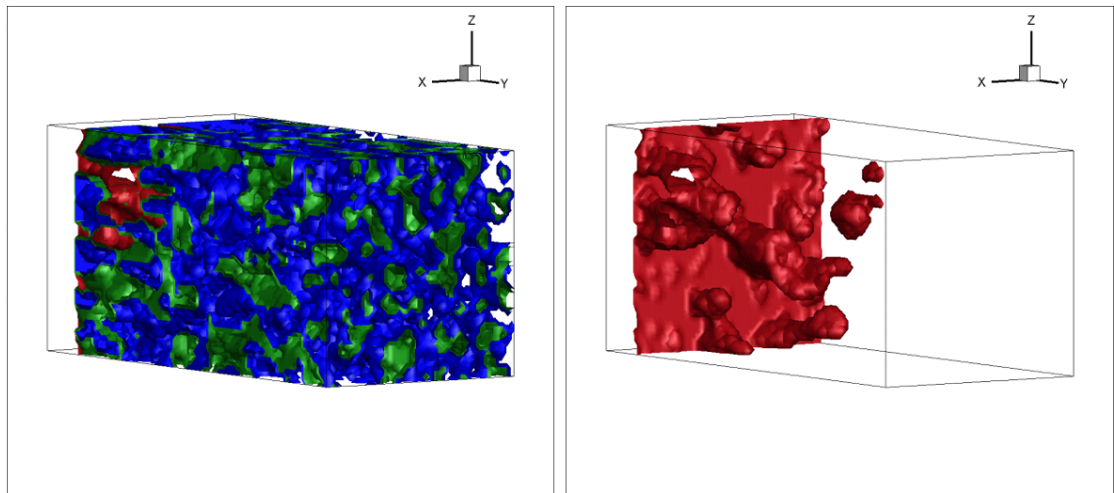
(c)



(d)

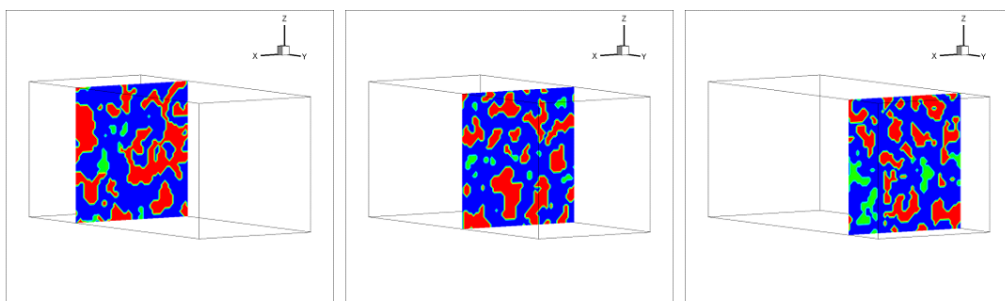


(e)

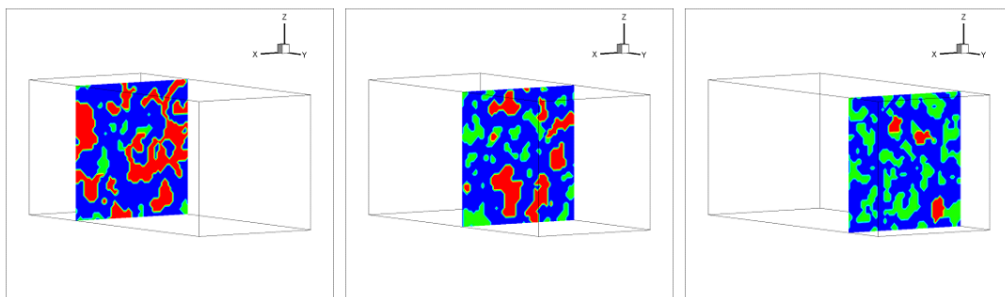


(f)

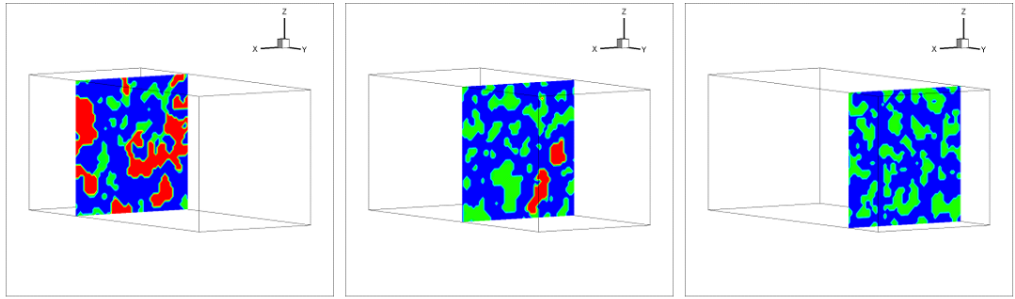
Figure 5.10: Visualization of water transport after $2.37 \mu\text{s}$ in reconstructed catalyst layers with $\delta p = .0017$, $M = 18$, and assuming different contact angles: a) $\theta = 105^\circ$ b) $\theta = 110^\circ$ c) $\theta = 115^\circ$ d) $\theta = 120^\circ$ e) $\theta = 130^\circ$ f) $\theta = 140^\circ$. Left column (red: water, green: air, blue: solid structure); right column shows the isosurface of water at equilibrium status.



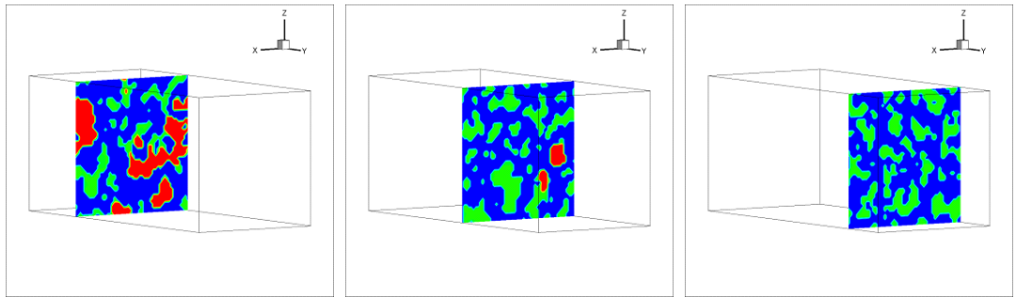
(a)



(b)



(c)



(d)

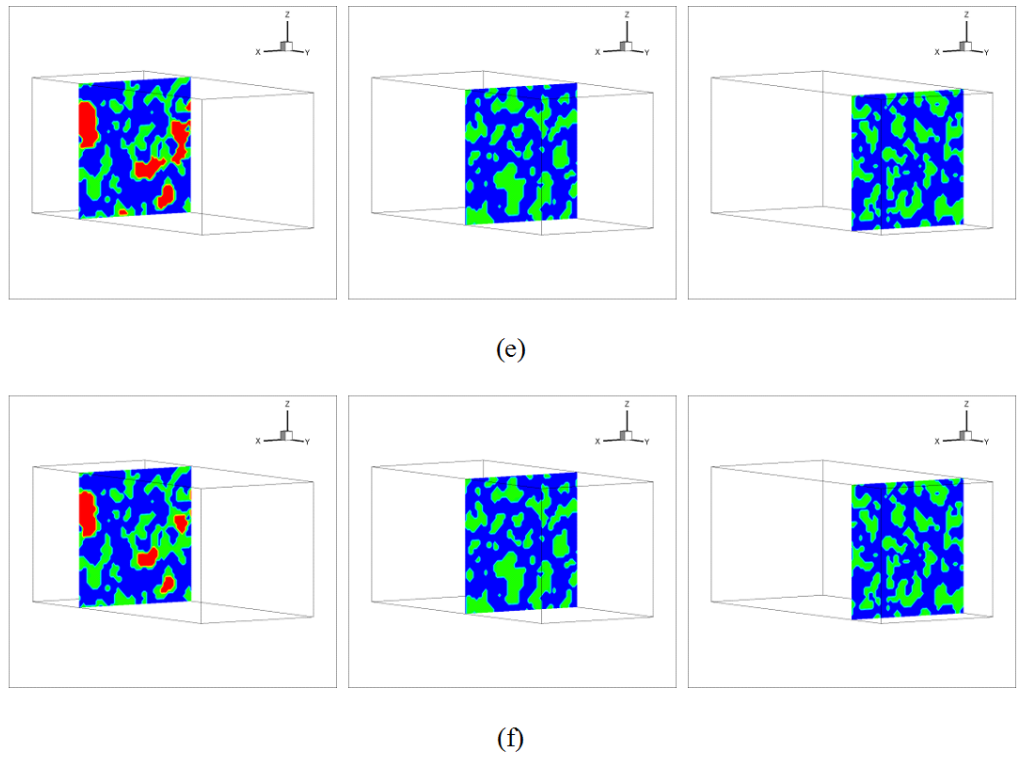
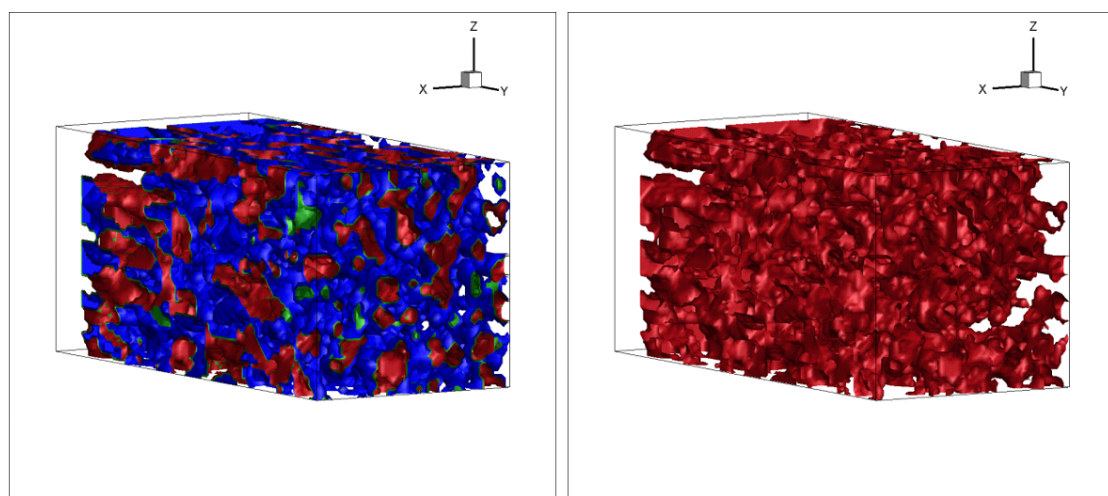
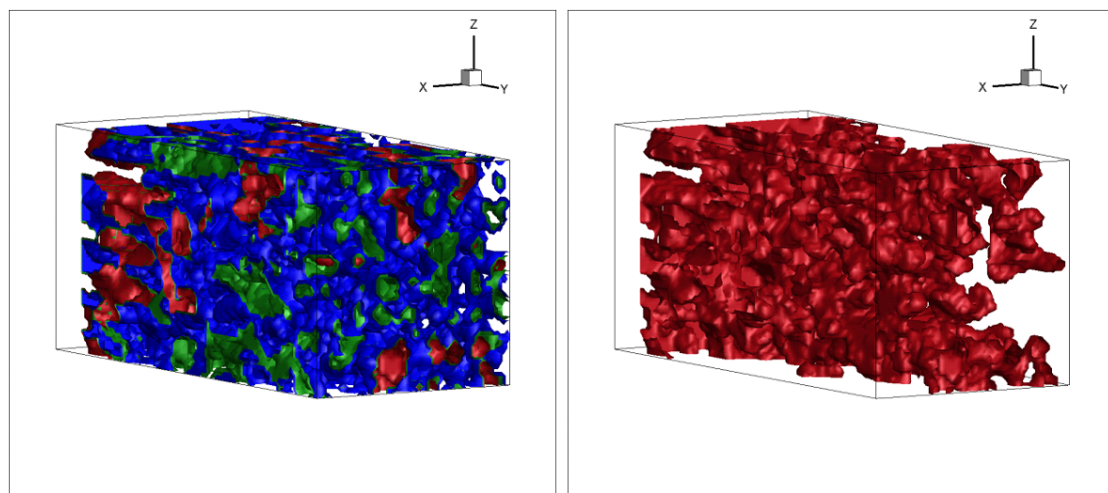


Figure 5.11: Visualization of water distribution after $2.37 \mu\text{s}$ in reconstructed catalyst layers with $\delta p = .0017$, $M = 18$, and assuming different contact angles: a) $\theta = 105^\circ$ b) $\theta = 110^\circ$ c) $\theta = 115^\circ$ d) $\theta = 120^\circ$ e) $\theta = 130^\circ$ f) $\theta = 140^\circ$. Red: water, green: air, blue: solid structure.

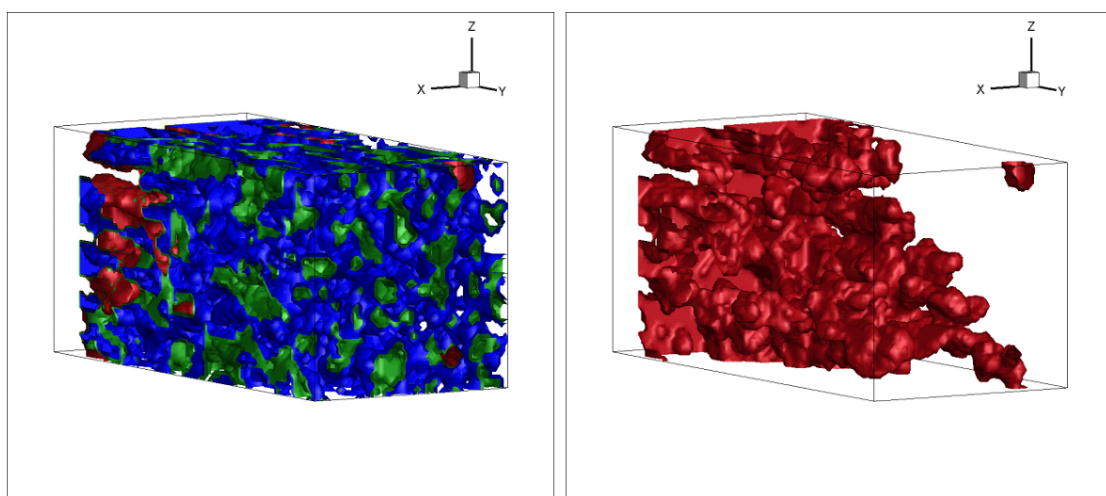
Simulations were also performed to examine the effect of the pressure gradient, showing no perceptibly significant effect on the water pattern, which remained largely dependent on wettability, but an overall increase in water saturation compared to the results obtained in case 1 (Figs. 5.8 and 5.9). Next, the combined effects of decreasing viscosity ratio and increasing pressure gradient simultaneously were examined. Water saturation increased significantly compared to base case 1, as shown in Fig. 5.12, and transition in the water pattern still occurs for a contact angle of $\theta = 110^\circ$, but the capillary fingering pattern is not dominant in this case.



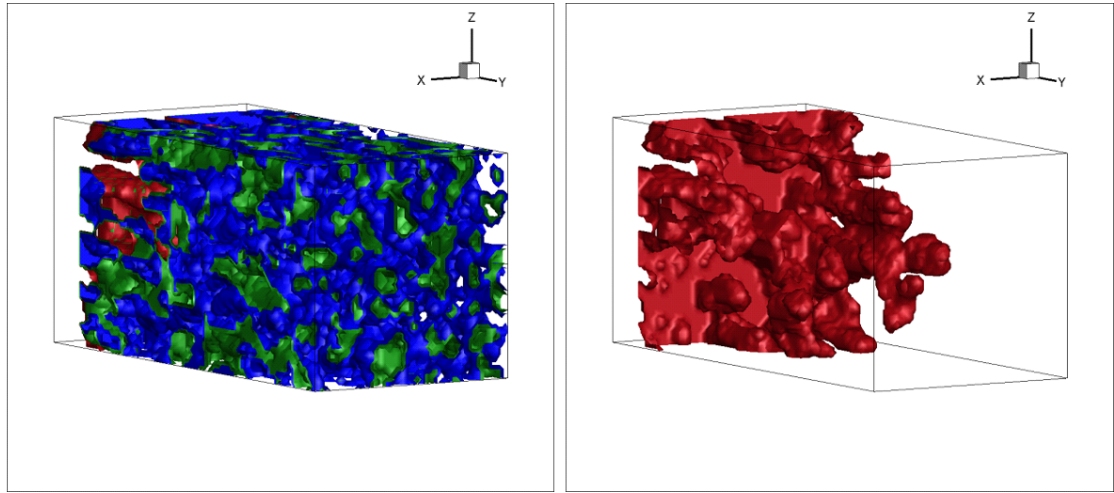
(a)



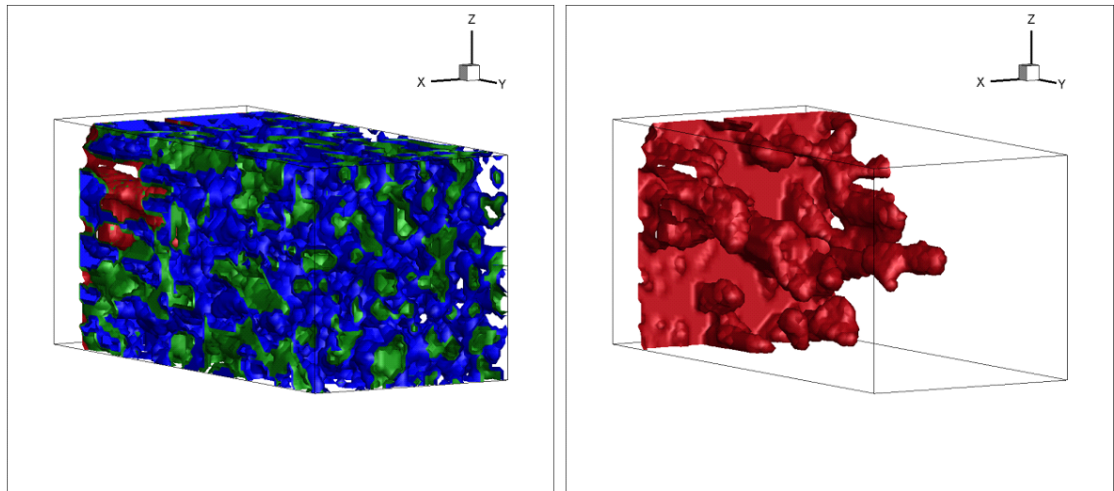
(b)



(c)



(e)



(f)

Figure 5.12: Visualization of water transport after $2.37 \mu s$ in reconstructed catalyst layers with $\delta p=0.0034$ ($=226.6$ KPa), $M=18$, and assuming different contact angles: a) $\theta = 105^\circ$ b) $\theta = 110^\circ$ c) $\theta = 115^\circ$ d) $\theta = 120^\circ$ e) $\theta = 130^\circ$ f) $\theta = 140^\circ$. Left column (red: water, green: air, blue: solid structure); right column shows the isosurface of water at equilibrium status.

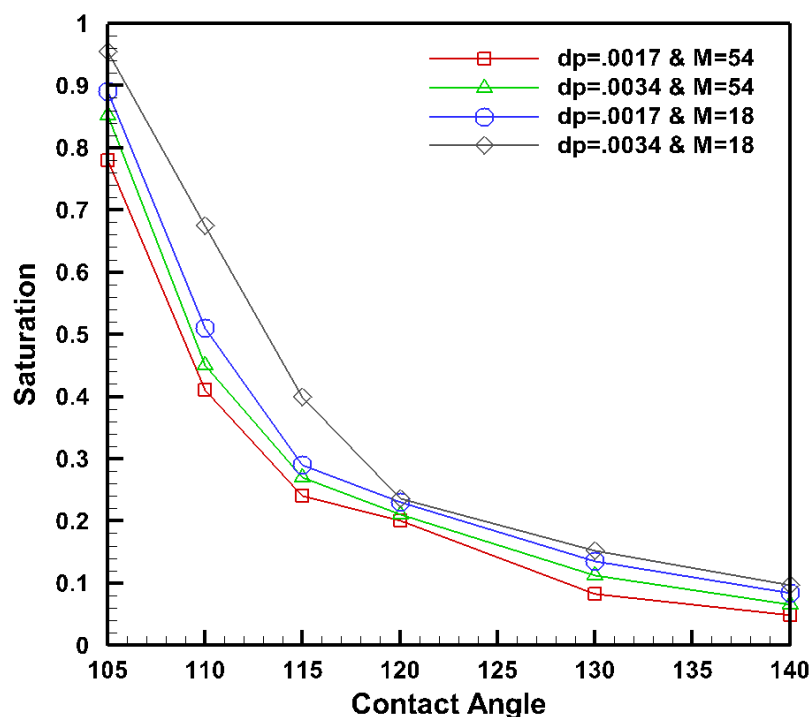


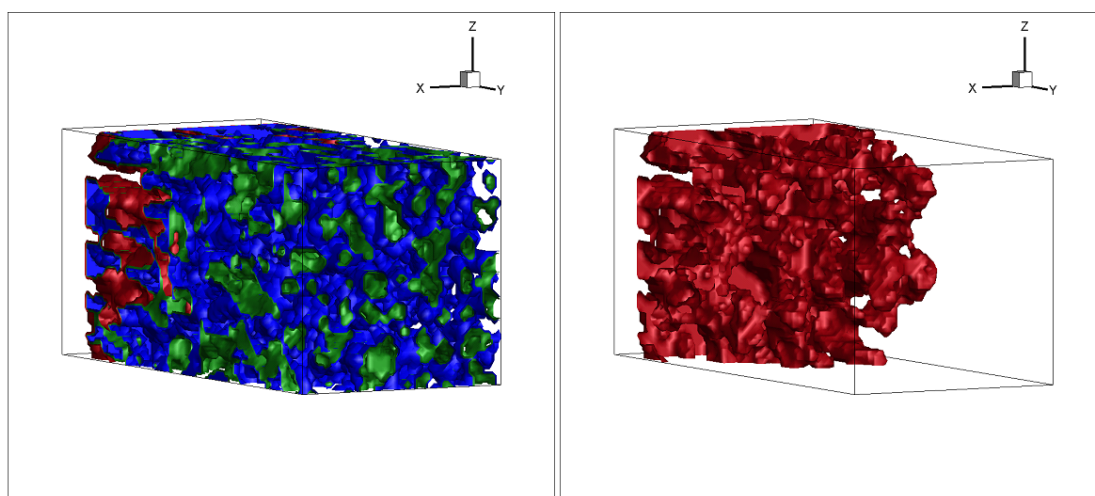
Figure 5.13: Simulated water saturation versus contact angle considering the effects of different pressure gradients and viscosity ratios.

Fig. 5.13 summarizes the effects of different contact angles for the four combinations of pressure drop and viscosity ratios examined. Water saturation decreases with increasing hydrophobicity in all cases. At lower contact angles, the saturation and risk of flooding increase with potential blockage of percolation pathways for air. Contact angles between $\theta = 110^\circ$ to $\theta = 115^\circ$ appear to ensure sufficiently low saturation.

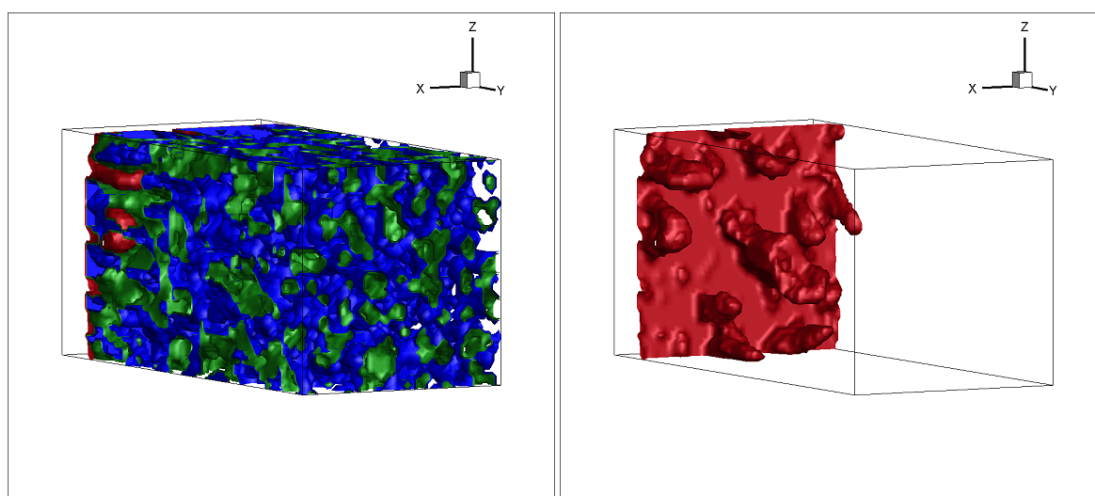
5.2.1 Effect of Surface Tension

Surface tension is a force that tends to minimize the size of a liquid surface and to increase resistance to deformation by external forces. The effect of surface tension becomes more significant at smaller scales and potentially dominant in catalyst layer pores that are in the order of nanometres wide. In a fuel cell starting from cold conditions, the operating temperature gradually increases to 80 degrees Celsius or higher, and correspondingly surface tension decreases linearly with temperature. It is therefore of interest to elucidate the effect of surface tension as temperature varies. For the first test, the effect of reduced surface tension is examined compared to the reference case shown in Fig. Fig. 5.8. For the sake of brevity, only two contact

angles are presented in Fig. 5.14 and should be compared to Fig. 5.8 (b) and (e). Lower surface tension does not alter the water pattern significantly, and the process appears to be primarily determined by the wettability potential or contact angle. Diminishing surface tension does result in slightly lower water penetration into the domain, specifically for contact angles less than $\theta = 130^\circ$, as shown in Fig. 5.15. The results show that surface tension has a negligible effect in super-hydrophobic regimes and a stronger effect on stable displacement and transient regimes. This can be explained by examining the role of surface tension in the three distinct water patterns. As stated earlier, water pattern is determined by contact angle. As a result, surface tension in capillary fingering tends to minimize surface energy as well as interfacial surface between two fluids. However, in the stable displacement regime and to some extent in transient regimes as well, surface tension acts as a resistive force at the interface and hinders penetration of more water into the domain.



(a)



(b)

Figure 5.14: Visualization of water transport after $2.3 \mu\text{s}$ in reconstructed catalyst layers with $\delta p = .0017$, $M = 54$, $\sigma = .0625$, considering different contact angles: a) $\theta = 110^\circ$ b) $\theta = 130^\circ$. Left column (red: water, green: air, blue: solid structure); right column shows the isosurface of water at equilibrium status.

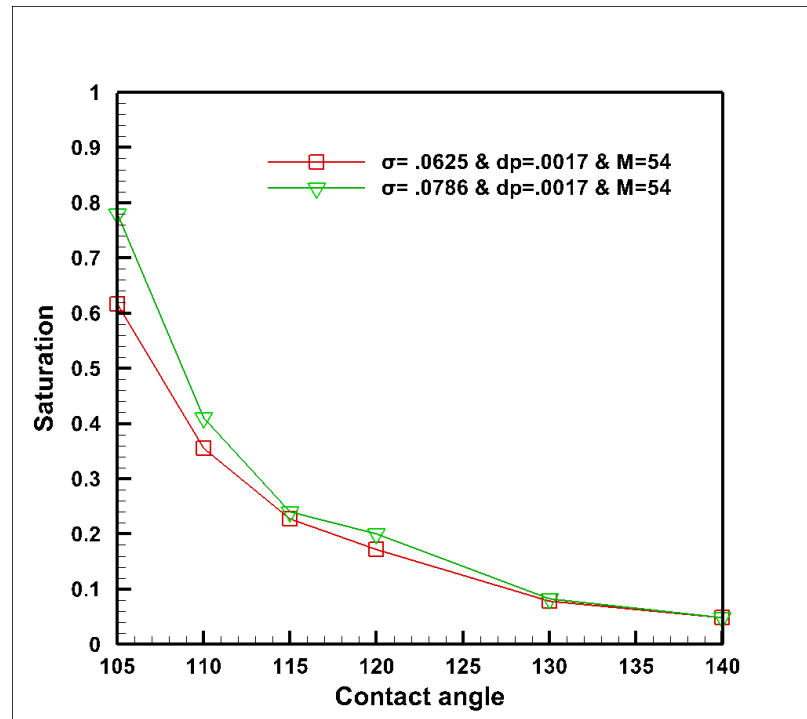


Figure 5.15: Simulated water saturation versus contact angle considering the effect of different surface tension values.

We next examine the effect of decreasing surface tension and dynamic viscosity ratio simultaneously. Due to a lubrication effect, more water is driven into and saturates the domain, as shown in Fig. 5.16. As in the previous case, lower surface tension reduces saturation for lower contact angles, as shown in Fig. 5.17. This can be attributed to the impact of surface tension on the different regimes. Figure 5.16 (a), shows a noticeable influence of decreased surface tension on stable displacement and transient regimes for contact angles less than $\theta = 115^\circ$.

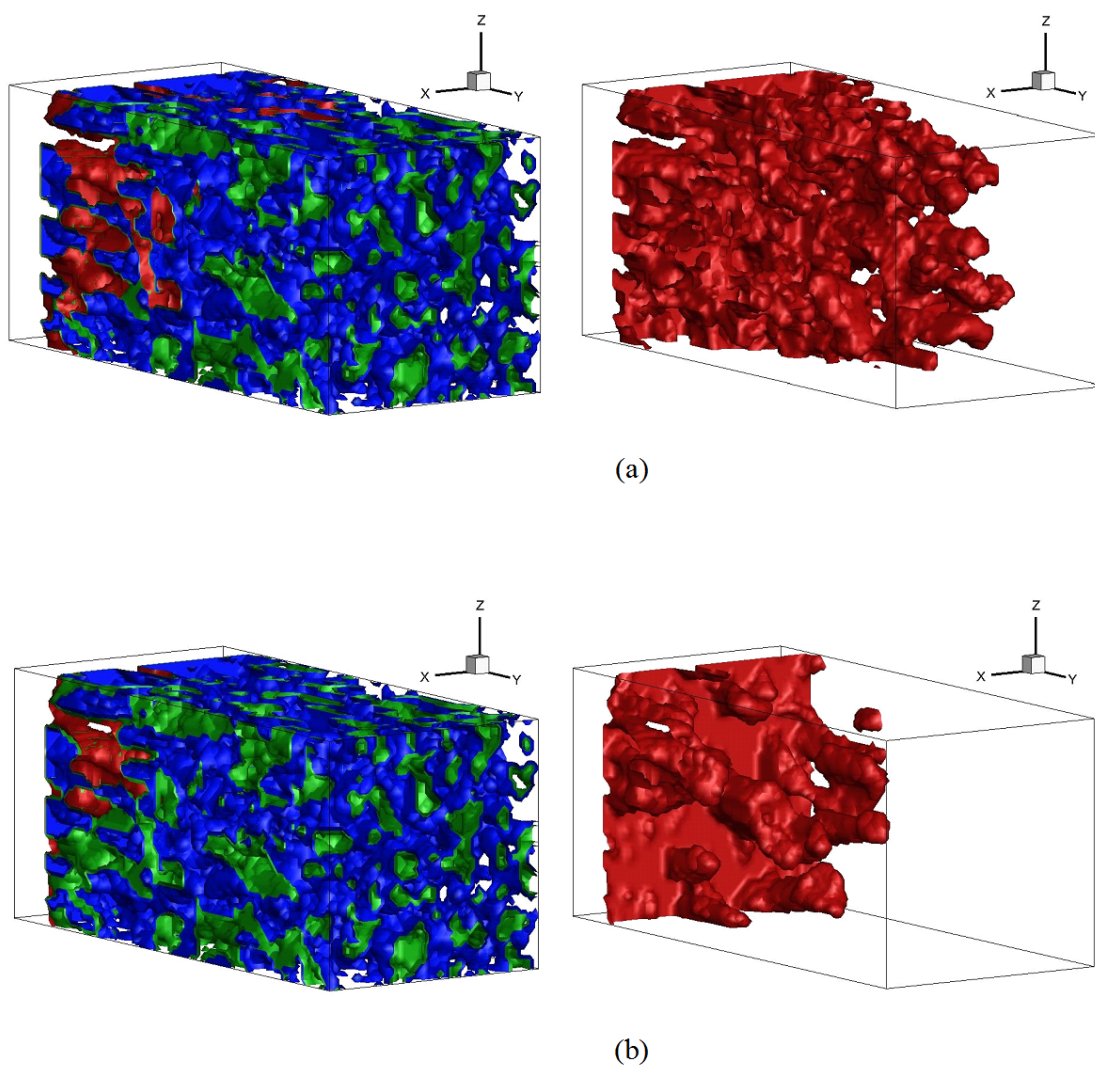


Figure 5.16: Visualization of water transport after $2.37 \mu\text{s}$ in reconstructed catalyst layers with $\delta p = .0017$, $M = 18$, $\sigma = .0625$, and considering different contact angles: a) $\theta = 110^\circ$ b) $\theta = 130^\circ$. Left column (red: water, green: air, blue: solid structure); right column shows the isosurface of water at equilibrium status.

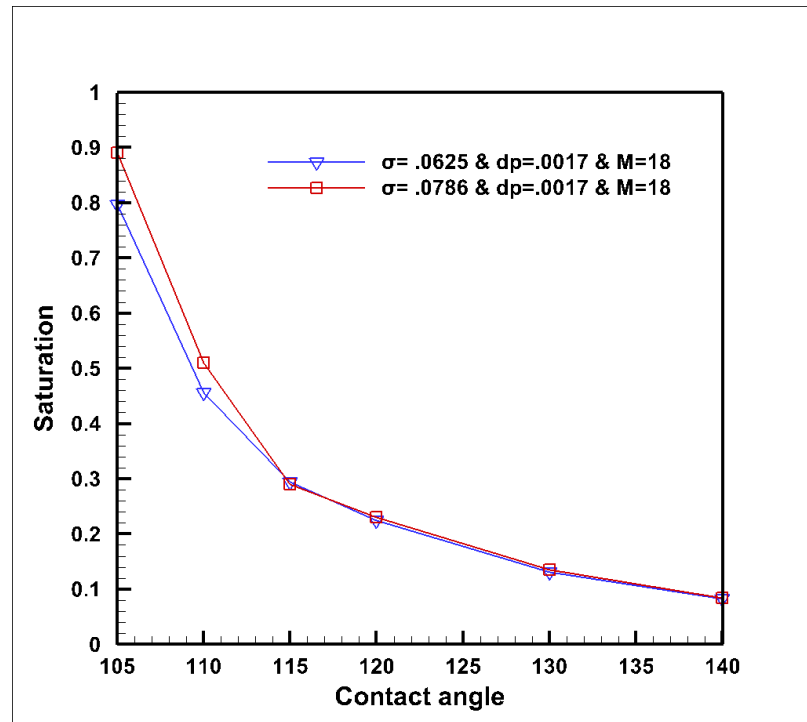


Figure 5.17: Simulated water saturation versus contact angle considering the effect of different surface tension values.

Finally we examine the simultaneous effect of increasing pressure gradient and reducing dynamic viscosity ratio. This results in higher saturation, as shown in Fig. 5.18. Although decreasing surface tension does have a small effect on water saturation, especially at contact angles $< \theta = 110^\circ$ and in purely stable displacement regimes, it primarily provides a resistive force against external pressure changes and viscous forces in stable displacement regimes. On the other hand, in the capillary fingering regime, surface tension maintains fingering by minimizing sizes and energies.

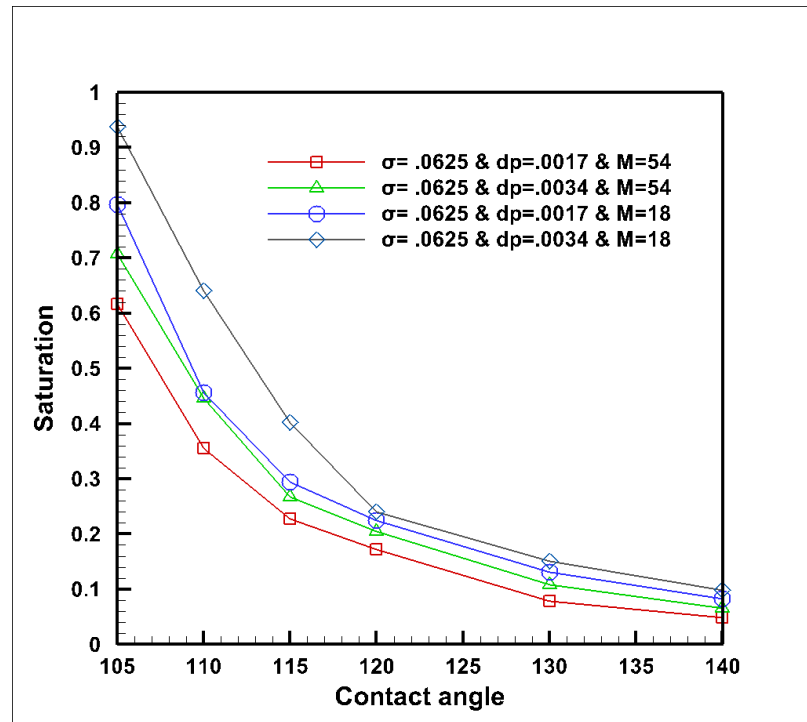


Figure 5.18: Variation of water saturation with contact angle considering the effects of different pressure gradients and viscosity ratios.

5.3 Capillary Pressure in a Reconstructed Catalyst Layer

Water transport in the nano-scale structure of catalyst layers is strongly dominated by capillary forces. According to the Young-Laplace formula given in Eq. (5.4), the capillary pressure is inversely related to pore-size radii and directly proportional to the contact angle of CL materials and the surface tension between liquid and gas fluids.

In macroscopic porous transport simulations including the effect of capillary pressure, one of the widely used methods to determine capillary pressure is the Leverett-J function, expressed in Eq. (5.5). In this expression, σ , ϵ , k , and S represent the surface tension, porosity and absolute permeability of the porous media and the saturation of the liquid phase respectively. This expression was derived based on curve fitting to experimental capillary pressure data for soil porous media. This expression is also widely used to model two-phase flow problems for porous PEMFC structures. In fact, the geometries of porous fuel-cell components are completely different from

soil porous structures. Accordingly, alternative models have been suggested by a few groups [6]:

$$P_c = \sigma \cos(\theta) \left(\frac{\epsilon}{k}\right)^5 (1.417S - 2.12S^2 + 1.263S^3) \quad (5.5)$$

LaManna et al. [98] suggested a modified version of the Leverett-J function for CL porous structures, as expressed in Eq. (5.6). They derived this expression by curve fitting to their experimental data for a catalyst layer sample. Another method widely used to describe capillary pressure in porous media is the Van Genuchten model, which is shown in Eq. (5.7) [99]. In this equation, the parameters P_d and m are fitting parameters, and S corresponds to saturation of the liquid phase:

$$P_c = \sigma \left(\frac{\epsilon}{k}\right)^5 (3.02343S^3 - 2.35638S^2 + .55602S) \quad (5.6)$$

$$P_c = P_d [(1 - S)^{\left(\frac{-1}{m}\right)} - 1]^{(1-m)} \quad (5.7)$$

In this research, the capillary pressure for the reconstructed catalyst layer illustrated in Fig. 5.7 was simulated using the two-phase lattice Boltzmann method. The contact angle for the CL hydrophobic porous media was set to $\theta = 110^\circ$ degree. Figure 5.19 shows simulated capillary pressure results for different liquid water saturations. The cross symbols represent simulated numerical results. The solid green and blue lines correspond to curves fitted using a polynomial and the Van Genuchten model. The experimental data from LaManna et al. [98] and the Leverett-J function are illustrated in red and black respectively. Figure 5.19 clearly shows that the standard Leverett-J function either over-predicts or under-predicts capillary pressure values. The fitted capillary pressure described by Eq. (5.8) based on LBM simulations can provide more accurate predictions of capillary pressure for CL porous structures than the standard Leverett-J function.

The impact of different contact angles on the simulated capillary pressure is illustrated in Fig. 5.20. The simulated results indicate that increasing hydrophobicity of CL materials leads to an increase in resistance against water movement through CL porous structures. Hence, less water can penetrate into the structures, and higher external pressure is necessary to drive liquid water into the CL porous medium:

$$P_c = \sigma \left(\frac{\epsilon}{k}\right)^5 (2.05S^3 - 0.9161S^2 + .3946S) \quad (5.8)$$

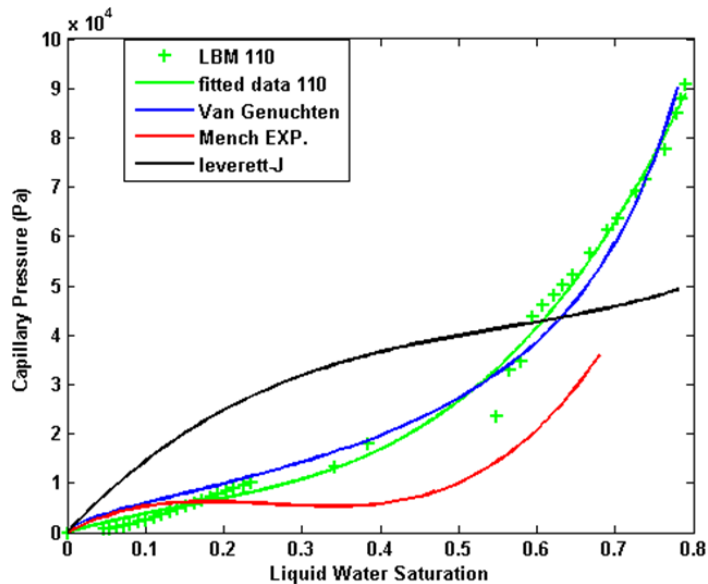


Figure 5.19: Capillary pressure in the reconstructed catalyst layer

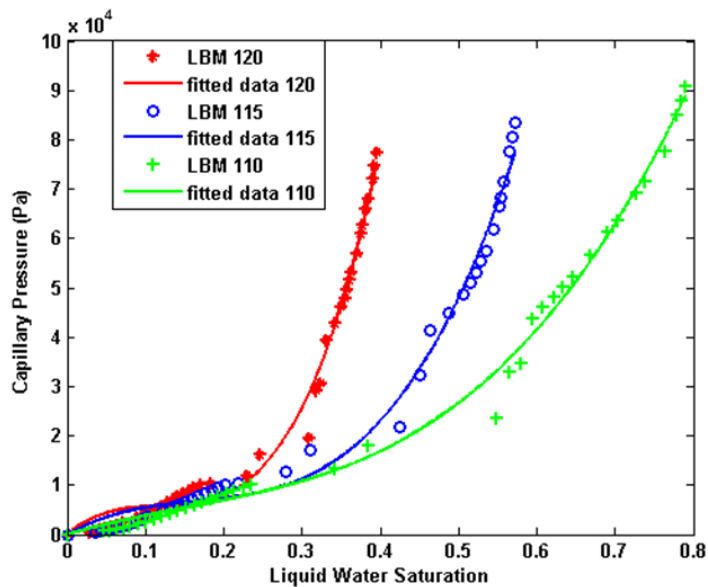


Figure 5.20: Effect of different contact angles on capillary pressure

5.4 Impact of Liquid Water on Transport Parameters in Catalyst Layers

This section investigates the effect of liquid water on the transport parameters through the 3D stochastic reconstructed CL shown in Fig. 5.21. The CL sample was reconstructed with $305 \times 235 \times 252$ grid cells at an isotropic resolution of 5.95 nm. This reconstructed geometry was used in an earlier study [13] to determine the effective transport parameters without accounting for liquid water impact. In the present study, liquid water was introduced into the domain as a new phase in conjunction with other solid and gas phases in the CL. The reconstructed CL therefore consists of five phases: carbon black particles and the ionomer phase, which enable conduction of electrons and protons respectively; pores, which enable transport of reactants; non-volumetric Pt at reaction sites located at the interface of the carbon particles and the ionomer phase; and generated liquid water due to oxygen reduction reaction (ORR) at the cathode CLs.

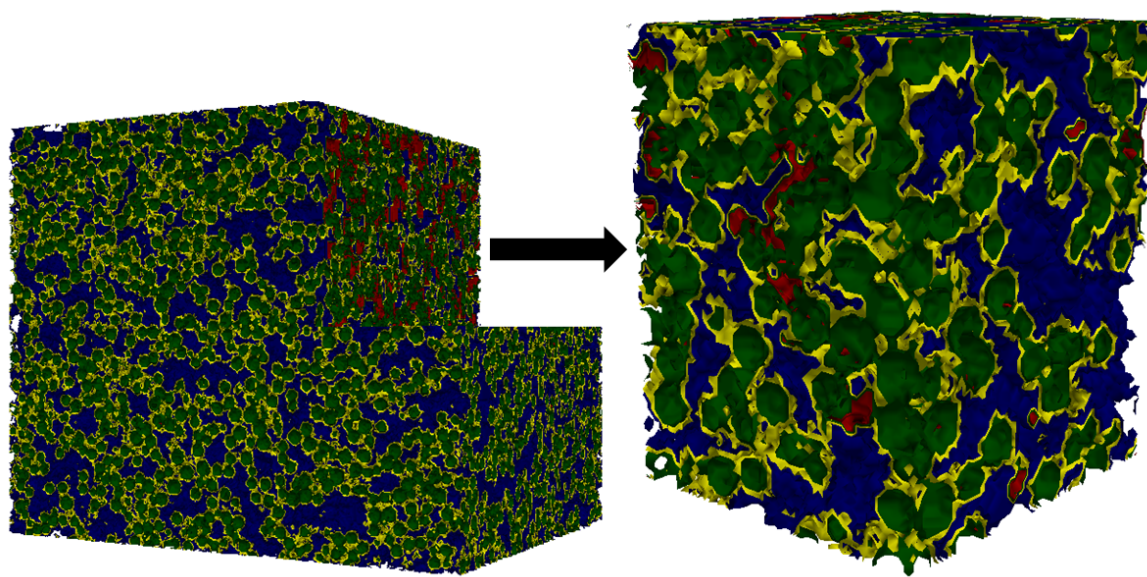


Figure 5.21: 3D model of the reconstructed CL including ionomer, carbon spheres, water, and pores (ionomer: yellow, carbon: green, water: red, and pores: blue).

Due to different CL material wettability properties, the contact angles of the ionomer and carbon phases were chosen as $\theta = 120^\circ$ and $\theta = 80^\circ$ respectively. The effects of different ionomer surface wettability conditions and pressure gradients are examined in the following sections. The determination of the effective transport

properties is done via a sequence of steps combining LBM and PSM simulations. First, the simulations are initiated by randomly distributing liquid water throughout the CL to achieve a predefined saturation level. The two-phase LBM is then used to determine the equilibrium water distribution. The volumes of liquid water at the equilibrium locations are then introduced in the pore-scale simulation as an additional stationary heat-conducting, non-electric, and non-proton conductive phase. Finally, pore-scale simulations using a finite-volume method (FVM) are carried out to determine mass, charge, and heat transport through the CL accounting for the presence of liquid water. These simulations were performed by introducing the additional liquid water phase in a pore scale modelling (PSM) code developed by Lange, Djilali and coworkers [14, 81, 82]. The PSM allows highly resolved parallel simulations and is described in details in [95].

Figure 5.22 presents the simulated values of effective oxygen and water-vapour diffusivities and effective proton, electron, and thermal conductivities as functions of liquid water saturation throughout the reconstructed CL domain. In these simulations, the liquid water saturation varied between 10% to 80 %. In the first case, a pressure gradient equal to 1.6×10^{-5} (=2.7 KPa) was applied to drive water through the pores until it reaches equilibrium conditions.

The simulations reveal that the most sensitive properties to the presence of liquid water are effective oxygen and water-vapour diffusivities and effective thermal conductivity. The effective oxygen and water-vapour diffusivities decrease by 96 % and 88% respectively as the liquid water saturation increases from 0% to 80%. This is a direct effect of liquid water hindering air pathways and constricting or blocking open pore spaces for reactants to reach reaction sites. The effective electron and proton conductivities, on the other hand, remained unchanged over all the simulations. However, it should be noted that in all our simulations the protonic conductivity is just a function of relative humidity. Therefore, in order to properly model the sensitivity of protonic conductivity to different liquid water saturations, a model that accounts for the variation of σ_m with local liquid water saturation needs to be developed and deployed. Effective thermal conductivity is significantly affected by differences in liquid water saturation. Thermal conduction is promoted by the presence of liquid water which has a thermal conductivity approximately 25 times greater than that of air. Consequently the effective thermal conductivity increases by 134% when the liquid water saturation reaches 80%. Furthermore, higher liquid water saturations increase thermal percolation pathways through the CL. Therefore, increasing the liquid water

saturation gives rise to higher thermal conductivity and can alleviate the possibility of hot spots formation in the CL [100, 101].

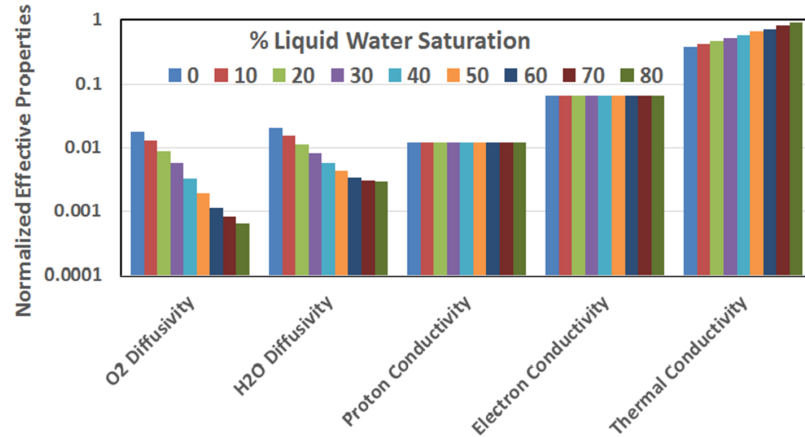


Figure 5.22: Impact of different liquid water saturations on effective oxygen and water-vapour diffusivities and on proton, electron, and thermal conductivities.

5.4.1 Effect of Different Contact Angles

It is well known that ionomer wettability decreases with increasing temperature [102–104]. The contact angle of an ionomer surface has been reported to change from a hydrophobic to a hydrophilic surface over time [102–104]. This section describes simulations that were performed to examine the effect of different ionomer contact angles on water transport. In these simulations, the exerted pressure gradient across the CL domain was set to $3.2e-5$ (=5.4 KPa), and the ionomer contact angle was varied from a hydrophobic surface (120 degree) to a hydrophilic surface (80 degree).

Figs. 5.23 - 5.25 illustrate the simulated results for effective oxygen and water vapour diffusivities as well as thermal conductivity as a function of liquid water saturation for the cases of hydrophobic and hydrophilic ionomer contact angles. The comparison of the results in Figs. 5.23-5.24 indicates that for saturations less than 50%, the effective oxygen and water-vapour diffusivities show higher values corresponding to a hydrophilic ionomer, but for saturations greater than 50%, the hydrophobic ionomer leads to higher diffusivities. This can be attributed to the important role of the larger pores in the CL. For saturations less than 50%, water preferentially occupies large pores that have a hydrophobic ionomer surface, or small pores in the case of a hydrophilic ionomer. In addition, water prefers to lie on the surface in the case of hydrophilic ionomer, but it is repelled from the surface and occupies the larger

pores in the hydrophobic case. Therefore, with the same liquid water saturation (less than 50%), but with different ionomer wettability, the open pore spaces in the large pores are larger in the case of hydrophilic ionomer and lead to higher diffusivities for oxygen and water vapour.

The results also indicate that increasing liquid water saturation to more than 50% with a hydrophobic ionomer surface permits more reactants to reach the reaction sites. The reason is that increasing liquid water saturation causes the large pores to become preferentially occupied, meaning that the effect of small pores dominates.

Since liquid water prefers to occupy small pores with a hydrophilic ionomer surface, the rate of reactant transport consequently reduced in the case of saturations higher than 50% compared to a hydrophobic ionomer surface.

Figures 5.25 illustrates the effective thermal conductivity as a function of different liquid water saturations for different ionomer contact angles. Clearly, for the entire range of saturations, the effective thermal conductivity is higher for the case of the hydrophilic ionomer than for the hydrophobic case. The reason lies in the importance of thermal percolation pathways through the CL. The hydrophilic ionomer surface causes the water to occupy small pores and to lie on the surface, hence increasing thermal percolation pathways.

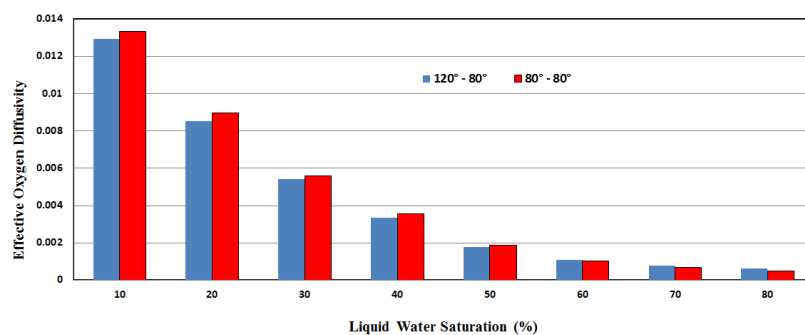


Figure 5.23: Impact of different ionomer contact angles on effective oxygen diffusivity.

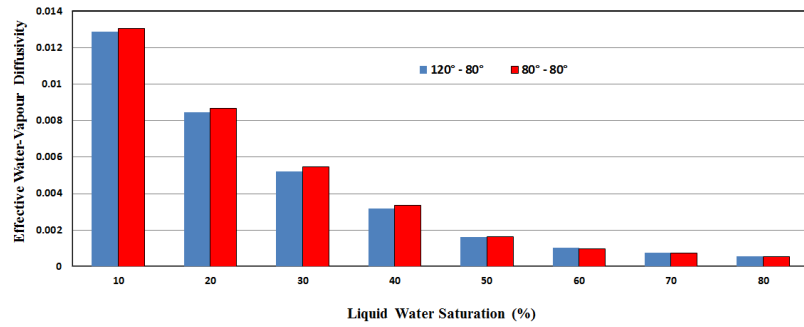


Figure 5.24: Impact of different ionomer contact angles on effective water-vapour diffusivity.

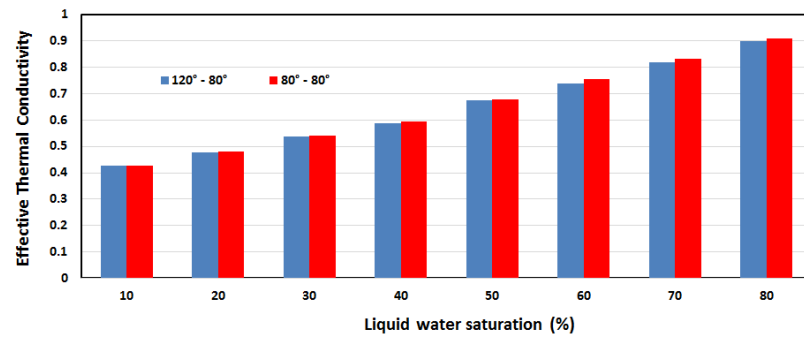


Figure 5.25: Impact of different ionomer contact angles on effective thermal conductivity.

5.4.2 Effect of Different Pressure Gradients

Increasing Pressure drop from $\delta p=1.6e-5$ (=2.7 KPa) to $\delta p=3.2e-5$ (=5.4 KPa)

This section examines the effects of different pressure gradients on transport properties. Figures 5.26 and 5.27 show the effective oxygen diffusivity versus liquid water saturation for various pressure gradients and ionomer contact angles. For the sake of brevity, the effects of liquid water on water-vapour diffusivity and thermal conductivity are illustrated in Figs. 5.28 and 5.29 for the hydrophobic ionomer surface case. The results indicate that for the entire range of liquid water saturations, oxygen and water-vapour diffusivities decrease when the pressure gradient exerted on the liquid water increases from $\delta p=1.6e-5$ (=2.7 KPa) to $\delta p=3.2e-5$ (=5.4 KPa). This increase causes smaller droplets of liquid water to push towards each other and coalesce to form bigger liquid water droplets in the large pores. Furthermore, it induces trapped

liquid water to come out of dead-end pores and coalesce with bigger liquid water droplets. At higher liquid water saturations, water moves further as the pressure gradient increases, blocking more open areas that serve as reactant transport and hence limiting oxygen and water-vapour diffusivities further. The decrease in effective thermal conductivity with increasing pressure gradient is due to the reduction of thermal percolation pathways through the CL.

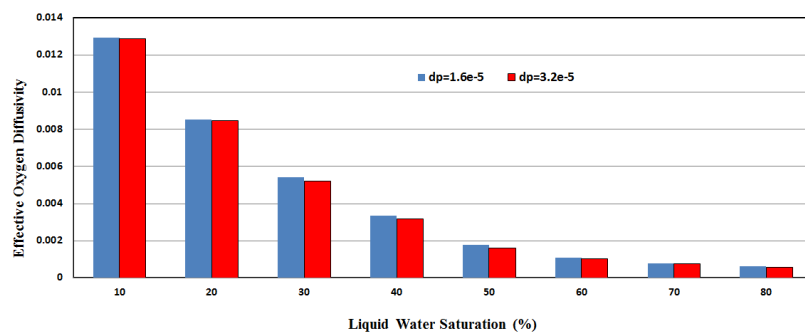


Figure 5.26: Impact of different pressure gradients on effective oxygen diffusivity with hydrophobic ionomer surface.

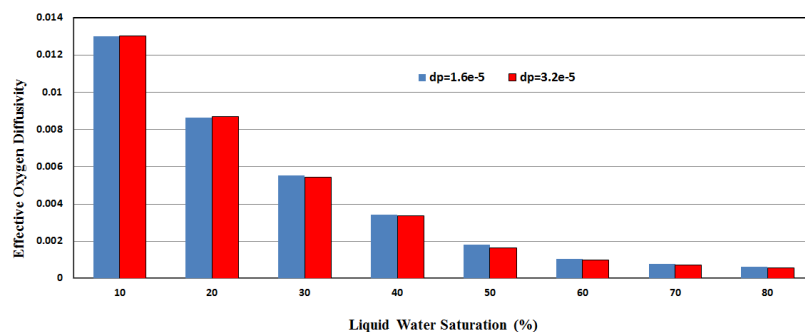


Figure 5.27: The impact of different pressure gradients on the effective oxygen diffusivity with hydrophilic ionomer surface.

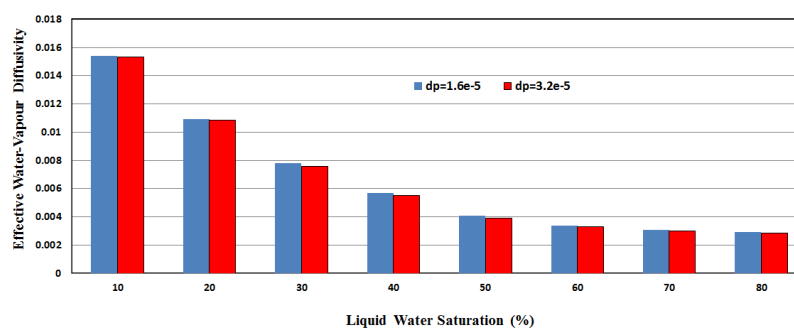


Figure 5.28: Impact of different pressure gradients on effective water-vapour diffusivity with hydrophobic ionomer surface.

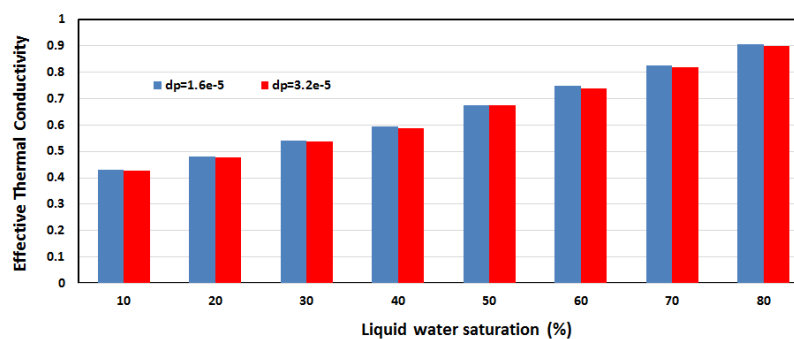


Figure 5.29: Impact of different pressure gradients on effective thermal conductivity with hydrophobic ionomer surface.

Increasing Pressure Gradient

Increasing the pressure gradient further (from $\delta p=3.2e-5$ (=5.4 KPa) to $\delta p=4.8e-5$ (=8.1 KPa)) causes the larger interconnected liquid water droplets to break-up into smaller ones and to create more open spaces in the large pores, as illustrated in Fig. 5.33. In addition, the increase in the pressure gradient stretches the small liquid water droplets, turns them into elongated strips, and simultaneously push them out of the large pores. This implies that the effective oxygen and water-vapour diffusivities increase further compared to Figs. 5.26-5.28. As shown in Fig. 5.34, in the case of higher liquid water saturation, the large pores are mostly occupied, and therefore separation and break-up of the large water droplets does not occur as readily compared to cases of lower liquid water saturation. At higher liquid water saturations, water stretches with increasing pressure gradients, hindering reactant pathways and reducing oxygen and water-vapour diffusivities further. Similarly to the previous case,

increasing the pressure gradient decreases thermal percolation pathways, leading to a drop in effective thermal conductivity.

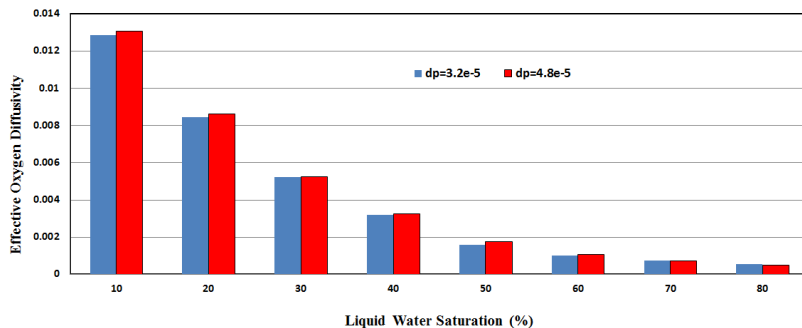


Figure 5.30: Impact of different pressure gradients on effective oxygen diffusivity with hydrophobic ionomer surface.

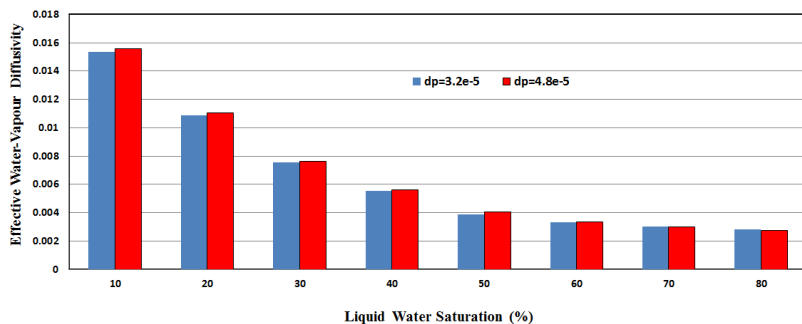


Figure 5.31: Impact of different pressure gradients on effective water-vapour diffusivity with hydrophobic ionomer surface.

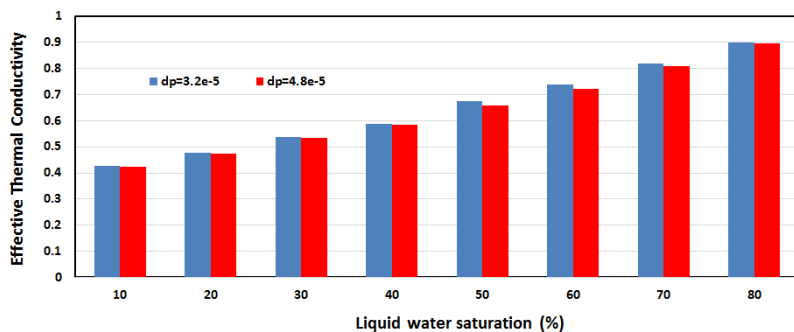


Figure 5.32: Impact of different pressure gradients on effective thermal conductivity with hydrophobic ionomer surface.

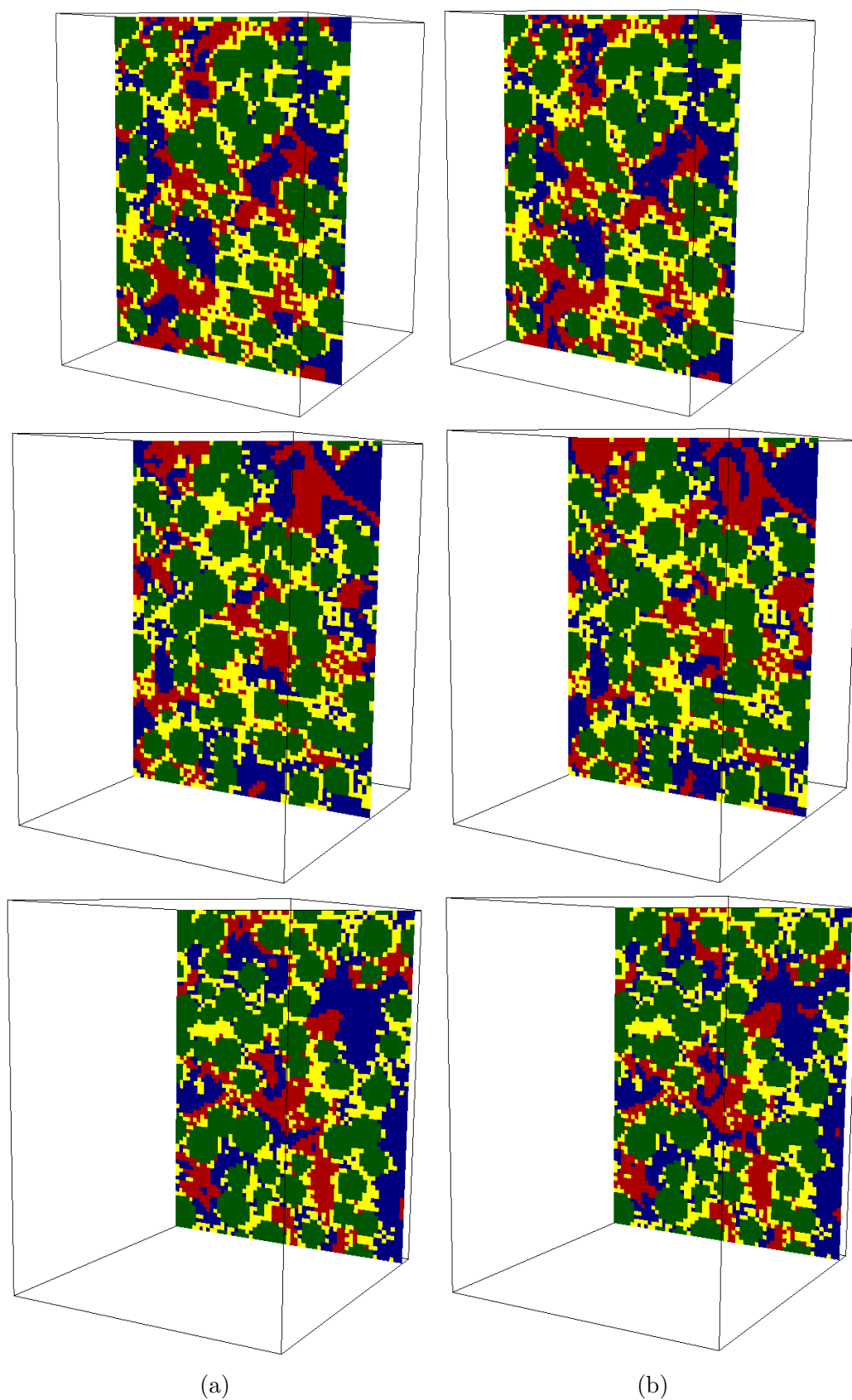


Figure 5.33: Impact of different pressure gradients on water distribution with $S=40$ and hydrophobic ionomer surface shown in three slices through the CL structure: **a)** $\delta p=3.2 \times 10^{-5}$ (=5.4 KPa) **b)** $\delta p=4.8 \times 10^{-5}$ (=8.1 KPa)

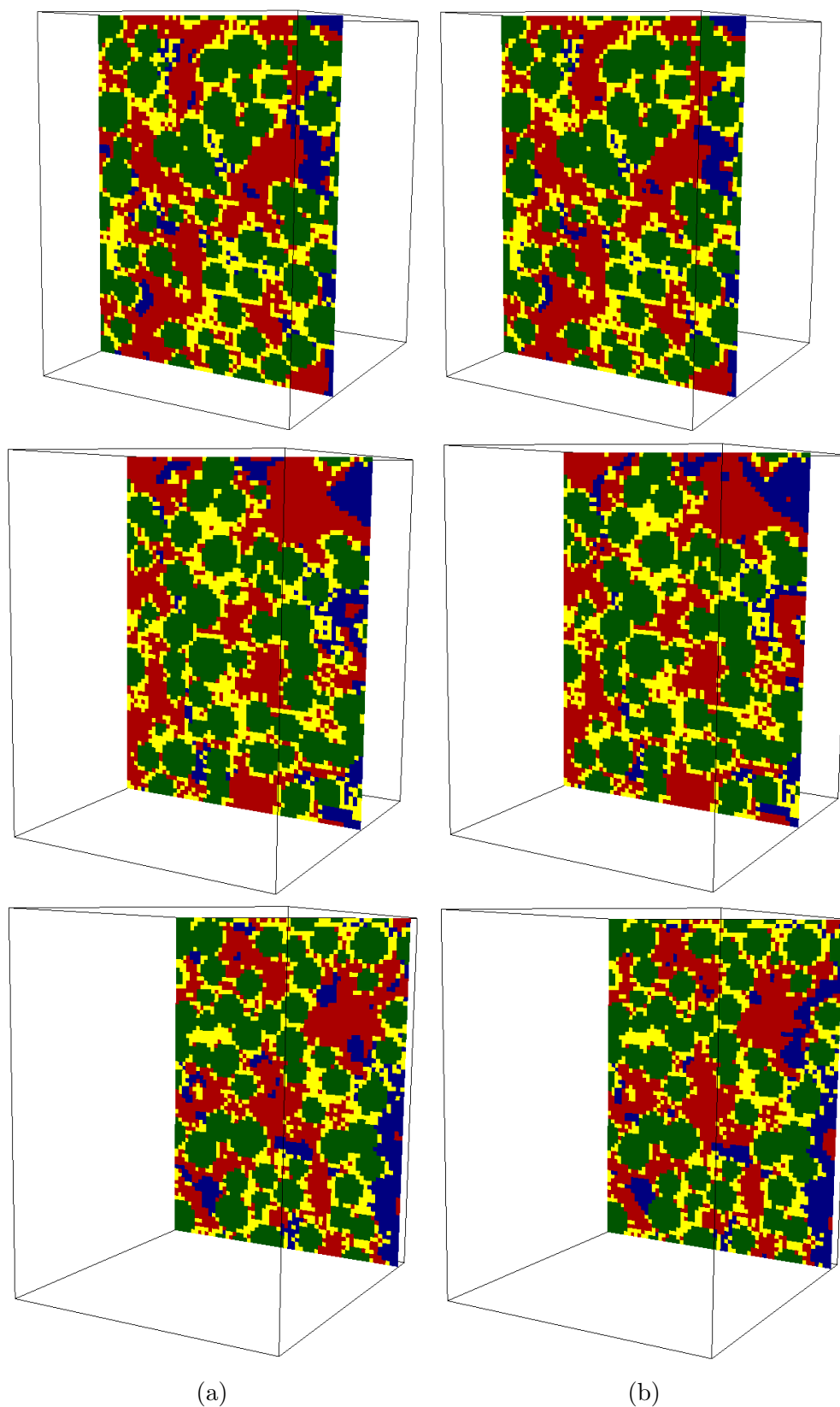


Figure 5.34: Impact of different pressure gradients on water distribution with $S=70$ and hydrophobic ionomer surface shown in three slices through the CL structure: **a)** $\delta p=3.2e-5$ ($=5.4$ KPa) **b)** $\delta p=4.8e-5$ ($=8.1$ KPa). (Green represents carbon, yellow is ionomer, blue is gas filled pores, and red water filled pores)

Chapter 6

Conclusions and Future Work

6.1 Conclusions

In the first part of the thesis, a multiple relaxation time lattice Boltzmann method (MRT-LBM) was used to investigate water transport dynamics in a PEMFC catalyst layer sample that was numerically reconstructed based on a stack of SEM images obtained by sequential slicing of a catalyst sample. The validated MRT-LBM model provides physically representative simulations of high-density-ratio two-phase flows. This accurate model combined with the physically representative structure and morphology of the catalyst layer provided fundamental insight into key dynamic transport processes in PEM fuel-cell electrodes. A parametric study enabled exploration of the effects of hydrophobicity, viscosity ratio, pressure gradient, and surface tension. A less hydrophobic medium was found to give rise to higher water saturation in the domain, with a contact angle between $\theta = 110^\circ$ and $\theta = 115^\circ$ providing optimal wettability of the catalyst layer materials. It has been shown that a higher pressure gradient as well as lower viscosity ratio result in higher water saturation, which is attributed to a lubricating effect. Phase change and the effect of temperature gradients was outside the scope of this work, but the effect of bulk temperature differences was investigated by adjusting surface tension. Lower surface tension results in lower saturation in the stable displacement and transient regimes, but in the capillary fingering regime, it tends to minimize the surface of the fingers without having a significant impact overall on water saturation.

In the second part of the thesis, capillary pressure, which is a dominant force in the nano-structure of catalyst layers, was investigated. A new expression for CL

capillary pressure function was introduced. This new function can provide more accurate prediction of the combined effect of capillarity and reactant transport in fuel cell performance models that rely on a macroscopic representation of the porous electrodes. The effect of different wettabilities of CL materials on capillary pressure was taken into account. It was found that a CL with higher hydrophobicity presents greater resistance to water movement, and therefore greater external forces must be exerted on water to drive it into the CL porous medium.

In the last part of this thesis, the impact of liquid water on effective transport properties and the effect of non-homogeneous wetting properties within the catalyst layer were considered. The simulated results indicate that the parameters most sensitive to the presence of liquid water are effective oxygen and water-vapour diffusivities as well as effective thermal conductivity. Several parametric studies were carried out to determine the effect of different physical parameters on the transport parameters through a stochastically reconstructed CL. The effects of different ionomer contact angles on transport properties was examined for two cases of hydrophobic and hydrophilic ionomer. Effective oxygen and water-vapour diffusivities showed higher values with hydrophilic ionomer and for liquid water saturations less than 50 %. On the other hand, for saturations greater than 50 %, the effective oxygen and water-vapour diffusivities showed higher values for hydrophobic ionomer. The effective thermal conductivity was observed to be higher for the case of hydrophilic ionomer over the entire range of liquid water saturation due to increased number of thermal percolation pathways. The impacts of increasing the pressure gradient from $\delta p=1.6e-5$ (=2.7 KPa) to $\delta p=3.2e-5$ (=5.4 KPa) and also from $\delta p=3.2e-5$ (=5.4 KPa) to $\delta p=4.8e-5$ (=8.1 KPa) were explored separately. The results show that effective oxygen and water-vapour diffusivities decrease with increasing pressure gradient from $\delta p=1.6e-5$ (=2.7 KPa) to $\delta p=3.2e-5$ (=5.4 KPa) over the entire range of liquid water saturation. However, when the pressure gradient is increased from $\delta p=3.2e-5$ (=5.4 KPa) to $\delta p=4.8e-5$ (=8.1 KPa) the diffusivities show higher and lower values for saturations less than and greater than 50 % respectively. For both cases, lower effective thermal conductivity values are obtained by increasing the pressure gradients over the entire range of liquid water saturation.

6.2 Future Work

The proposed work provides new insights as well as macroscopic transport parameters required for integrated fuel cell performance and degradation modeling. The methodology can also be applied to inform improved CL design and investigate strategies for improved water management to avoid flooding. The reconstruction and modeling methodology can be extended to other layers of the electrode and serve as the basis for a systematic investigation of interfacial transport and associated resistances between the various porous components in a fuel cell membrane-electrode assembly (CL, micro-porous layer, gas diffusion layer). Additionally, during fuel cell operation, liquid water that form and transports through the porous electrodes eventually emerges into the flow channel, resulting in a complex dynamic pattern of coalescence and shedding of droplets that affect pressure drop and reactant flow distribution [24]. LBM will be well suited to investigate these issues in future work. Thus extension of the methodology presented in this thesis could address the following questions:

1. How does water behave at the interface of different components, e.g. the CL/MPL and MPL/GDL interfaces?
2. What is the impact of cracks generated due manufacturing in CL and MPL? Can such cracks be engineered to improve water management in these components?
3. How does water move through different components that have different or heterogeneous hydrophobicities?
4. What would be the impact of different PTFE and binder contents in MPL and GDL on water transport?

The simulations performed in this thesis mimic physical imbibition/drainage experiments. Future work should consider coupling of LBM to electrochemical reaction to allow simulation of local water generation at the reaction sites of the CL.

Appendix A

Additional Information

A.1 Impact of Liquid Water on Transport Parameters in hydrophilic Catalyst Layers

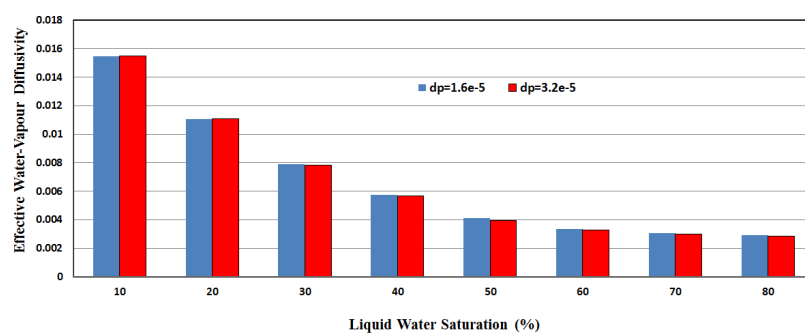


Figure A.1: Impact of different pressure gradients on effective water-vapour diffusivity with hydrophilic ionomer surface.

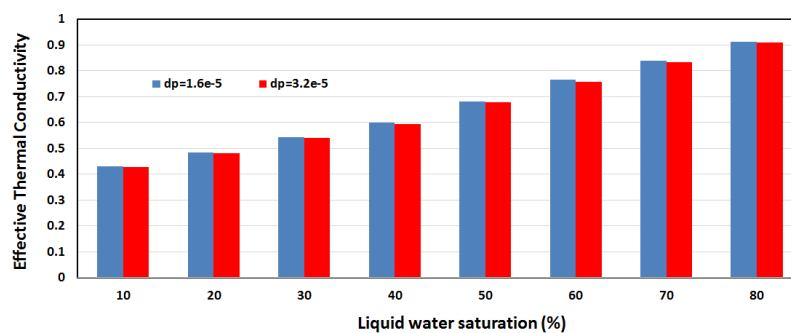


Figure A.2: Impact of different pressure gradients on effective thermal conductivity with hydrophilic ionomer surface.

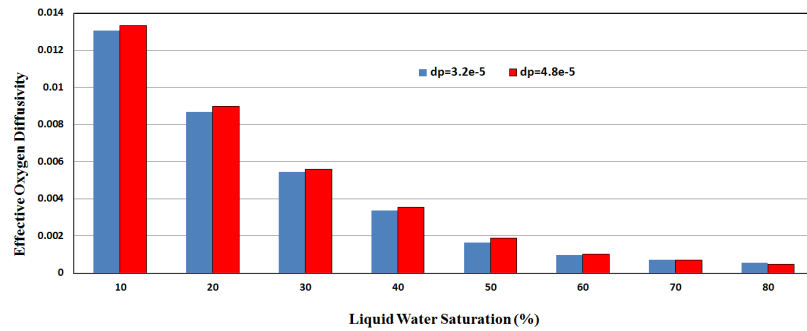


Figure A.3: Impact of different pressure gradients on effective oxygen diffusivity with hydrophilic ionomer surface.

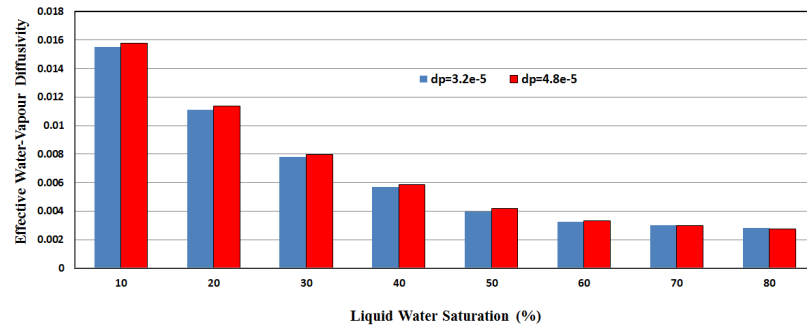


Figure A.4: Impact of different pressure gradients on effective oxygen diffusivity with hydrophilic ionomer surface.

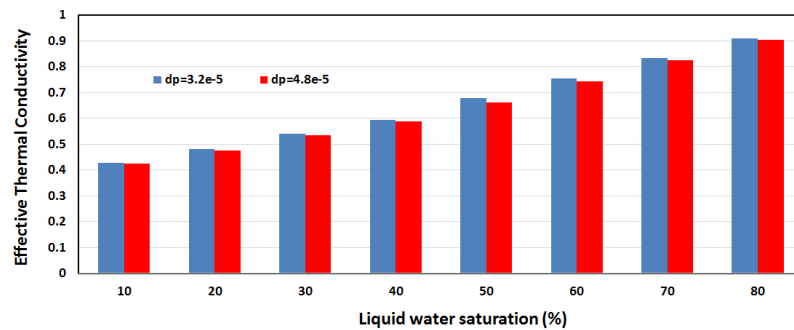


Figure A.5: Impact of different pressure gradients on effective thermal conductivity with hydrophilic ionomer surface.

A.2 Relation Between Units in the Framework of LBM and Physical Units

Length:

$$\frac{L_p}{\Delta x_p} = \frac{L_{LB}}{\delta x_{LB}} \quad (\text{A.1})$$

Or

$$L_p = \Delta x_p \frac{L_{LB}}{\delta x_{LB}} \quad (\text{A.2})$$

where subscripts LB and p represent the parameters in lattice Boltzmann space and physical space.

Pressure:

$$\frac{P_p}{\frac{\sigma_p}{\Delta x_p}} = \frac{P_{LB}}{\frac{\sigma_{LB}}{\delta x_{LB}}} \quad (\text{A.3})$$

Or

$$P_p = \frac{\sigma_p}{\Delta x_p} \frac{P_{LB}}{\frac{\sigma_{LB}}{\delta x_{LB}}} \quad (\text{A.4})$$

Time Steps:

$$\frac{\nu_p}{\frac{\Delta x_p^2}{\Delta t_p}} = \frac{\nu_{LB}}{\frac{\delta x_{LB}^2}{\delta t_{LB}}} \quad (\text{A.5})$$

Or

$$\Delta t_p = \frac{\Delta x_p^2}{\nu_p} \frac{\nu_{LB}}{\frac{\delta x_{LB}^2}{\delta t_{LB}}} \quad (\text{A.6})$$

Bibliography

- [1] N. Djilali. Computational modelling of polymer electrolyte membrane PEM fuel cells: Challenges and opportunities. *Energy*, 32:269–280, 2007.
- [2] R. Borup, J. Meyers, B. Pivovar, Y.S. Kim, R. Mukundan, N. Garland, and D. Myers. Scientific aspects of polymer electrolyte fuel cell durability and degradation. *Chemical Review*, 107:3904–15, 2007.
- [3] M.M. Mench. *Fuel Cell Engines*. John Wiley & Sons, 2008.
- [4] C.Y. Wang, W. Lietsich, and A. Lamm. *Handbook of Fuel Cells: Fundamentals, technology and applications*, volume 3. John Wiley & Sons, 2003.
- [5] A.Z. Weber, R.L. Borup, R.M. Darling, P.K. Das, T.J. Dursch, W. Gu, D. Harvey, A. Kusoglu, S. Litster, M.M. Mench, R. Mukundan, J.P. Owejan, J.G. Pharoah, M. Secanell, and I.V. Zenyuk. A critical review of modeling transport phenomena in polymer-electrolyte fuel cells. *J. Electrochem. Soc.*, 161:F1254–F1299, 2014.
- [6] K. Jiao and X. Li. Water transport in polymer electrolyte membrane fuel cells. *Progress in Energy and Combustion Science*, 37:221–291, 2011.
- [7] M. Ji and Z. Wei. A review of water management in polymer electrolyte membrane fuel cells. *Energies*, 2:1057–1106, 2009.
- [8] H. Schulenburg, B. Schwanitz, N. Linse, G. Scherer, A. Wokaun, J. Krbanjevic, R. Grothausmann, and I. Manke. 3D imaging of catalyst support corrosion in polymer electrolyte fuel cells. *J. Physical Chemistry*, 115:14236–1442, 2011.
- [9] J. Hu, P.C. Sui, S. Kumar, and N. Djilali. Modeling and simulations of carbon corrosion during operation of a polymer electrolyte membrane fuel cell. *Electrochimica Acta*, 54:5583–5592, 2009.

- [10] H. Li, Y. Tang, Z. Wang, Z. Shi, S. Wu, D. Song, J. Zhang, K. Fatih, J. Zhang, H. Wang, Z. Liu, R. Abouatallah, and A. Mazza. A review of water flooding issues in the proton exchange membrane fuel cell. *J. Power Sources*, 178:103–117, 2008.
- [11] K. Tuber, D. Pcza, and C. Hebling. Visualization of water buildup in the cathode of a transparent PEM fuel cell. *J. Power Sources*, 124:403–414, 2003.
- [12] A.P. Young, J. Stumper, S. Knights, and E. Gyenge. Ionomer degradation in polymer electrolyte membrane fuel cells. *J. Electrochemical Society*, 157:B425 – B436, 2010.
- [13] R. Singh, A. R. Akhgar, P. C. Sui, K. J. Lange, and N. Djilali. Dual-beam FIB/SEM characterization, statistical reconstruction, and pore scale modeling of a PEMFC catalyst layer. *J. Electrochemical Society*, 161:F415–F424, 2014.
- [14] K.J. Lange, H. Carlsso, I. Stewart, P.C. S, R. Herring, and N. Djilali. PEM fuel cell CL characterization using a standalone FIB and SEM: experiments and simulation. *Electrochimica Acta*, 85:322–331, 2012.
- [15] G. Wang, P.P. Mukherjee, and C.Y. Wang. Direct numerical simulation (DNS) modeling of PEFC electrodes. *Electrochimica Acta*, 51:3139–3150, 2006a.
- [16] P.P. Mukherjee and C.Y. Wang. Stochastic microstructure reconstruction and direct numerical simulation of the PEFC catalyst layer. *J. Electrochemical Society*, 153:A840, 2006.
- [17] S.H. Kim and H. Pitsch. Reconstruction and effective transport properties of the catalyst layer in PEM fuel cells. *J. Electrochemical Society*, 156:B673, 2009.
- [18] N.A. Siddique and F. Liu. Process based reconstruction and simulation of a three-dimensional fuel cell catalyst layer. *Electrochimica Acta*, 55:5357–5366, 2010.
- [19] D. Gerteisen, T. Heilmann, and C. Ziegler. Modeling the phenomena of dehydration and flooding of a polymer electrolyte membrane fuel cell. *J. Power Sources*, 187:165, 2009.
- [20] U. Pasaogullari and C. Y. Wang. Two-phase modeling and flooding prediction of polymer electrolyte fuel cells. *J. Electrochemical Society*, 152:A380, 2005.

- [21] D. Natarajan and T. V. Nguyen. Three-dimensional effects of liquid water flooding in the cathode of a PEM fuel cell. *J. Power Sources*, 115:66, 2003.
- [22] J. J. Baschuk and X. Li. Modelling of polymer electrolyte membrane fuel cells with variable degrees of water flooding. *J. Power Sources*, 86:181, 2000.
- [23] A. Bazylak. Liquid water visualization in PEM fuel cell: A review. *Int. J. Hydrogen Energy*, 34:3845–3857, 2009.
- [24] T.C. Wu and N. Djilali. Experimental investigation of water droplet emergence in a model polymer electrolyte membrane fuel cell microchannel. *J. Power Sources*, 208:248–256, 2012.
- [25] A. Bazylak, D. Sinton, and N. Djilali. Dynamic water transport and droplet emergence in PEMFC gas diffusion layers. *J. Power Sources*, 176:240–246, 2008.
- [26] S Lister, D. Sinton, and N. Djilali. Ex situ visualization of liquid water transport in PEM fuel cell gas diffusion layers. *J. Power Sources*, 154:95–105, 2006.
- [27] A Bazylak, D. Sinton, Z.S. Liu, and N. Djilali. Effect of compression on liquid water transport and microstructure of PEMFC gas diffusion layers. *J. Power Sources*, 163:784–792, 2007.
- [28] R. Mukundan and R.L. Borup. Visualizing liquid water in PEM fuel cells using neutron imaging. *Fuel Cells*, 5:499–505, 2009.
- [29] P. Deevanhxay, T. Sasabe, S. Tsushima, and S. Hirai. Investigation of water accumulation and discharge behaviors with variation of current density in PEMFC by high-resolution soft X-ray radiography. *Int. J. Hydrogen Energy*, 36:10901–10907, 2011.
- [30] P. Deevanhxay, T. Sasaabe, S. Tsushima, and S. Hirai. Observation of dynamic liquid water transport in the microporous layer and gas diffusion layer of an operating PEM fuel cell by high resolution soft X-ray radiography. *J. Power Sources*, 230(38-43), 2013.
- [31] P. Deevanhxay, T. Sasabe, S. Tsushima, and S. Hirai. Effect of liquid water distribution in gas diffusion media with and without microporous layer on PEM fuel cell performance. *Electrochemistry Communications*, 34:239–241, 2013.

- [32] P. Deevanhxay, T. Sasabe, S. Tsushima, and S. Hirai. In situ diagnostic of liquid water distribution in cathode catalyst layer in an operating PEMFC by high resolution soft X-ray radiography. *Electrochemistry Communications*, 22:33–36, 2012.
- [33] T. Sasaabe, P. Deevanhxay, S. Tsushima, and S. Hirai. Soft X-ray visualization of the liquid water transport within the cracks of micro porous layer in PEMFC. *Electrochemistry Communications*, 13:638–641, 2011.
- [34] T. Sasaabe, P. Deevanhxay, S. Tsushima, and S. Hirai. Investigation on the effect of microstructure of proton exchange membrane fuel cell porous layers on liquid water behaviour by soft X-ray radiography. *J. Power Sources*, 196:8197–8206, 2011.
- [35] P. Antonacci, S. Chevalier, J. Lee, R. Yip, N. Ge, and A. Bazylak. Feasibility of combining electrochemical impedance spectroscopy and synchrotron X-ray radiography for determining the influence of liquid water on polymer electrolyte membrane fuel cell performance. *Int. J. Hydrogen Energy*, 40:16494–16502, 2015.
- [36] J. Lee, R. Yip, R. Antonacci, N. Ge, T. Kotaka, Y. Tabuchi, and A. Bazylak. Synchrotron investigation of microporous layer thickness on liquid water distribution in a PEM fuel cell. *J. Electrochemical Society*, 162:F669–F676, 2015.
- [37] J. Hinebaugh, J. Lee, C. Mascarenhas, and A. Bazylak. Quantifying percolation events in PEM fuel cell using synchrotron radiography. *Electrochimica Acta*, 184:417–426, 2015.
- [38] U. Pasaogullari and C.Y. Wang. Two phase transport and role of micro-porous layer in polymer electrolyte fuel cells. *Electrochimica Acta*, 49:4359–4369, 2004.
- [39] C.Y. Wang. Fundamental models for fuel cell engineering. *Chemical Reviews*, 104:4727–4766, 2004.
- [40] S. Lister and N. Djilali. Two Phase Transport in Porous Gas Diffusion Electrodes. *Transport Phenomena in Fuel Cells*. WIT Press, 2005.

- [41] T. Berning and N. Djilali. A three-dimensional, multi-phase, multicomponent model of the cathode and anode of a PEM fuel cell. *J. Electrochemical Society*, 150:A1598–A1607, 2003.
- [42] E. Thompson. Pore scale modeling of fluid transport in disordered fibers materials. *J. American Institute of Chemical Engineers*, 48:1369–1389, 2002.
- [43] P.K. Sinha, P.P. Mukherjee, and C.Y. Wang. Impact of GDL structure and wettability on water management in polymer electrolyte fuel cells. *J. Material Chemistry*, 17:3089–103, 2007.
- [44] P.K. Sinha and C.Y. Wang. Pore-network modeling of liquid water transport in gas diffusion layer of a polymer electrolyte fuel cell. *Electrochimica Acta*, 52:7936–45, 2007.
- [45] A. Bazylak, V. Berejnov, B. Markicevic, D. Sinton, and N. Djilali. Numerical and microfluidic pore networks: Towards designs for directed water transport in GDLs. *Electrochimica Acta*, 53:7630–7637, 2008.
- [46] B. Markicevic and N. Djilali. Analysis of liquid water transport in fuel cell gas diffusion media using two-mobile phase pore network simulations. *J. Power Sources*, 196:2725–2734, 2011.
- [47] X. Zhu, P.C. Sui, and N. Djilali. Numerical simulation of emergence of a water droplet from a pore into a microchannel gas stream. *Microfluidics and Nanofluidics*, 6:543–555, 2008.
- [48] X. Zhu, P.C. Sui, and N. Djilali. Three-dimensional numerical simulations of water droplet dynamics in a PEMFC gas channel. *J. Power Sources*, 181:101–115, 2008.
- [49] S. Ryu and S. Ko. A comparative study of lattice Boltzmann and volume of fluid method for two-dimensional multiphase flows. *J. Nuclear Engineering and Technology*, 44(6):623–638, 2012.
- [50] S. Annaland, W. Dijkhuizen, N.G. Deen, and J.A.M. Kuipers. Numerical simulation of behaviour of gas bubbles using a 3-D front tracking method. *J. AIChE*, 52:99–110, 2006.

- [51] H. Huang, H. Zheng, X.Y. Lu, and C. Shu. An evaluation of a 3D free-energy based lattice Boltzmann model for multiphase flows with large density ratio. *Int. J. Numerical Methods in Fluids*, 63:11931207, 2009.
- [52] U. Frisch, B. Hasslacher, and Y.Pomeau. Lattice-gas automata for the Navier-Stokes equation. *Physical Review Letters*, 56:15051508, 1986.
- [53] A.G. Yiotis, J. Psihogios, M.E. Kainourgiakis, A. Paspaioannou, and A.K. Stubbos. A lattice Boltzmann study of viscous coupling effect in immiscible two-phase flow in porous media. *J. Coll Surf*, 300:35–49, 2007.
- [54] T. Koido, T. Furusawa, and K. Moriyama. An approach to modeling two-phase transport in the gas diffusion layer of a proton exchange membrane fuel cell. *J. Power Sources*, 175:127–136, 2008.
- [55] A.K. Gunstensen, D.H. Rothman, S. Zaleski, and G. Zanetti. Lattice Boltzmann model of immiscible fluids. *Phys. Rev. A*, 43:4320–4327, 1991.
- [56] X. Shan and H. Chen. Lattice Boltzmann model for simulating flows with multiple phases and components. *Phys. Rev. A*, 47:181519, 1993.
- [57] M.R. Swift, S.E. Orlandini, W.R. Osborn, and J.M. Yeomans. Lattice Boltzmann simulations of liquid-gas and binary fluid systems. *Phys. Rev. E*, 54:5041–52, 1996.
- [58] X. He, S. Chen, and R. Zhang. A lattice Boltzmann scheme for incompressible multiphase flow and its application in simulation of Rayleigh-Taylor instability. *J. Comput. Phys*, 152:642–663, 1999.
- [59] D.H. Rothman and J.M. Keller. Immiscible cellular-automaton fluids. *J. Statistical Physics*, 52:1119–1127, 1988.
- [60] D.W. Grunau, S. Chen, and K. Eggert. A lattice Boltzmann model for multiphase fluid flows. *Phys. Fluids A*, 5:2557–2562, 1993.
- [61] T. Reis and T.N. Phillips. Lattice Boltzmann model for simulating immiscible two-phase flows. *J. Physics A*, 40:4033–4053, 2007.
- [62] S.V. Lishchuk, C.M. Care, and I. Halliday. Lattice Boltzmann algorithm for surface tension with greatly reduced microcurrents. *Phys. Rev. E*, 67:036701, 2003.

- [63] M. Latva-Kokko and D.H. Rothman. Diffusion properties of gradient-based lattice Boltzmann models of immiscible fluids. *Phys. Rev. A*, 71:056702, 2005.
- [64] C.K. Aidun and J.R. Clausen. Lattice Boltzmann method for complex flows. *Annual Review. Fluid Mechanics*, 42:439–472, 2010.
- [65] C. Pan, M. Hilpert, and C.T. Miller. Lattice Boltzmann simulation of two-phase flow in porous media. *J. Water Resources Research*, 40:01501, 2004.
- [66] X.D. Niu, T. Munekata, S.A. Hyodo, and K. Suga. An investigation of water-gas transport processes in the gas-diffusion-layer of a PEM fuel cell by a multiphase multi-relaxation-time lattice Boltzmann model. *J. Power Sources*, 172:542–552, 2007.
- [67] T. Inamuro, T. Ogata, S. Tajima, and N. Konishi. A lattice Boltzmann method for incompressible two-phase flows with large density differences. *J. Computational Physics*, 198:628–44, 2004.
- [68] B.T. Nadiga and S. Zaleski. Investigations of a two-phase fluid model. *Eur. J. Mech. B/Fluids*, 15:88596, 1996.
- [69] H.W. Zheng, C. Shu, and Y.T. Chew. A lattice Boltzmann model for multiphase flows with large density ratio. *J. Computational Physics*, 218:353–71, 2006.
- [70] L. Hao and P. Cheng. Lattice Boltzmann simulation of anisotropic permeabilities in carbon paper gas diffusion layers. *J. Power Sources*, 186:104–114, 2009.
- [71] L. Hao and P. Cheng. Lattice Boltzmann simulations of water transport in gas diffusion layer of a polymer electrolyte membrane fuel cell. *J. Power Sources*, 195:3870–3881, 2010.
- [72] L. Hao and P. Cheng. Capillary pressure in carbon paper gas diffusion layers having hydrophilic and hydrophobic pores. *J. Heat and Mass Transfer*, 55:133–139, 2012.
- [73] Y. Gao, X. Zhang, P. Rama, R. Chen, H. Ostadi, and K. Jiang. Lattice Boltzmann simulation of water and gas flow in porous gas diffusion layers in fuel cells reconstructed from Micro-Tomography. *J. Computer and Mathematics with Applications*, 65:891–900, 2013.

- [74] K. Moriyama and T. Inamuro. Lattice Boltzmann simulations of water transport from the gas diffusion layer to the gas channel in PEMFC. *Communications in Computational Physics*, 9:1206–1218, 2011.
- [75] J.H. Nam and M. Kaviany. Effective diffusivity and water-saturation distribution in single and two-layer PEMFC diffusion medium. *J. Heat and Mass Transfer*, 46:4595 – 4611, 2003.
- [76] P. Mukherjee, C.Y Wang, and Q. Kang. Mesoscopic modeling of two-phase behavior and flooding phenomena in polymer electrolyte fuel cells. *Electrochimica Acta*, 54:6861–6875, 2009.
- [77] D. Jacqmin. Calculation of two-phase Navier Stokes flows using phase-field modeling. *J. Computational Physics*, 155:96–127, 1999.
- [78] M.E. McCracken and J. Abraham. Multiple-relaxation-time lattice Boltzmann model for multiphase flow. *Phys. Rev. E*, 71:036701–036709, 2005.
- [79] D. Harvey, J. G. Pharoah, and K. Karan. A comparison of different approaches to modelling the PEMFC catalyst layer. *J. Power Sources*, 179:209, 2008.
- [80] P. K. Das, X. Li, and Z.-S. Liu. Effective transport coefficients in PEM fuel cell catalyst and gas diffusion layers: Beyond Bruggeman approximation. *Appl. Energy*, 87:2785, 2010.
- [81] K.J. Lange, P.C. Sui, and N. Djilali. Pore scale simulation of transport and electrochemical reactions in reconstructed PEMFC catalyst layers. *J. Electrochemical Society*, 157:B1434 – B1442, 2010.
- [82] K.J. Lange, P.C. Sui, and N. Djilali. Determination of effective transport properties in a PEMFC catalyst layer using different reconstruction algorithms. *J. Power Sources*, 208:354–365, 2012.
- [83] L. Hao and P. Cheng. Pore scale simulations on relative permeabilities of porous media by lattice Boltzmann method. *J. Heat Mass Transfer*, 53:1908–1913, 2010.
- [84] H.W. Zheng, C. Shu, and Y.T. Chew. Lattice Boltzmann interface capturing method for incompressible flows. *Phys. Rev. E*, 72:056705–056710, 2005.

- [85] V.M. Kendon, M.E. Cates, I. Pagonabarraga, C. Desplat, and P. Bladon. Inertial effects in three-dimensional spinodal decomposition of a symmetric binary fluid mixture: A lattice Boltzmann study. *J. Fluid Mech*, 440:147–203, 2001.
- [86] T. Hutzenlaub, J. Becker, R. Zengerle, and S. Thiele. Modelling the water distribution within a hydrophilic and hydrophobic 3D reconstructed cathode catalyst layer of a proton exchange membrane fuel cell. *J. Power Sources*, 227:260, 2013.
- [87] S. Thiele, R. Zengerle, and C. Ziegler. Nano-morphology of a polymer electrolyte fuel cell catalyst layer-imaging, reconstruction and analysis. *J. Nano Research*, 4:849–860, 2011.
- [88] A.W. Gladrow. *Lattice-gas cellular automata and lattice Boltzmann models-An Introduction*. Springer, 2005.
- [89] A. A. Mohamad. *Lattice Boltzmann Method: Fundamentals and Engineering Applications with Computer Codes*. Springer, 2011.
- [90] Sauro Succi. *The lattice Boltzmann equation for fluid dynamics and beyond*. Oxford Press, 2001.
- [91] Michael C. Sukop and Daniel T. Thorne. *Lattice Boltzmann Modeling; an Introduction for Geoscientists and Engineers*. Springer, 2006.
- [92] A.J. Briant, P.Papatzacos, and M. Yeomans. Lattice Boltzmann simulations of contact line motion in a liquid-gas system. *Philos. Trans. R. Soc. London, Ser. A*, 360:485, 2002.
- [93] J.J. Huang, C.Shu, and Y.T.Chew. Lattice Boltzmann study of droplet motion inside a grooved channel. *Phys. Fluids*, 21:022103–022111, 2009.
- [94] K.J. Lange, C. Misra, P.C. Sui, and N. Djilali. A numerical study on preconditioning and partitioning schemes for reactive transport in a PEMFC catalyst layer. *Computer Methods in Applied Mechanics and Engineering*, 200(9-12):905–916, 2011.
- [95] K.J. Lange, P.C. Sui, and N. Djilali. Using an ILU/deflation preconditioner for simulation of a PEM fuel cell cathode catalyst layer. *Communications in Computational Physics*, 14(3):537–573, 2013.

- [96] A.A. Zick and G.M. Homsy. Stokes flow through periodic arrays of spheres. *J. Fluid Mechanics*, 115:13–26, 1982.
- [97] D.F. Young, B.R. Munson, and T.H. Okiishi. *A Brief Introduction to Fluid Mechanics*. John Wiley & Sons Inc, 2001.
- [98] J.M. LaManna, J.V. Bothe, F.Y. Zhang, and M.M. Mench. Measurement of capillary pressure in fuel cell diffusion media, micro-porous layers, catalyst layers, and interfaces. *J. Power Sources*, 271:180–186, 2014.
- [99] V.P. Schulz, J. Becker, A. Wiegmann, P.P. Mukherjee, and C.Y Wang. Modeling of two-phase behavior in the gas diffusion medium of PEFCs via full morphology approach. *J. Electrochemical Society*, 154:B419–B426, 2007.
- [100] W.H.J. Hogarth and J.B. Benziger. Operation of polymer electrolyte membrane fuel cells with dry feeds: Design and operating strategies. *J. Power Sources*, 159:968–978, 2006.
- [101] D. Chen and H. Peng. A thermodynamic model of membrane humidifiers for PEM fuel cell humidification control. *J. Dynamic Systems, Measurement, and Control*, 127:424–432, 2005.
- [102] A Li, M. Han, S.H. Chan, and N.T. Nguyen. Effect of hydrophobicity of the cathode catalyst layer on the performance of a PEM fuel cell. *Electrochimica Acta*, 55:27062711, 2010.
- [103] H.M. Yu, C. Ziegler, M. Oszcipok, M. Zobel, and C. Hebling. Hydrophilicity and hydrophobicity study of catalyst layers in proton exchange membrane fuel cells. *Electrochimica Acta*, 51:11991207, 2006.
- [104] D.K. Paul and K. Karan. Conductivity and wettability changes of ultrathin nafion films subjected to thermal annealing and liquid water exposure. *J. Physical Chemistry*, 118:18281835, 2014.